LA-9333-T
Thesis

UC-20f
Issued: May 1982

LA--9333-T

DE82 0173[illegible]

The Behavior of a Plasma in a High-Density Gas-Embedded Z-Pinch Configuration

Jack Sherman Shlachter

Los Alamos Los Alamos National Laboratory
Los Alamos, New Mexico 87545

[illegible]

CONTENTS

List of Figures

THE BEHAVIOR OF A PLASMA IN A HIGH DENSITY GAS EMBEDDED Z-PINCH CONFIGURATION

by

Jack Sherman Shlachter

ABSTRACT

Vigorous research in plasma physics during the past thirty years has been motivated, in part, by the desire for a controlled fusion energy source. In the linear Z-pinch, one of the earliest configurations examined as the basis for a magnetic confinement fusion device, the plasma conducts an axial current between two electrodes. Ideally, the plasma is resistively heated to ignition temperature while the current simultaneously generates an azimuthal magnetic field which confines the hot material and prevents contact with the cold chamber walls. The observation and appreciation of magnetohydrodynamic instabilities, however, led to disillusionment with the linear Z-pinch approach. An evaluation of a related concept based on a gas embedded current-carrying plasma channel suggests advantages of operation in the high density regime, with filling pressures of approximately one atmosphere. Simple scaling arguments indicate that the channel radii compatible with this pressure are in the range of 50-200 μ, and the corresponding confinement time scale is about one microsecond. This novel area of plasma physics is explored in an ongoing research program at Los Alamos National Laboratory.

In this paper, the theoretical analysis of a high density Z-pinch (HDZP) begins with an examination of the steady state energy balance between ohmic heating and bremsstrahlung radiation losses for a plasma column in pressure equilibrium. The model is then expanded to include the time-varying internal energy and results in a quasi-equilibrium prescription for the load current through a constant radius plasma channel. This set of current waveforms is useful in the design of experimental systems. The behavior of a plasma for

physically realizable conditions is first examined by allowing adiabatic changes in the column radius. A more complete model is then developed by incorporating inertial effects into the momentum equation, and the resultant global MHD computational model is compared with more sophisticated, and costly, one- and two-dimensional computer simulations. These comparisons demonstrate the advantages of the global MHD description over previously developed zero-dimensional models.

A 6 kJ experiment capable of generating 100 kA load currents through a 5 cm long plasma channel has been in operation since 1978. This machine consists of a 600 kV Marx bank generator coupled to the plasma through an intermediate, water dielectric, coaxial transmission line. The system can be operated in two distinct modes, producing current rise rates of 8×10^{11} As^{-1} or 5×10^{12} As^{-1}. Initiation of the discharge path is provided by a pulsed ruby laser focused inside the load chamber and fired 100 ns before application of the Marx-generated voltage. Optical diagnostics employing a pulsed N_2 laser have been used to obtain electron density information. An original technique which has been successfully implemented is a quantitative Schlieren method using the Moiré pattern created by two coarse gratings. The Moiré-Schlieren results are in good agreement with interferometric data produced in a conventional Mach-Zehnder configuration. An x-ray detector consisting of a metallic foil, a plastic scintillator, and a fast photomultiplier tube has allowed investigation of the bremsstrahlung emission from the plasma. Additional data have been acquired from current and voltage probes in the transmission line and load chamber.

Observations of the plasma dynamics indicate a monotonic expansion of the channel, in conflict with the predictions of the global MHD model. Moiré-Schlieren and interferometric data provide evidence for an accompanying increase in plasma line density. This is an effect which is not included in the simple computer model, and accretion is thus recognized as an important process in HDZP plasmas. A more significant discrepancy has been observed between the x-ray detector signals and the temperatures estimated from the measurements of plasma density and total current. A plausible hypothesis to explain this inconsistency requires the bulk of the load current to flow outside the laser-initiated channel, undetected by the optical diagnostics. Support for this hypothesis comes from additional experimental results, simple calculations, and the self-consistent solution provided by a two-dimensional MHD computer code.

THE BEHAVIOR OF A PLASMA IN A HIGH DENSIT GAS EMBEDDED Z-PINCH CONFIGURATION

by

Jack Sherman Shlachter

Chapter 1. Introduction

1.1 Historical Overview and Motivation for High Density Z-Pinches

Magnetic confinement fusion schemes attempt to achieve high temperatures, greater than 10 keV, while simultaneously satisfying a constraint on the ion density, n, and confinement time, τ. The linear Z-pinch[1] is a device which in its simplest form requires no auxiliary magnetic field; an axial current carried by the plasma produces an azimuthal confining field and provides ohmic or resistive heating. The Lawson criterion[2] for deuterium-tritium plasmas,

$$n\tau \geq 10^{20}\ \mathrm{m}^{-3}\mathrm{s}\ , \qquad (1.1)$$

expresses a breakeven condition balancing the fusion reaction output power with the losses resulting from particle heating and bremsstrahlung radiation. Early Z-pinch experiments typically investigated the regime $n \sim 10^{19}$-$10^{24}\ \mathrm{m}^{-3}$ seeking 10^{-4}-10 s confinement times. The plasma formed at the surface of an insulating wall and was compressed or "pinched" radially inward by the magnetic pressure of the self-generated B_θ. Violent and disruptive motion of the column was often observed during the plasma lifetime both visually and in the voltage and current signals, and this behavior was attributed to magnetohydrodynamic (MHD) instabilities caused by "bad field curvature." In simple terms, the plasma was driven toward a lower energy configuration by the magnetic field. Representative of these MHD instabilities are the sausage and kink modes (Fig. 1.1), which were sufficiently disruptive to the plasma in early experiments to establish upper limits on the confinement time, well below that required by the Lawson criterion. In addition, desorption of high Z impurities off the insulating chamber walls often resulted in excessive line and continuum radiation losses, and plasma temperatures remained well below ignition. Subsequent efforts involved the application of a stabilizing axial magnetic field, but additional instabilities were detected, and simple linear Z-pinches

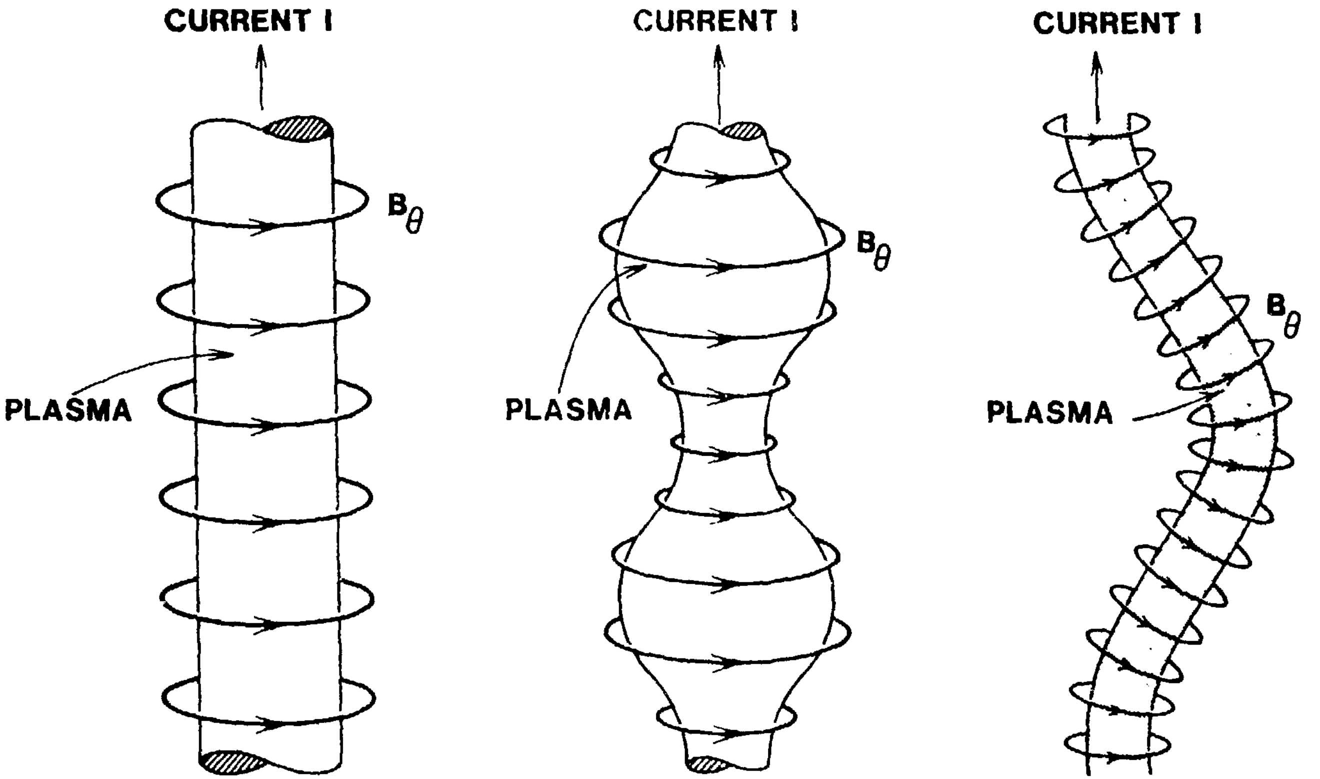

(A) BEFORE INSTABILITY **(B) SAUSAGE INSTABILITY** **(C) KINK INSTABILITY**

Fig. 1.1 Sausage and kink instabilities in a Z-pinch [Reproduced from D. J. Rose and M. Clark, <u>Plasmas and Controlled Fusion</u> (M.I.T. Press, Cambridge, Massachusetts, 1961)] created at the chamber walls have been essentially abandoned for the past several years.

In 1960, Alfvén[3] recognized that a small plasma column initiated inside a larger volume of surrounding neutral gas would not suffer an impurity problem caused by desorption of wall material and would only contact high Z material at the electrodes. In the high temperature, high density regime, radial thermal conductivity might be minimal.[4] Furthermore, the creation of an ionized coronal region surrounding the current-carrying hot channel might add sufficient inertial drag to stabilize the plasma against MHD kink instabilities. Recent analytical calculations by Manheimer et al.,[5] have shown that a coronal region might reduce growth rates for kink modes by two orders of magnitude. Early experimental work on gas embedded Z-pinches using a plasma preionized by a dc arc was conducted by Smars.[6] The H_2 discharge between two plane electrodes at atmospheric pressure was supplied by a generator producing a current rise rate

$$\dot{I} = 10^{11}\ \mathrm{As}^{-1} \tag{1.2}$$

with a peak current of 10^5 A. A helical instability was investigated and spectroscopic diagnostics indicated peak temperatures of 14 eV. The channel also displayed a monotonic expansion. Research on laser-induced breakdown phenomena[7,8] and light-gas interactions below the threshold for optical breakdown suggested the use of an intense optical source for plasma channel initiation. Pechacek et al.,[9-12] have subsequently pursued studies of laser guided discharges using a 70 joule Nd source, while recent work at Sandia National Laboratory[13] has examined the formation of a channel by tuned CO_2 irradiation for ion beam propagation experiments. An alternate initiation scheme employing a collimated electron beam has been investigated by Hartman et al.[14] All of these experiments on gas embedded channels to date have operated in the regime of relatively slow current rise, with $\dot{I} < 10^{12}$ As^{-1}, and have observed electron temperatures less than 100 eV and expanding columns.

A re-examination and elaboration of Pease's early energy balance arguments for a Z-pinch[15] has suggested[29,32] that achievement of high temperatures and nonexpanding channels using ohmic heating is contingent upon driving current rise rates of $\sim 5\times10^{12}$ As^{-1}. Generators capable of supplying these fast rising currents with peak currents of approximately 10^6 amperes are a relatively recent technological advance motivated by intense electron and ion beam source development. These devices can generate multimegavolts using Marx banks (capacitors charged in parallel and discharged through fast switches in series) and often require low impedance, high field strength transmission lines to efficiently transfer energy to a load. A fusion reactor based on a narrow (100 μ), high density (10^{27} m^{-3}) gas embedded channel with an e-beam type generator might achieve energy breakeven and ignition temperatures using only ohmic heating with a relatively modest input energy (~ 100 k joule), cost, and size, assuming the plasma remained stable and exhibited classical thermal conduction losses.[16] The high density Z-pinch (HDZP) reactor concept, inherently pulsed with microsecond burn times, represents a large departure from steady state or nearly steady state approaches such as the tokamak, EBT, RFP, and magnetic mirror. Evaluation of the HDZP concept has motivated the construction of a laser-initiated plasma experiment at Los Alamos National Laboratory called the prototype high density Z-pinch or prototype HDZP. This thesis presents a study of the plasma behavior in this device and compares the observations with the predictions of a recently developed global MHD model of the column.

1.2 HDZP Parameter Regime and Scaling

In this section, scaling arguments and simple calculations help analyze various parameters of an HDZP plasma, while details of the model used here are presented in a later chapter. We consider a fully ionized and hydrogenic column of uniform temperature with a spatially uniform current profile and examine possible operating regimes. MKS units are used, but we express temperatures in eV. The breakeven time from the Lawson criterion, Eq. (1.1), is

$$\tau_b \simeq \frac{10^{20}}{n} \quad . \tag{1.3}$$

Instabilities are expected to have a characteristic growth time equal to the ion thermal transit time across the column radius, r;

$$\tau_{IN} \simeq \frac{10^{-4} r}{(T_{ion})^{1/2}} \quad . \tag{1.4}$$

For the simple plasma model used in this analysis, the number of ions or electrons per unit length, often called the line density, N, is given by

$$N = \pi r^2 n \qquad (1.5)$$

and we can rewrite Eq. (1.4) as

$$\tau_{IN} \simeq \frac{10^{-4} \quad N^{1/2}}{\pi^{1/2} n^{1/2} T_{ion}^{\;\;1/2}} \quad . \qquad (1.6)$$

We may choose the useful ion temperature to be 10 keV, set by D-T fusion considerations, and find a constraint on the line density from the Bennett relation.[17] This equation balances magnetic field pressure with plasma internal pressure, and for our model is

$$16\pi N k T_p = \mu_o I^2 \qquad (1.7)$$

where k is the Boltzmann constant, $\mu_o = 4\pi \times 10^{-7}$, and we have assumed $T_p = T_{i} = T_{electron}$. Pease[15] recognized that a steady state value for the current in a linear Z-pinch is found by equating ohmic heating input with bremsstrahlung loss using the Bennett relation, and we write

$$I_{Pease} \simeq 1.3\times10^{6} \text{ A} \quad . \qquad (1.8)$$

Solving Eq. (1.7) for the line density, with the values of I and T_{ion} above,

$$N = \frac{10^{-7}}{4}\,\frac{I^2}{kT_p} = \frac{10^{-7}}{4}\,\frac{(1.3\times10^{6})^2}{1.6\times10^{-19}10^{4}} \simeq 2.6\times10^{19} \text{ m}^{-1} \quad . \qquad (1.9)$$

Equation (1.6) for the instability growth time thus becomes

$$\tau_{IN} \simeq 2.9\times10^3 \frac{1}{n^{1/2}} \quad . \tag{1.10}$$

Results of a simple analysis for the time dependent temperature of a constant radius, constant line density plasma[29,32] indicate a characteristic rise time to the Pease current of

$$\tau_{OH} \simeq 1.6\times10^{31} \frac{r^2}{N^{3/2}} \tag{1.11}$$

which we can re-express using (1.9) and (1.5) as

$$\tau_{OH} \simeq \frac{10^{21}}{n} \quad . \tag{1.12}$$

The basis for a useful fusion operating regime at the Pease current is established by the inequalities

$$\begin{aligned} &\tau_{OH} < \tau_{IN} \\ &\text{and} \\ &\tau_b < \tau_{IN} \quad , \end{aligned} \tag{1.13}$$

and expressions (1.3), (1.10), and (1.12) suggest operation with as high a plasma density as possible. Operation at high temperatures for a constant line density model therefore implies a simultaneous requirement of small column radius using the Bennett relation. Laser-initiation experiments indicate a lower bound of approximately 100 μ for channel radii,[18] and chamber fill pressures of as high as 10 atmospheres (5×10^{26} ions/m^3) are easily manageable; these conditions result in

$$\tau_{IN} \sim 10^{-10} \text{ s} \quad ,$$

$$\tau_{OH} \sim 2\times10^{-6} \text{ s} \quad , \tag{1.14}$$

and

$$\tau_b \sim 2\times10^{-7} \text{ s} \ .$$

An increase in τ_{IN} is obviously still needed, as both the heating and burn times exceed the instability growth time by several orders of magnitude.

A simple analytical stability criterion for the most catastrophic MHD mode (m = 0 sausage) is determined from an energy principle to be[19]

$$\frac{-d \; \ell np}{d \; \ell nr} < \frac{4\gamma}{2 + \gamma\beta} \quad \text{for stability} \tag{1.15}$$

where β is the ratio of plasma pressure to magnetic pressure,

$$\beta = \frac{p}{B^2/2\mu_o} \quad , \tag{1.16}$$

and γ is the adiabaticity index which we set equal to 5/3. The sausage mode constricts the plasma channel at one or more nodes and can seriously impede the current flow. For low β, Eq. (1.15) requires

$$p \sim p_o\left(\frac{r}{r_o}\right)^{-n} \tag{1.17}$$

with

$$n < 10/3 \quad , \tag{1.18}$$

and our model therefore assumes a plasma pressure profile which peaks on axis and falls off with a shallow enough gradient to satisfy stability. Profile considerations have been one motivation for the continuation of laser-initiation studies over the annular plasma schemes involving puffed gas cylinders,[20] cylindrical foils,[21] and wire arrays.[22] In each of these alternate plasma formation mechanisms, the plasma pressure is initially zero on axis, and violation of equation (1.15) is quite possibly the explanation for observed disruptions.

Stability against higher m-modes where the displacement takes the form $\zeta(r,\theta,z) = \zeta(r,z)e^{im\theta}$ is governed by[19]

$$\frac{-d\ \ell n p}{d\ \ell n r} < \frac{m^2}{\beta} \quad , \tag{1.19}$$

and all modes with $m > 2$ will be stable <u>if</u> $m = 0$ is stable. The kink mode ($m = 1$) can still be unstable for $\beta > 2/(3\gamma)$ even if all other m-modes are stable. This configuration is not necessarily an obstacle to normal current flow through the channel, and it is unlikely that a kink excursion would be sufficiently large to cause contact with the chamber walls during the plasma heating time, τ_{OH}, for the example in Eq. (1.14). A kink may increase the plasma line density, however, by accreting cold coronal gas through enhanced thermal conduction and/or convection, and the resultant increase in particle number would effectively decrease the plasma temperature for a constant plasma pressure.

One possible regime where MHD modes may be stable occurs when the ion Larmor radius is comparable to or larger than the column dimensions (FLR stabilization). In this limit, conventional fluid equations are no longer applicable and more complete theoretical treatments as well as experiments have suggested improved stability. We can express the stability factor S as

$$S = \frac{\langle r_{ion} \rangle}{r_p} \quad . \tag{1.20}$$

For simplicity, we choose a parabolic density profile to obtain

$$\langle r_{ion}\rangle = \frac{2\pi\int_o^{r_p} n(r) r_{ion} r dr}{2\pi\int_o^{r_p} n(r) r dr} \qquad (1.21)$$

where

$$n(r) = n_o \left(1-\left(\frac{r}{r_p}\right)^2\right) \text{ and } r_{ion} = 10^{-4}\,\frac{T^{1/2}}{B} \quad . \qquad (1.22)$$

With a uniform temperature profile and a uniform current density profile,

$$B(r) = \frac{\mu_o I r}{2\pi r_p^2} \qquad (1.23)$$

and

$$\langle r_{ion}\rangle = \frac{2\pi\int_o^{r_p} n_o[1 - \frac{r^2}{r_p^2}]\,\frac{10^{-4}T^{1/2}}{\mu_o I r}\,2\pi r_p^2\, r dr}{2\pi\int_o^{r_p} n_o[1-\frac{r^2}{r_p^2}]\, r dr} \qquad (1.24)$$

or

$$S \equiv \frac{\langle r_{ion}\rangle}{r_p} = \frac{8}{3}\,10^{-4}\,T^{1/2}\,\frac{2\pi}{\mu_o I} \quad . \qquad (1.25)$$

Using the Bennett relation, Eq. (1.7), the stability parameter becomes

$$S = \frac{8}{3}\,10^{-4}\,\left(\frac{\mu_o}{16\pi N k}\right)^{1/2}\,\frac{2\pi}{\mu_o} = \frac{5.3\times10^{8}}{N^{1/2}} \quad . \qquad (1.26)$$

For a plasma column with $r_p = 10^{-4}$ m, we find $S > 1$ at a density of

$$n_o < 1.8\times10^{25}\ \mathrm{m}^{-3} \simeq 5\ \mathrm{psia}\ H_2 \quad , \tag{1.27}$$

and we might therefore expect stabilization at relatively low densities. FLR effects have been examined to some extent in linear Z-pinches[23] and may reduce the growth rates for instabilities. However, low density operation is also expected to result in drift induced microinstabilities (e.g., lower hybrid), and these can cause enhanced thermal transport losses. We calculate R, the ratio of electron drift velocity, v_{de}, to ion thermal velocity, v_{ti}, again using the Bennett relation, noting that conditions producing large R are likely to display streaming instabilities.

$$R = \frac{v_{de}}{v_{ti}} = \frac{\frac{I}{\pi r_p^2} \times \frac{1}{n_o e}}{\left(\frac{kT_i}{m_i}\right)^{1/2}} = \frac{\frac{I}{\pi r_p^2}\,\frac{1}{n_o}\,(1.6\times10^{-19})^{-1}}{10^4 T^{1/2}} \tag{1.28}$$

or

$$R = \frac{v_{de}}{v_{ti}} = \frac{I}{T^{1/2}}\,\frac{3.1\times10^{14}}{N} = \left(\frac{16\pi Nk}{\mu_o}\right)^{1/2} \frac{3.1\times10^{14}}{N} = \frac{7.8\times10^{8}}{N^{1/2}} \quad . \tag{1.29}$$

A channel with $r_p = 10^{-4}$ m and $R < 1$ requires

$$n_o > 4\times10^{25}\ \mathrm{m}^{-3} \simeq 12\ \mathrm{psia}\ H_2 \quad . \tag{1.30}$$

For the channel radius chosen in Eqs. (1.27) and (1.30) and with the Bennett relation assumption, it is not clear that a window exists where FLR effects help stabilize modes while microinstabilities do not cause enhanced transport.

A second mechanism which may reduce the growth rate for MHD instabilities in a gas embedded Z-pinch is the drag on the plasma column produced by the surrounding gas blanket. As the plasma kinks, it drags additional mass along with it, which slows down the acceleration. In addition, if the speed of the kinking motion exceeds the sound speed in the adjacent gas, a hydrodynamic shock will be produced, with a resultant pressure force that opposes the kinking. By assuming a dense, low temperature, ionized coronal region surrounding the plasma, calculations[5] predict at least a two order of magnitude reduction in growth rate for m = 1 kink modes. Unfortunately, the coronal region is difficult to investigate both experimentally and analytically; it is not at all obvious that an ionized zone outside the current carrying channel will indeed be formed.[24]

Bremsstrahlung radiation will produce a local photoionization rate in hydrogen for wavelengths shorter than the threshold at $\lambda_{max} = 912$ Å. This rate must be balanced with recombination processes to compute an ionization fraction for the surrounding gas. The bremsstrahlung flux from a uniform column of density n_p, radius r_p, and temperature T_p, at a radius $r > r_p$ is

$$\Phi(r,\lambda) = 5.4\times10^{-20} \frac{n_p^2}{T_p^{1/2}\lambda} e^{-12600/\lambda T_p} \frac{r_p^2}{r} \frac{\text{photons}}{\text{m}^2\text{s Å}} \qquad (1.31)$$

where λ is in Å, and we have assumed no absorption in the intervening region. The photoionization cross section for

$$h\nu + H \rightarrow H^+ + e^- \qquad (1.32)$$

is given approximately by Kramers' rule,[25]

$$\sigma(\lambda) = 10^{-30}\lambda^3 \quad , \qquad (1.33)$$

with λ in Å, and we find

$$\frac{dn_e}{dt} = \frac{\#\text{electron-ion pairs}}{m^3 s} = n_o \int_o^{\lambda_{max}} \sigma(\lambda)\Phi(r,\lambda)d\lambda \tag{1.34}$$

where n_o is the neutral density. The rise in cross-section at long wavelengths dominates the flux increase at short wavelengths, for any plasma temperature of interest, and we can approximate the exponential in Eq. (1.31) by unity. Thus

$$\frac{dn_e}{dt} \lesssim 1.4\times10^{-41} \frac{n_o n_p{}^2}{T_p^{1/2}} \frac{r_p^2}{r} \quad . \tag{1.35}$$

We next compare radiative recombination to three-body recombination to determine the dominant process for typical plasma conditions. The recombination rates are expressed by[26]

$$\left(\frac{dn_e}{dt}\right)_{recomb} = - \alpha n_e^2 \tag{1.36}$$

where n_e is the density of electrons (or ions) in the corona;

$$\alpha_{Rad} = 5.2\times10^{-20} \left(\frac{E_b}{T_c}\right)^{1/2}$$

$$\times\left[0.429 + \frac{1}{2} \ell n \left(\frac{E_b}{T_c}\right) + .469 \left(\frac{E_b}{T_c}\right)^{-1/3}\right] \tag{1.37}$$

and

$$\alpha_{3_{body}} = 1.4\times10^{-43} n_e \left(\frac{E_b}{T_c}\right)^2 e^{\frac{E_b}{4T_c}} \tag{1.38}$$

where E_b is the binding energy (13.6 eV) and the subscript c refers to the corona. Notice that $\alpha_{3_{\mathrm{body}}}$ is proportional to n_e, as would be expected for a three-body process. Using $n_e > 1\times10^{23}\ \mathrm{m}^{-3}$ and $T_c = 5$ eV, we find

$$\alpha_{\mathrm{Rad}} = 1\times10^{-19}\ \mathrm{m}^3/\mathrm{s} \tag{1.39}$$

$$\alpha_{3\mathrm{body}} > 2\times10^{-19}\ \mathrm{m}^3/\mathrm{s} \quad ,$$

and we therefore compute the ionization fraction of the corona by equating the bremsstrahlung induced photoionization rate with the three-body recombination rate. From Eqs. (1.35) and (1.38) we find

$$1.4\times10^{-41}\ \frac{n_o n_p^2}{T_p^{1/2}}\ \frac{r_p^2}{r} = \left[1.4\times10^{-43} n_e \left(\frac{E_b}{T_c}\right)^2 \left(e^{E_b/4T_c}\right)\right] n_e^2 \quad . \tag{1.40}$$

If we assume a fully ionized core with the initial fill density, then $n_o = n_p$, and Eq. (1.40) becomes

$$f = \frac{n_e}{n_o} = \left[1.4\times10^{-41}\ \frac{r_p^2}{r}\ \frac{1}{T_p^{1/2}}\ \frac{1}{1.4\times10^{-43}\left(\frac{E_b}{T_c}\right)^2\ e^{E_b/4T_c}}\right]^{1/3} \tag{1.41}$$

where f is the fractional ionization of the corona. For the conditions

$$r_p = 10^{-4}\ \mathrm{m} \qquad T_p = 100\ \mathrm{eV} \qquad T_c = 3\ \mathrm{eV} \tag{1.42}$$

$$r = 10^{-3}\ \mathrm{m} \qquad E_b = 13.6\ \mathrm{eV}$$

we obtain

$$f = 0.01 \text{ or } 1\% \text{ ionization.} \tag{1.43}$$

Strong recombination thus keeps the coronal region from reaching a high equilibrium ionization.

Three-body recombination ultimately will lead to full ionization of the corona. In this process, two electrons collide in the vicinity of an ion, and one electron loses enough energy to be captured and form a neutral atom while the other electron gains energy. Eventually, these free electrons will cause impact ionization, converting bremsstrahlung energy indirectly into ionization. The time scale for this process is too large to effectively create a corona, however, as we can see from energy considerations. For the conditions of (1.42) with $n_p = 10^{26}\ m^{-3}$, the bremsstrahlung power is

$$p_{BR} = 1.7\times10^{-38}\ n_p^2\ T_p^{1/2}\ \frac{\text{watt}}{m^3} \tag{1.44}$$

or

$$P_{BR} = p_{BR}\times(\pi r_p^2) \simeq 5\times10^7\ \frac{\text{watt}}{m}\ . \tag{1.45}$$

The energy required to ionize the corona is

$$E_{ion} \simeq \frac{13.6\ \text{eV}}{\text{ion pair}} \times n_p \times \pi(r^2-r_p{}^2) \simeq 700\ \frac{\text{joule}}{m}\ , \tag{1.46}$$

hence

$$\tau_{ionization} \simeq \frac{E_{ion}}{P_{BR}} \simeq 14\ \mu s > \tau_{OH}\ . \tag{1.47}$$

It is possible that thermal conduction at early (first 10 ns of current flow) times will provide the radial heat transport needed to ionize the corona. For low plasma channel temperatures, electron thermal conduction dominates ion thermal conduction, and we can estimate the efficiency of this mechanism for creating the corona. The energy deposited per unit volume per unit time in the corona is

$$P_{TC} \simeq \nabla\cdot q \simeq \nabla\cdot(K_{\parallel e}\nabla kT_p) \simeq K_{\parallel e}\,\frac{kT_p}{r_p^2} \qquad (1.48)$$

where q is the heat flux. Braginskii[27] gives

$$K_{\parallel e} = 3.2\,\frac{n_p kT_p \tau_e}{m_e} \qquad (1.49)$$

with

$$\tau_e = \frac{3.44\times10^{11}\ T_p^{3/2}}{n_p \ell n\Lambda}\ . \qquad (1.50)$$

For $T_p = 30$ eV and $n_p = 10^{26}$ m^{-3},

$$K_{\parallel e} \simeq 2\times10^{26}\ m^{-1}s^{-1}\ . \qquad (1.51)$$

Thus for $r_p = 10^{-4}$ m, we obtain

$$P_{TC} \simeq 10^{17}\,\frac{\text{watt}}{m^3}\ . \qquad (1.52)$$

If the corona density is also 10^{26} m^{-3} and the energy needed to produce an ion-electron pair is 13.6 eV, the time to ionize the corona by electron thermal conduction is

$$\tau_{\text{ionization}} = \frac{13.6\ \text{eV} \times 1.6 \times 10^{-19} \times 10^{26}}{10^{17}} \simeq 2 \times 10^{-9}\ \text{s} \quad , \tag{1.53}$$

and we find that thermal conduction is far more effective than radiation at creating a corona.

The coronal region, while contributing to a reduction in the instability growth rate, may present a mechanism by which current is diverted from the central channel. As the corona heats, its resistivity drops, and the penetration time for new current increases; thus current will begin to flow in the corona. For a fully ionized corona with $r = 10^{-3}$ m, $n = 10^{26}\ \text{m}^{-3}$, and $T = 3.5$ eV, the coronal resistivity is

$$\eta_c = \frac{10^{-4} \ln\Lambda}{T^{3/2}} \simeq 2.8 \times 10^{-5}\ \Omega\text{-m} \tag{1.54}$$

and the resistive diffusion time is

$$\tau_R \simeq \frac{\mu_o r^2}{\eta_c} \simeq 45\ \text{ns} \quad . \tag{1.55}$$

This time is comparable to the current risetime in a practical device, and current may be prevented from penetrating into the central channel.

In addition to providing the ohmic heating, it is a requirement that current be distributed in a core region to insure cross-field thermal and particle diffusion both axially and radially. In the high current, high temperature regime, ion thermal conductivity will become a severe loss mechanism to the electrodes and the neutral gas if a magnetic field of high strength is not embedded in the channel. We can compare the ohmic heating input power rate to ion thermal conductivity parallel to B in analogy to Eq. (1.48). Using

$$K_{\parallel}^{ion} = \frac{3.9\ n_p k T_p \tau_i}{m_i} \qquad (1.56)$$

with

$$\tau_i = \frac{2.09\times10^{13}}{n_p \ell n\Lambda} T_p^{3/2} \qquad (1.57)$$

and

$$T_p = 100\ \text{eV},\ n_p = 10^{26}\ \text{m}^{-3},\ \text{and}\ r_p = 10^{-4}\ \text{m},$$

we find

$$P_{ion} = \nabla\cdot q \simeq K_{\parallel}^{ion} \frac{kT_p}{r_p^2} \simeq 2\times10^{17}\ \frac{\text{watt}}{\text{m}^3} \quad . \qquad (1.58)$$

The ohmic heating rate is

$$P_{OH} = \eta j^2 \qquad (1.59)$$

where j is the current density and η is the resistivity. For Bennett equilibrium at the above conditions, $I \simeq 45$ kA, and

$$j \simeq \frac{I}{\pi r_p^2} = 1.4\times10^{12}\ \frac{\text{A}}{\text{m}^2} \quad . \qquad (1.60)$$

Using Eq. (1.54) for the plasma resistivity, we obtain

$$\eta_p = \frac{10^{-4}\ \ell n\Lambda}{T^{3/2}} \simeq 5.6\times10^{-7}\ \Omega\text{-m} \tag{1.61}$$

and

$$P_{OH} \simeq 10^{18}\ \frac{\text{watt}}{\text{m}^3}\quad . \tag{1.62}$$

Comparing Eqs. (1.62) and (1.58), we find that if the thermal conduction is not cross-field, this loss mechanism represents a sizable fraction of the ohmic heating input and will have a detrimental effect on the plasma temperature. Even with cross-field thermal conduction, particles within a Larmor radius of the channel axis may execute unusual orbits which can carry them rapidly toward the electrodes.[28] A complete analysis of the energy loss from these particles may in fact set a length constraint on the column for reactor conditions.

The collisionality of an HDZP plasma governs its behavior (eg., runaway electrons), and we next estimate the electron mean free path. For $n_p = 10^{26}\ \text{m}^{-3}$ and $T_p = 100$ eV,

$$\lambda_{mfp} \simeq v_{T_e}\tau_{ee} \simeq \frac{1.4\times10^{17}\ T_p^2}{n_p \ell n\Lambda} \simeq 2.5\times10^{-6}\ \text{m} \ll \ell \tag{1.63}$$

where ℓ is a typical column length, $\ell \sim 10^{-1}$ m. As a comparison, we can compute the Debye length for these conditions,

$$\lambda_{D_e} = 7.4\times10^{3}\ \left(\frac{T_p}{n_p}\right)^{1/2} \simeq 7.4\times10^{-9}\ \text{m}\quad . \tag{1.64}$$

Because the Debye length is much shorter than the collision mean free path, we expect the statistical description of the plasma to be valid, with long range encounters dominant over binary large angle scattering. For these conditions, the plasma parameter is

$$g = \frac{1}{n_p \lambda^3_{D_e}} \simeq 2.5\times10^{-2} << 1 \text{ as required.} \tag{1.65}$$

During the early formation phase of a high density plasma, however, the plasma parameter exceeds unity and transport processes will become anomalous; for example, Spitzer resistivity will no longer be applicable. We find for $n_p = 10^{26}$ m^{-3} that $g > 1$ for $T_p < 8.5$ eV. Calculations in this regime are quite complicated, and we hope the formation phase is brief enough that the column is not seriously affected by $g > 1$ processes.

The high plasma density also has a deleterious effect on conventional diagnostics because of the large plasma frequency, ω_{pe}. For $n_p = 10^{26}$ m^{-3},

$$\omega_{pe} = \left(\frac{n_p e^2}{\varepsilon_o m_e}\right)^{1/2} = 5.7\times10^{14} \text{ s}^{-1} \quad , \tag{1.66}$$

and optical transmission is cutoff for

$$\lambda > \lambda_{MAX} \simeq 3.3 \ \mu \quad . \tag{1.67}$$

Significant refraction and absorption will be observed in the infra-red and red, and one is dependent on ultra-violet sources for most optical diagnostics.

In any reactor scheme involving a high β plasma, the total cyclotron emission radiated power exceeds bremsstrahlung by a significant factor. For $T_p = 10^4$ eV and $\beta = 1$,

$$\frac{P_c}{P_B} = \frac{5\times10^{-44} n_p{}^2 T_p{}^2 \ \text{watt/m}^3}{1.7\times10^{-38} n_p{}^2 T_p{}^{1/2} \ \text{watt/m}^3} \simeq 3 \quad . \tag{1.68}$$

The actual radiation loss from cyclotron emission is less than P_c because we expect most of the radiation to be reabsorbed. The peak field is at the column surface,

$$B_p = \frac{\mu_o I}{2\pi r_p} \simeq 9\times10^2 \text{ T} \quad , \tag{1.69}$$

for $I = 10^6$ A and $r_p = 2\times10^{-4}$ m, and

$$\omega_{ce} = \frac{eB}{m_e} \simeq 1.6\times10^{14} \text{ s}^{-1} < \omega_{pe} \quad . \tag{1.70}$$

Following Rose and Clark[30] we calculate the dimensionless transparency coefficient, K_L , which measures the absorption of cyclotron radiation in the plasma. For $n_e = n_i = 10^{26}$ m^{-3}, $T_e = T_i = 10^4$ eV, and $r_p = 2\times10^{-4}$ m, the dimensionless plasma size is

$$L \simeq \frac{\omega_{pe}^2}{\omega_{ce}} \frac{r_p}{c} \simeq 1.3\times10^3 \quad . \tag{1.71}$$

Trubnikov[31] has determined that for these conditions,

$$K_L \simeq 0.006 \quad . \tag{1.72}$$

Thus less than 1% of the total cyclotron power density is lost, and bremsstrahlung is the dominant radiation loss mechanism for a hydrogenic HDZP plasma at D-T fusion temperatures.

The strength of the azimuthal field, B_θ, in an HDZP plasma is indicated by [illegible] and we recognize the futility of externally generating a comparable axial field for conventional stabilization. This high field motivates a comparison between the stored plasma energy and the field energy for a reactor-type HDZP at Bennett equilibrium, assuming uniform current density. With a return conductor at radius r_{OUT}, the plasma inductance is

$$L = \frac{\mu_o \ell}{2\pi} \left(\ell n \frac{r_{OUT}}{r_p} + \frac{1}{4}\right) \quad , \tag{1.73}$$

the stored magnetic energy is

$$W_B = \frac{1}{2} LI^2 \quad , \tag{1.74}$$

and the plasma energy is

$$W_p = 3NkT\ell \tag{1.75}$$

where N is the line density. Using the Bennett relation, (1.7),

$$\frac{W_p}{W_B} = \frac{3NkT\ell}{\frac{\mu_o \ell}{4\pi}\left(\ell n \frac{r_{OUT}}{r_p} + \frac{1}{4}\right)\frac{16\pi NkT}{\mu_o}} = \frac{3}{4\left(\ell n \frac{r_{OUT}}{r_p} + \frac{1}{4}\right)} \quad . \tag{1.76}$$

The prototype HDZP device has $r_{OUT} = 0.2$ m, and for $r_p = 10^{-4}$ m, we obtain

$$\frac{W_p}{W_B} = 9.6 \times 10^{-2} \approx 10\% \quad . \tag{1.77}$$

As a result of the logarithmic dependence on r_{OUT}, no substantial increase in efficiency is observed until r_{OUT} approaches 10^{-3} m.

In conclusion, the high density, small spatial scale, short pulse regime appears promising for gas embedded linear Z-pinch plasmas, in spite of possible instabilities, thermal conduction losses, and the difficulty of performing diagnostics in this relatively unexplored area of plasma physics.

References for Chapter 1

1. D. J. Rose and M. Clark, *Plasmas and Controlled Fusion* (MIT Press, Cambridge, Massachusetts, 1961) Chapter 14; see also S. Glasstone and R. H. Lovberg, *Controlled Thermonuclear Reactions* (Van Nostrand, Princeton, New Jersey, 1960) Chapter 7.

2. F. F. Chen, *Introduction to Plasma Physics* (Plenum Press, New York, 1974), p.281.

3. H. Alfvén and E. Smars, Nature *188*, 801 (1960).

4. C.-G. Fälthammar, Phys. Fluids *4*, 1145 (1961).

5. W. M. Manheimer, M. Lampe, and J. P. Boris, Phys. Fluids *16*, 1126 (1973).

6. E. A. Smars, Arkiv För Fysik *Band 29*, 97 (1964).

7. R. Papoular, in *Laser Plasmas and Nuclear Energy*, H. Hora, edited by Y. Ksander (Plenum Press, New York, 1975), p. 125.

8. C. S. Naiman, M. Y. DeWolf, I. Goldblatt, and J. Schwartz, Phys. Rev. *146*, 133 (1966).

9. R. E. Pechacek, Bull. Am. Phys. Soc. *17*, 974 (1972).

10. D. W. Koopman and T. D. Wilkerson, J. of Appl. Phys. *42*, 1883 (1971).

11. M. Raleigh, Naval Research Laboratory, personal communication, 1981.

12. M. Raleigh, J. R. Greig, R. E. Pechacek, and E. Laikin, NRL Memorandum Report 4380, (1981).

13. J. N. Olsen, Sandia National Laboratory, personal communication, 1981.

14. K. W. Struve, C. W. Hartman, R. H. Munger, and J. W. Shearer, Bull. Am. Phys. Soc. *20*, 1296 (1975).

15. R. S. Pease, Proc. Phys. Soc. *70*, 11 (1957).

16. R. L. Hagenson, A. S. Tai, R. A. Krakowski, and R. W. Moses, Los Alamos Scientific Laboratory report LA-8186-MS (1980).

17. W. H. Bennett, Phys. Rev. *45*, 890 (1934).

18. J. E. Hammel, F. C. Jahoda, J. Shlachter, and D. A. Platts, Bull. Am. Phys. Soc. *24*, 1078 (1979).

19. B. B. Kadomtsev, in *Reviews of Plasma Physics*, edited by M. A. Leontovich (Consultants Bureau, New York, 1966), Vol. 2, pp. 153-199.

20. J. Shiloh, A. Fisher, and N. Rostoker, Phys. Rev. Lett. *40*, 515 (1978); see also C. Stallings, K. Childers, I. Roth, and R. Schneider, Appl. Phys. Lett. *35*, 524 (1979).

21. W. L. Baker, M. C. Clark, J. H. Degnan, G. F. Kiuttu, C. R. McClenahan, and R. E. Reinovsky, J. Appl. Phys. 49, 4694 (1978).

22. C. Stallings, K. Nielsen, and R. Schneider, Appl. Phys. Lett. 29, 404 (1976); see also F. S. Felber and N. Rostoker, Maxwell Laboratory report MLR-937, (1980).

23. K. W. Struve, Lawrence Livermore Laboratory report UCRL-52993 (1980).

24. R. H. Lovberg, University of California, San Diego, personal communication, 1979.

25. Atomic Data for Controlled Fusion Research, Oak Ridge National Laboratory report ORNL-5207, edited by C. F. Barnett, et al., Vol. I, pp. B.1.4-B.1.5 (1977).

26. R. C. Elton, in Methods of Experimental Physics, edited by H. R. Griem and R. H. Lovberg (Academic Press, New York, 1970), Vol. 9, part A, 154.

27. S. I. Braginskii, in Reviews of Plasma Physics, edited by M. A. Leontovich (Consultants Bureau, New York, 1966), Vol. 1, pp. 205-311.

28. M. G. Haines, J. Phys. D: Appl. Phys. 11, 1709 (1978).

29. J. E. Hammel, Los Alamos Scientific Laboratory report LA-6203-MS (1976).

30. D. J. Rose and M. Clark, Plasmas and Controlled Fusion (MIT Press, Cambridge, Massachusetts, 1961), p. 251.

31. B. A. Trubnikov and V. S. Kudryavtsev, Proc. 2nd U.N. Conf. on Peaceful Uses of Atomic Energy, Vol. 31 (United Nations, Geneva, 1958), pp. 93-98.

32. M. G. Haines, Physical Society of London Proceedings 76, 250 (1960).

Chapter 2. Analytical and Computational Modeling

One theoretical approach to describing the plasma produced in an HDZP experiment is to develop a magnetohydrodynamic (MHD) code which divides the plasma into fluid cells and traces the time evolution of these cells through governing difference equations. The space mesh may be allowed to move (Lagrangian code) or it may be fixed (Eulerian code), and the complexity of the code is determined by the number of spatial dimensions in the mesh and the number of physical processes included in the code (e.g., radiation transport, recombination ...).[1] A number of codes presently exist which can be applied to HDZP plasmas, including RAVEN[2] (one-dimensional axially and azimuthally symmetric Lagrangian MHD) and MANIAC[3-6] (two-dimensional azimuthally symmetric Eulerian MHD). These codes, however, can be costly to run and difficult to interpret. Furthermore, they are practically impossible to check in detail by experiment. Observations of HDZP plasmas are typically limited to a few global parameters as a function of time. Present diagnostics can only determine load current, radius, temperature, and the radial profile of electron density. A relatively simple, inexpensive-to-run, self-consistent global or zero-dimensional MHD model which can predict the temporal behavior of plasma current, temperature, and radius, has therefore been developed and applied to both present and future experimental regimes.

This chapter outlines the development and characteristics of the global MHD model used to describe HDZP plasmas. We begin with a simple analysis of the equilibrium configuration for a Z-pinch, first performed by Bennett.[7] This equilibrium (Bennett equilibrium) is then supplemented by a simple energy balance and results in an asymptotic condition for the plasma (Pease limit).[8] Incorporating time dependence into this analysis leads to a set of quasi-equilibrium curves (Hammel curves).[9] These curves prescribe the time dependence of the current carried by a spatially static plasma. Inclusion of an adiabatic work term then yields a model which can be applied to a given set of experimental conditions (adiabatic model).[10] Finally, this adiabatic model is augmented by an inertial term, allowing deviations from Bennett equilibrium, and becomes our global MHD model. This model, its solution for various test problems, and a comparison with other models, will be described in detail.

The variables throughout this chapter which will be used to describe the cylindrical plasma are T (plasma temperature), I (plasma current), n (ion or electron density), and r (plasma radius) (Fig. 2.1). All quantities are expressed in MKS units except T, which is typically expressed in electron volts (1 eV = 11600 K^o). We shall make several assumptions in developing this model and will justify most of these through calculation.

Assumption 1 Constant line density N

The line density is the number of particles of one species (electrons or ions) per unit length of the plasma column. By assuming this number to be constant, we are not allowing for ionization of the surrounding gas through shock heating, radiation, thermal conduction, or thermal convection; this is a serious limitation to the model. While computer codes exist which can allow for changes in line density,[11] even the most sophisticated models cannot presently address all aspects of this difficult problem.

Recombination processes will tend to decrease the initial plasma line density, and without a source term, the density will decay with a characteristic time. For the plasma conditions in the prototype HDZP experiment, three-body recombination is dominant over radiative recombination[12] and we can estimate τ_{recomb} for T = 100 eV and $n = 10^{26}$ m^{-3},

$$\frac{dn_e}{dt} = - \alpha_{3body}\, n_e^2 \simeq - n_e/\tau_{recomb}$$

$$\tau_{recomb} \simeq (2.7\times10^{-19}\ m^3s^{-1})^{-1}\ \frac{1}{10^{26}\ m^{-3}} \simeq 40\ ns \quad . \qquad (2.1)$$

We are therefore reasonably justified in ignoring recombination on the time scale of the prototype HDZP experiment, approximately 60 ns.

Assumption 2 Ion and Electron Equilibration $\qquad T_i = T_e = T$

We can compute the equilibration time between electrons and ions for conditions ($T_i \sim T_e$ = 100 eV, $n = 10^{26}$ m^{-3}) which result in $\ell n\Lambda \simeq 7$.

$$\tau_{eq} \simeq \frac{10^6\ T^{3/2}}{3.2\times10^{-9}\ n\ell n\Lambda} \simeq 0.4\ ns \quad . \qquad (2.2)$$

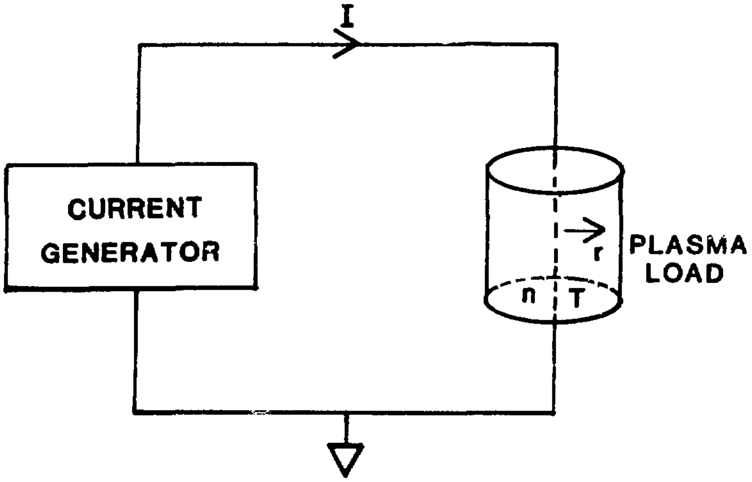

Fig. 2.1 Block diagram of High Density Z-Pinch

The equilibration time, τ_{eq}, is short compared to the experimental times of interest and justifies this assumption.

Assumption 3 Quasineutrality $n_e = n_i = n$

We compute the Debye length for a plasma with the conditions of the previous assumption,

$$\lambda_{D_e} = 7.4\times10^3 \left(\frac{T_e}{n}\right)^{1/2} \simeq 0.007\ \mu \quad . \tag{2.3}$$

The Debye length is much smaller than the spatial scale of the experimentally generated plasmas ($\lesssim$ 1000 μ) and justifies quasineutrality.

Assumption 4 Isothermal column $T \neq T(r)$

We make an approximation to the time required to smooth out temperature variations across the column by the thermal conductivity, K, recognizing that our choice of the column radius as the spatial scale for temperature gradients is crude and inconsistent with heat loss terms used in subsequent analyses. We also neglect the spatial variation in K.

$$3nk\,\frac{dT}{dt} \simeq -\,\nabla\cdot q \simeq -\,K\nabla^2 kT \simeq 3nk\,\frac{T}{\tau_{isotherm}} \tag{2.4}$$

$$\tau_{isotherm} \simeq \frac{-3nkT}{K\nabla^2 kT} \simeq \frac{3nkT}{KkT}\,r_p{}^2 \tag{2.5}$$

We use T = 200 eV, r_p = 100 μ, $n = 10^{26}\ m^{-3}$ and Bennett equilibrium (derived in section 2.1) to determine K. For these conditions, we use $K_\perp^i$, the ion perpendicular conductivity, with

$$K_\perp^i = 2\,\frac{nkT}{m_i\Omega_{ci}^2\tau_i} \quad . \tag{2.6}$$

For I = 63 kA, $B = 1.3\times10^2$ T, $\Omega_{ci} = 1.3\times10^{10}\ s^{-1}$, and $\tau_i = 3\times10^{-11}$ s, we find

$$\tau_{isotherm} \simeq \frac{m_i r_p^2 \Omega_{ci}}{kT} (\Omega_{ci} \tau_i) \simeq 2.6 \text{ ns} \quad . \qquad (2.7)$$

We therefore might expect reasonably uniform temperatures across the channel on the experimental time scale.

2.1 Equilibrium and Quasi-Equilibrium

Our closure equation of state for the plasma column is

$$p_{TOT} = n_i kT_i + n_e kT_e = 2nkT$$

where p_{TOT} (total pressure) and n (individual species density) are both functions of radius and time. We next write the MHD momentum equation for a fully ionized, hydrogenic, single fluid plasma and discuss various simple forms.

$$mn \frac{D\underset{\sim}{v}}{Dt} = - \underset{\sim}{\nabla} p + \underset{\sim}{j} \times \underset{\sim}{B} - \nabla \cdot \underset{\approx}{\pi} \qquad (2.8)$$

where D/Dt is the convective derivative, i.e., the time rate of change of a quantity within a given element of fluid (Lagrangian approach). We use $m = m_{proton}$, j is the current density, B is the magnetic field, and $\underset{\approx}{\pi}$ is the off-diagonal pressure tensor. The left hand side of Eq. (2.8) is the inertial term, used in the global MHD model; the right hand side of (2.8) expresses the forces resulting from plasma pressure, magnetic field pressure, and viscous effects. The geometry of our model presupposes axial current and therefore azimuthal magnetic field, and all quantities are assumed to have only radial spatial dependence. Ignoring the inertial and viscous terms temporarily, we obtain a fluid element equilibrium equation,

$$\underset{\sim}{\nabla} p = \underset{\sim}{j} \times \underset{\sim}{B} \quad . \qquad (2.9)$$

Our goal is to assemble a set of global equations, and we begin by integrating

(2.9) over the plasma column. We use Maxwell's equations with no displacement current,

$$\underset{\sim}{\nabla}\times\underset{\sim}{B} = \mu_o \underset{\sim}{j} = \frac{1}{r}\frac{\partial}{\partial r}(rB)\,\hat{e}_z \quad , \tag{2.10}$$

so

$$\underset{\sim}{j}\times\underset{\sim}{B} = \frac{-B}{\mu_o r}\frac{\partial}{\partial r}(rB)\,\hat{e}_r = -\frac{1}{\mu_o r^2}\frac{\partial}{\partial r}\left(\frac{r^2B^2}{2}\right)\hat{e}_r \quad . \tag{2.11}$$

Our equation of state yields

$$\underset{\sim}{\nabla}p = \frac{\partial p}{\partial r}\,\hat{e}_r = 2\ kT\,\frac{\partial n}{\partial r}\,\hat{e}_r \quad . \tag{2.12}$$

Hence

$$2\ kT\,\frac{\partial n}{\partial r}\,\hat{e}_r = \frac{-1}{\mu_o r^2}\frac{\partial}{\partial r}\left(\frac{r^2B^2}{2}\right)\hat{e}_r \quad . \tag{2.13}$$

We multiply both sides of (2.13) by πr_p^2 and integrate over the column, where r_p is the channel radius;

$$2\pi\ kT\int_o^\infty r^2\,\frac{\partial n}{\partial r}\,dr = -\frac{\pi}{\mu_o}\int_o^\infty \frac{\partial}{\partial r}\left(\frac{r^2B^2}{2}\right)dr \quad . \tag{2.14}$$

Integrating the LHS of (2.14) by parts,

$$2\ kT\int_o^\infty \pi r^2\,\frac{\partial n}{\partial r}\,dr = 2\ kT\pi r^2 n\,\Big|_o^\infty - 2\ kT\int_o^\infty 2\pi r n dr = -\ 2\ kTN \quad , \tag{2.15}$$

where n goes to zero at large radii, and the line density N is given by

$$N = \int_o^\infty 2\pi r n dr \quad . \tag{2.16}$$

Examining the RHS of Eq. (2.14) and using Maxwell's equation

$$\frac{\mu_o I}{2\pi} = rB \Big|^{\infty} \tag{2.17}$$

we obtain

$$\int_o^\infty \frac{\partial}{\partial r} \left(\frac{r^2 B^2}{2}\right) dr = \frac{\mu_o^2 I^2}{8\pi^2} \quad . \tag{2.18}$$

The global momentum balance equation (2.14) thus becomes

$$\mu_o I^2 = 16\pi NkT \tag{2.19}$$

or

$$I^2 = 1.6\times10^{-12} \; NT \quad . \tag{2.20}$$

This Bennett equilibrium equation is an expression of a balance between plasma pressure and magnetic field pressure. We note two important assumptions that have gone into this analysis. First, we have assumed $B_\theta = B_\theta(r)$ or, alternatively, that current is only flowing axially and is only radially dependent. If current were to flow in discrete filaments parallel to the cylindrical axis of symmetry, the Bennett equilibrium would no longer be valid. Second, we have required $B_z = B_r = 0$. This assumption is violated for a column which coils up, producing a solenoidal B_z which can contribute to the overall pressure balance. Nevertheless, for columns which appear cylindrically symmetric in Schlieren photographs, the Bennett equilibrium expression provides a useful estimate of plasma temperature, as both N and I are measurable. As an example, for a column with $r = 100\ \mu$, $n(r) = n_0 = 10^{26}\ \mathrm{m}^{-3}$, and $I = 100$ kA, we find that $T_{\mathrm{Bennett}} = 500$ eV.

Before returning to the MHD momentum equation, we examine the MHD energy equation,

$$\frac{3}{2}\frac{Dp}{Dt} + \frac{5}{2}\, p\nabla\cdot\underset{\sim}{v} = \eta_\perp j^2 - \nabla\cdot\underset{\sim}{q} - R \quad , \tag{2.21}$$

where $\eta_\perp$ is the plasma resistivity for current perpendicular to the field, q is the heat flux, and R is the loss of energy associated with radiation. The first term on the LHS of (2.21) is an expression of the change in internal energy of a fluid element; the second term is related to the work done by a fluid element during expansion against the magnetic field. The first term on the RHS is the joule or ohmic heating of the plasma and couples the electrical circuit to the load. The heat flux term is essentially the expression used in Eq. (2.4). The models which we will analyze ignore radiation transport; we treat only bremsstrahlung radiation and assume that it is lost completely from the system. Our choice of a hydrogenic $Z = 1$ plasma reduces the importance of line radiation. We simplify Eq. (2.21) by re-expressing the work term using the continuity equation,

$$\nabla\cdot\underset{\sim}{v} = -\frac{1}{n}\frac{dn}{dt} \quad , \tag{2.22}$$

demonstrating that all the explicit time dependence of Eq. (2.21) is on the LHS. Thus we can look at a steady state solution balancing the ohmic heating input against the bremsstrahlung loss,

$$\eta_\perp j^2 = R \quad . \tag{2.23}$$

For simplicity, we assume a constant radius channel with uniform density, temperature, and current; we note, however, that these profiles are not consistent with pressure balance. We can express the ohmic heating term as

$$\eta_\perp \frac{I^2}{(\pi r_p^2)^2}$$

where r_p is the channel radius and we use cross-field Spitzer resistivity,

$$\eta_\perp = \frac{10^{-4}\ \ell n\Lambda}{T^{3/2}} \quad . \tag{2.24}$$

Bremsstrahlung loss is given by

$$R = 1.7\times10^{-38}\ n_p^2\ T^{1/2}\ \text{watt/m}^3 \tag{2.25}$$

where n_p is the column density for a given species. We use the definition of line density,

$$N = \int_o^{r_p} 2\pi r n_p dr = \pi r_p^2\ n_p \quad , \tag{2.26}$$

to obtain

$$10^{-4}\ \ell n\Lambda \frac{I^2}{T^{3/2}} = 1.7\times10^{-38}\ N^2 T^{1/2} \quad .$$

To complete this calculation of asymptotic energy balance, we assume Bennett equilibrium, (2.19), to eliminate the temperature, yielding

$$I = \left[\frac{10^{-4}\ \ell n\Lambda}{1.7\times10^{-38}}\left(\frac{16\ \pi k}{\mu_o}\right)^2\right]^{1/2} \text{ amperes} \quad . \tag{2.27}$$

This rather surprising result reveals that there is an asymptotic current for a plasma in Bennett equilibrium which is independent of channel radius and density, ignoring small changes in $\ell n\Lambda$, with a value of

$$I_p \simeq 1.3 \text{ MA} \quad . \tag{2.28}$$

This current is referred to as the Pease current and is applicable to a Bennett equilibrium plasma which balances ohmic heating against bremsstrahlung. The value of I_p is weakly dependent on the choice of pressure profile. The Pease current represents a fundamental limit to the axial current through a steady state Z-pinch, and it is essential to the ohmically heated HDZP concept that the Bennett temperature at this limit be of thermonuclear interest (i.e., ~ 10 keV) for realizable channels. We choose $r_p = 300\ \mu$ and $n_p = 5\times10^{26}\ m^{-3}$ (10 atm) and obtain

$$T_{Pease} = \frac{I_p^2}{1.6\times10^{-12}N} = 10^4 \text{ eV} \quad . \tag{2.29}$$

We next consider a channel similar to that used in the Pease current analysis (constant radius, constant and uniform density, uniform current, and uniform temperature) with the additional feature of a time dependent temperature. This will provide us with a set of quasi-equilibrium curves describing the time dependent approach to the Pease current. Again we assume Bennett equilibrium at all stages of the channel development and consider only ohmic heating, bremsstrahlung, and the change in internal energy in Eq. (2.21). For constant density,

$$\frac{3}{2}\frac{Dp}{Dt} = \frac{3}{2}\,2n_p k\,\frac{dT}{dt} \tag{2.30}$$

and we get

$$3n_p k \frac{dT}{dt} = \frac{10^{-4}\ \ell n\Lambda}{T^{3/2}} \frac{I^2}{(\pi r_p^2)^2} - 1.7\times10^{-38} \frac{N^2}{(\pi r_p^2)^2} T^{1/2} \quad . \tag{2.31}$$

Internal Energy   Ohmic Heating   Bremsstrahlung

Using the Bennett equilibrium expression to eliminate I arbitrarily in favor of T, we obtain

$$\frac{dT}{dt} = \frac{A}{T^{1/2}} - BT^{1/2} \tag{2.32}$$

where A and B are constants,

$$A = \frac{9.33\times10^3\ n}{N}$$

$$B = 3.54\times10^{-20}\ n \quad ,$$

and we have chosen $\ell n\Lambda = 7$. With an initial condition of $T(0) = 0$, this differential equation may be solved analytically, yielding

$$Bt = -\ 2T^{1/2} + \left(\frac{A}{B}\right)^{1/2} \ell n \left(\frac{\left(\frac{A}{B}\right)^{1/2} + T^{1/2}}{\left(\frac{A}{B}\right)^{1/2} - T^{1/2}}\right) \quad . \tag{2.33}$$

This solution[9,20] is then a prescription for T(t) (or I(t) through the Bennett equilibrium) with only the number density, n_p, and line density, N, as adjustable parameters, (Fig 2.2). We have therefore arrived at a set of curves (Hammel curves) to describe the required approach to the Pease current, assuming Bennett equilibrium, ohmic heating, bremsstrahlung, and a constant radius, constant density channel. Let us examine the characteristic risetime, τ_{OH}, for these curves. First, the asymptotic temperature, T_p, at the Pease current is

$$T_p = A/B = \frac{2.64\times10^{23}}{N} \quad . \tag{2.34}$$

To obtain a characteristic time, we set $T = 1/2\ T_p$ in Eq. (2.33). Then

$$B\tau_{OH} = \left(\frac{A}{B}\right)^{1/2} \times (0.35) \tag{2.35}$$

or

$$\tau_{OH} \simeq \frac{A^{1/2}}{.9\ B^{3/2}} = \frac{5.1\times10^{30}}{nN^{1/2}} = \frac{2.9\times10^{30}}{rn^{3/2}} \quad . \tag{2.36}$$

Experimental constraints limit us to current rise rates of $\dot{I} \lesssim 4\times10^{12}$ A/s. At a current equal to 0.71 I_p (900 kA) we expect a temperature of $1/2\ T_p$ through the Bennett relation, thus we require $\tau_{OH} \gtrsim 200$ ns. For a column with $r_p = 400\ \mu$ and $n_p = 10^{26}\ m^{-3}$, Eq. (2.36) gives $\tau_{OH} \simeq 7.2\ \mu s$, so these experimentally achievable parameters[13] are easily matched to a Hammel curve with a feasible current rise rate. The dependence of τ_{OH} on r through Eq. (2.36) illustrates one motivation for creating small channels. The design and operation of ultra-fast current generators is a difficult task, and the required current rise rate from quasi-equilibrium considerations is reduced for smaller channels. It is important to emphasize that these Hammel curves act as a guide in the design of current generators but do not predict plasma properties; the model used to derive these curves assumes a constant radius and density, Bennett equilibrium plasma.

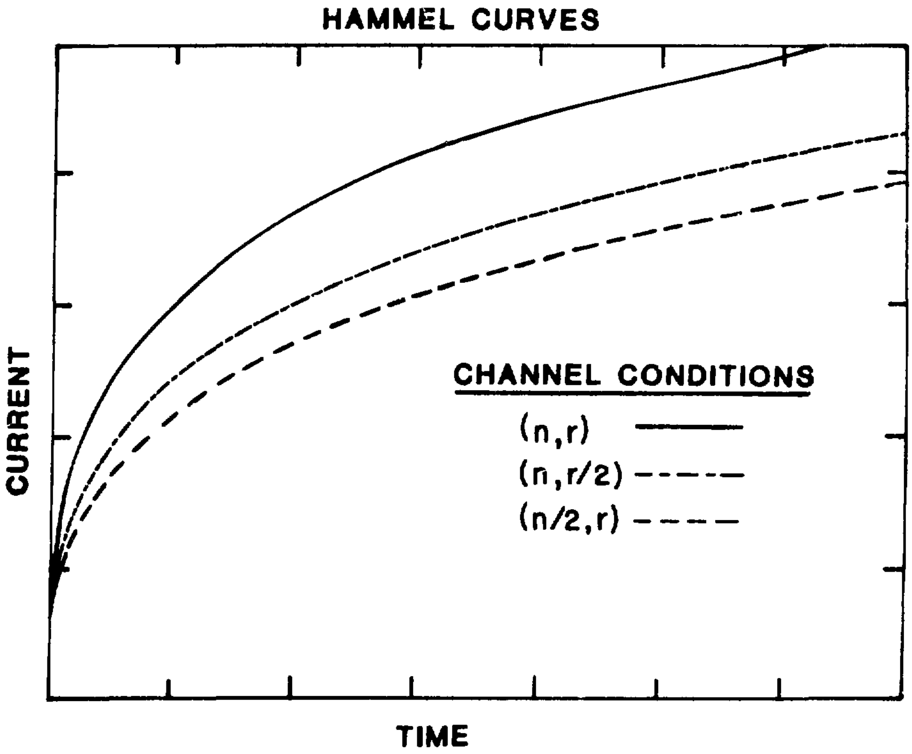

Fig. 2.2 Hammel equilibrium curves for various channel conditions

2.2 Adiabatic Model

The behavior of a plasma in an experiment whose current waveform differs from a Hammel curve cannot be determined from the quasi-equilibrium model. Furthermore, all experimentally generated currents will deviate from the Hammel curves at least at early times, because the solution of Eq. (2.32) requires an unattainable infinite slope at time zero. These difficulties motivate the introduction of the work term in the energy equation, allowing the plasma to expand or contract as it adjusts to the changes in internal energy, ohmic heating, and bremsstrahlung. It is instructive to begin looking at a simple global energy equation from an heuristic viewpoint. For a plasma load with both inductance (L) and resistance (R), the voltage across the load is given by

$$V = \frac{d}{dt}(LI) + IR \quad . \tag{2.37}$$

The total power into the system (load + field) is

$$P_{TOT} = IV = IL\dot{I} + I^2\dot{L} + I^2R \quad . \tag{2.38}$$

The power going into the creation of magnetic field, P_m, is

$$P_m = \frac{d}{dt}\left(\frac{1}{2}LI^2\right) = IL\dot{I} + \frac{1}{2}I^2\dot{L} \quad . \tag{2.39}$$

Thus the power into the plasma load, P_p, is

$$P_p = P_{TOT} - P_m = I^2R + \frac{I^2\dot{L}}{2} \quad . \tag{2.40}$$

We can identify I^2R as ohmic heating input, while $I^2\dot{L}/2$ is the power input to the plasma associated with contraction or expansion work. Using pressure balance,

$$P_B = \frac{B^2}{2\,\mu_o} = \left(\frac{\mu_o I}{2\pi r}\right)^2 \frac{1}{2\,\mu_o} = \frac{\mu_o I^2}{8\pi^2 r^2} \tag{2.41}$$

where P_B is the magnetic field pressure at the surface of the plasma. The work done on the plasma by a small change in volume, $P_B dV$, per unit time is

$$P_B \frac{dV}{dt} = \frac{\mu_o I^2 \ell}{4\pi r} \frac{dr}{dt} \tag{2.42}$$

where ℓ is the column length. For a cylindrical conductor with return current flowing at radius r_{out}, we have

$$L = \frac{\mu_o \ell}{2\pi} \ln \frac{r_{out}}{r} \quad . \tag{2.43}$$

Hence

$$\dot{L} = - \frac{\mu_o \ell}{2\pi r} \frac{dr}{dt} \quad . \tag{2.44}$$

We therefore identify $I^2\dot{L}/2$ as

$$\frac{I^2\dot{L}}{2} = - \frac{\mu_o \ell I^2}{4\pi r} \frac{dr}{dt} = - P_B \frac{dV}{dt} \quad . \tag{2.45}$$

We now express power balance for the entire pinch column as

$$\frac{dW_{Ohmic}}{dt} + \frac{dW_{PdV}}{dt} = \frac{dW_{Brem}}{dt} + \frac{dW_{Internal\ Energy}}{dt} \tag{2.46}$$

where W is the energy of the plasma column. Using expressions for each quantity from (2.31) and (2.42), we obtain the following energy equation,

$$\frac{I^2\ell}{\pi r_p^2}\frac{10^{-4}\ell n\Lambda}{T^{3/2}} - \frac{\mu_o\ell}{4\pi r_p} I^2 \frac{dr_p}{dt} = 1.7\times10^{-38}\frac{N^2T^{1/2}}{\pi r_p^2}\ell + 3\ N\ell k\frac{dT}{dt}\ . \tag{2.47}$$

Ohmic Contraction PdV Bremsstrahlung Internal energy

Now we additionally require Bennett equilibrium to replace T by I^2 where necessary, and we set $\ell n\Lambda = 7$, yielding

$$3.6\times10^{-21}\frac{\ell N^{3/2}}{Ir_p^2} - \frac{10^{-7}\ell}{r_p} I^2 \frac{dr_p}{dt} =$$

$$2.1\times10^{-33}\frac{N^{3/2}}{r_p^2} I\ell + 1.5\times10^{-7} I\ell\frac{dI}{dt} \tag{2.48}$$

Rearranging terms gives

$$\frac{dr_p}{dt} + 1.5\frac{r_p}{I}\frac{dI}{dt} - \left(\frac{3.6\times10^{-14}}{I^2} - 2.1\times10^{-26}\right)\frac{N^{3/2}}{I}\frac{1}{r_p} = 0\ . \tag{2.49}$$

We have recovered the Hammel result with the addition of a work term; for $dr_p/dt = 0$ we obtain the Hammel prescription for I(t). Expressing the constant radius Hammel current as $I_H(t)$, Eq. (2.49) becomes

$$\frac{dr_p}{dt} = 1.5\ r_p\left[\frac{1}{I_H(t)}\frac{dI_H(t)}{dt} - \frac{1}{I(t)}\frac{dI(t)}{dt}\right]\ . \tag{2.50}$$

A column which begins to deviate from the quasi-equilibrium current curve will expand or contract to satisfy energy balance and pressure balance simultaneously. For example, a column will begin to expand at point t_o of Fig. 2.3(a) because

$$\frac{dI}{dt} < \frac{dI_H}{dt} ,$$

and the plasma rids itself of excess ohmic heating energy by doing work against the magnetic field. Alternatively, at point t_o of Fig. 2.3(b) the plasma will contract. Recall that for a constant line density (one assumption of this model), the time scale for the Hammel curve is given by Eq. (2.36), which can be re-expressed as

$$\tau_{OH} \approx 1.6\times10^{31} \frac{r_p^2}{N^{3/2}} . \tag{2.51}$$

Thus for fixed line density, τ_{OH} is proportional to r_p^2. A column which expands because of a generated current waveform, I(t), rising slower than the equilibrium curve, $I_H(t)$, will begin to approach a new equilibrium curve as its radius increases, and the expansion velocity will be reduced. We may estimate the expansion velocity for a plasma at point t_o of Fig. 2.3(a). For $r_p = 300\ \mu$, $n_p = 6\times10^{25}\ m^{-3}$, and I = 100 kA, with dI/dt = 0, Eq. (2.49) results in

$$\frac{dr_p}{dt} = 8.3\times10^3 \text{ m/s}$$

as the instantaneous expansion velocity. As the plasma expands, however, the velocity will decrease in accordance with Eq. (2.49). From this example, we also note the relative unimportance of bremsstrahlung as a mechanism for heat loss compared to expansion, for currents below 400 kA. The model used to derive Eq. (2.49), while requiring the assumption of Bennett equilibrium, can provide some information on plasma column behavior in a given experimental situation. Equation (2.49) can be solved self-consistently with Kirchhoff's laws for the

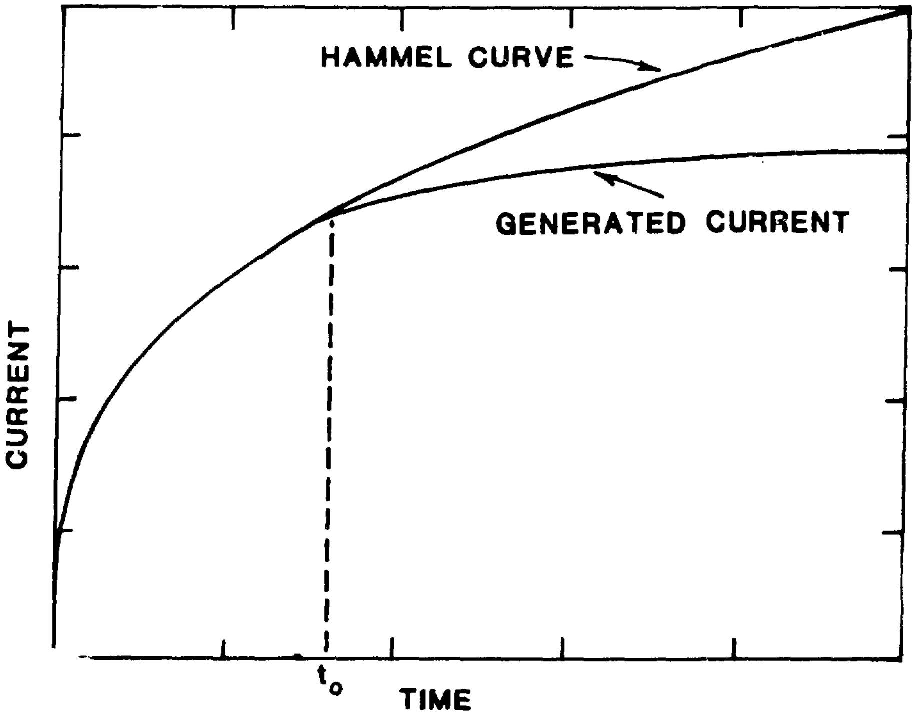

Fig. 2.3(a) Current waveform leading to channel expansion

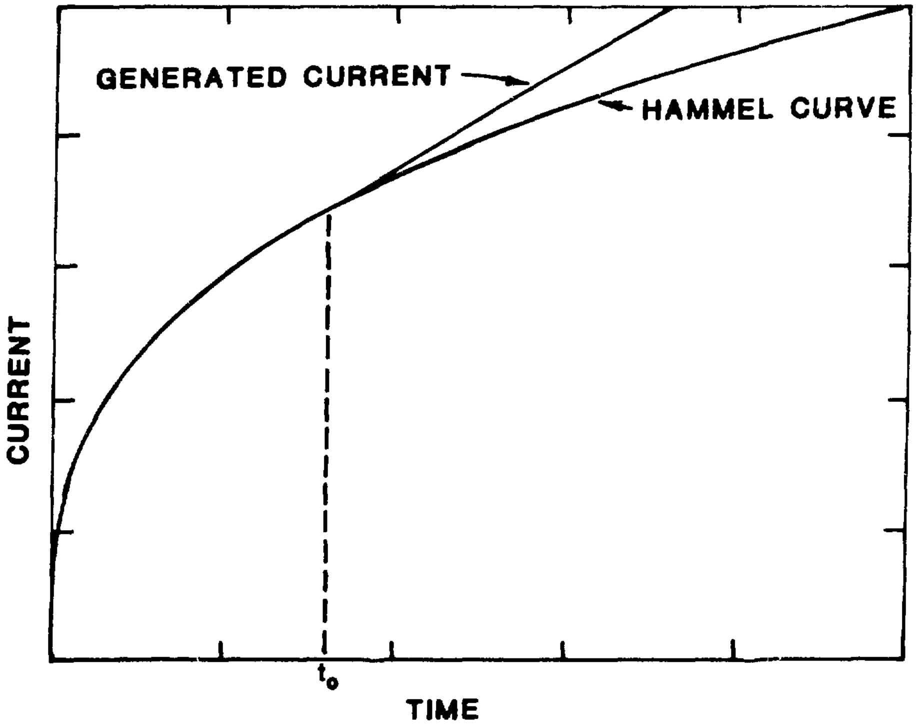

Fig. 2.3(b) Current waveform leading to channel contraction

driving circuit in a relatively simple computer code which treats I, the plasma current, and r_p, the column radius, as the proper variables. The temperature is obtained from the current through the Bennett relation, while the assumption of constant line density, N, gives the plasma density through the plasma radius. This model was first developed by Hagenson et al.,[10] and used an accurate representation of the prototype HDZP current generator and transmission line. The adiabatic model suffers from an inconsistency between the observed outward channel acceleration in the code results and the assumption of Bennett equilibrium, which requires no acceleration. This flaw is a strong motivation for a more complete model which includes the inertial term of Eq. (2.8).

2.3 Constant Line Density (Global MHD) Model

Plasma inertia allows for deviations from pressure balance (Bennett equilibrium) and is required for a self-consistent description of the temporal evolution of the channel. Incorporation of the inertial term into a global momentum equation was accomplished following a suggestion by Oliphant[11] through the use of a similarity solution, i.e., an assumed radial profile for plasma density is allowed to expand or contract but is required to retain its shape at all times. The result of this assumption is a constant line density model for the plasma column which solves the energy, momentum, and circuit equations simultaneously for the three variables I, T, and r_p. The assumption of a constant shape density profile results in constraints on the radial fluid velocity profile through the continuity equation. The density will have a functional form

$$n(r,t) = g(t)\, f\left(\frac{r}{a(t)}\right) \qquad (2.52)$$

where a(t) is the time varying scale size of the channel. Conservation of particles for this constant line density model requires

$$\int_0^\infty 2\pi r n(r,t) dr = \int_0^\infty 2\pi r n(r,o) dr \quad . \qquad (2.53)$$

Thus

$$g(t) = g(o)\,\frac{a^2(o)}{a^2(t)} \tag{2.54}$$

or

$$n(r,t) = g(o)\,\frac{a^2(o)}{a^2(t)}\,f\left(\frac{r}{a(t)}\right) \quad . \tag{2.55}$$

The continuity equation for the cylindrically symmetric column is expressed as

$$\frac{\partial n}{\partial t} + \frac{1}{r}\frac{\partial}{\partial r}(rnv) = 0 \quad , \tag{2.56}$$

or in integral form for a point $R < a$,

$$\int_o^R \frac{\partial n}{\partial t}\, rdr = -\, n(R,t)v(R,t)R \quad . \tag{2.57}$$

Substituting the density profile, (2.55), into (2.57) and integrating by parts yields

$$v(R,t) = \frac{R}{a(t)}\frac{d}{dt}a(t) \quad . \tag{2.58}$$

A similarity solution must therefore require a velocity profile which has a linear spatial dependence. Physically, for a density profile to retain its shape at all times, a given fluid element must keep the same fractional position in the fluid as the column expands or contracts, i.e.,

$$S \equiv \frac{r(t)}{a(t)} \quad \text{is independent of } t \tag{2.59}$$

where a(t) is the radius of a marker cell and r(t) is the location of a fluid element. The marker cell can be the boundary cell, as in a parabolic density profile

$$n(r,t) \propto 1 - \frac{r^2}{a^2(t)}$$

or it can be a scale length cell, as in a Gaussian density profile

$$n(r,t) \propto e^{-r^2/a^2(t)} \quad .$$

To demonstrate the equivalence of (2.58) and (2.59), we examine the convective derivative Dr/Dt following a given fluid cell;

$$\frac{Dr}{Dt} \equiv v = S\,\frac{Da}{Dt} = \frac{r}{a(t)}\,\frac{da(t)}{dt} \tag{2.60}$$

as in (2.58). To express the inertial term, we need

$$\frac{Dv}{Dt} = \frac{D}{Dt}\left[S\,\frac{da(t)}{dt}\right] = S\,\frac{d^2a(t)}{dt^2} \tag{2.61}$$

which we can also derive by

$$\frac{Dv}{Dt} = \frac{D}{Dt}\left[\frac{r}{a(t)}\,\frac{da(t)}{dt}\right] = \frac{r}{a}\,\frac{d^2a}{dt^2} + \frac{1}{a}\,\frac{da}{dt}\left(v - \frac{r}{a}\,\frac{da}{dt}\right) \quad . \tag{2.62}$$

This is the same result as (2.61) using (2.58). All of the analysis to this point has been applicable to any radial density profile. To choose a specific profile best suited to our model, we examine the momentum equation, (2.8), without viscous effects;

$$mn \frac{Dv}{Dt} = - jB - \frac{\partial p}{\partial r} \quad . \tag{2.63}$$

We use Eq. (2.61) to write

$$mn \frac{r}{a} \frac{d^2a}{dt^2} = - jB - \frac{\partial p}{\partial r} \quad . \tag{2.64}$$

To obtain a constraint on n(r,t), we temporarily drop the magnetic pressure term, and using the equation of state, we find

$$mn \frac{r}{a} \frac{d^2a}{dt^2} = - 2kT \frac{\partial n}{\partial r} \tag{2.65}$$

for an isothermal column. Solution of (2.65) yields a Gaussian profile for the density,

$$n(r,t) = n_o \frac{a_o^2}{a^2(t)} e^{-r^2/a^2(t)} \quad , \tag{2.66}$$

which is therefore our choice for the shape of the density. With a Gaussian density profile, self-consistency is achieved by allowing each fluid element to move in accordance with the momentum equation and still retain the same relative position with respect to neighboring cells. We next consider the equilibrium equation, (2.9), to provide a constraint on the magnetic field profile, given a Gaussian density profile.

$$-\underset{\sim}{j}\times\underset{\sim}{B} = - \underset{\sim}{\nabla}p = - 2kT \frac{\partial n}{\partial r} \hat{e}_r = \frac{4kT}{a^2} rn \hat{e}_r \tag{2.67}$$

so we have

$$\underset{\sim}{j}\times\underset{\sim}{B} = - jB\ \hat{e}_r = - \frac{1}{\mu_o r^2}\frac{\partial}{\partial r}\left[\frac{r^2B^2}{2}\right]\hat{e}_r = - \frac{4kTrn}{a^2}\hat{e}_r \quad . \tag{2.68}$$

The solution of this equation is

$$B^2(r,t) = \frac{K^2}{r^2}\left(1 - e^{-r^2/a^2}\right) - \frac{K^2}{a^2}e^{-r^2/a^2} \tag{2.69}$$

with

$$K = \frac{\mu_o I}{2\pi} \quad . \tag{2.70}$$

This field profile will provide $\underset{\sim}{j}\times\underset{\sim}{B}$ forces of the proper magnitude to retain the Gaussian density profile. We can now combine (2.65) and (2.67) to obtain a momentum equation which incorporates inertial effects and is consistent with a similarity solution.

$$mn\frac{Dv}{Dt} = - \frac{1}{\mu_o r^2}\frac{\partial}{\partial r}\left[\frac{r^2B^2}{2}\right] - 2kT\frac{\partial n}{\partial r} \tag{2.71}$$

or

$$\frac{n_o a_o^2}{a^2}\frac{mr}{a}e^{-r^2/a^2}\ddot{a} = - \frac{1}{\mu_o a^4}K^2\ re^{-r^2/a^2} + 4\ n_o a_o^2\frac{kTr}{a^4}e^{-r^2/a^2} \tag{2.72}$$

so that

$$\ddot{a} = \frac{1}{4\pi mNa}\left(-\mu_o I^2 + 16\pi NkT\right) \tag{2.73}$$

where

$$N = 2\pi\int_o^\infty n(r,t)rdr = \pi n_o a_o^2 \quad . \tag{2.74}$$

It is clear that our self-consistent momentum equation, (2.73), reduces to the Bennett equation, (2.19), when the inertial term is dropped.

We now examine the LHS of the energy equation, (2.21).

$$\frac{D}{Dt}\frac{3}{2}p + \frac{5}{2}p\nabla\cdot\underset{\sim}{v} = \frac{3}{2}\left(2kT\frac{Dn}{Dt}\right) + \frac{3}{2}\,2\,kn\frac{dT}{dt} + \frac{5}{2}p\nabla\cdot\underset{\sim}{v} \quad . \tag{2.75}$$

Continuity gives

$$\frac{3}{2}\,2kT\frac{Dn}{Dt} = -\frac{3}{2}\,2\,kTn(\nabla\cdot\underset{\sim}{v}) \tag{2.76}$$

and the linear velocity profile, (2.58), provides

$$\nabla\cdot\underset{\sim}{v} = \frac{1}{r}\frac{\partial}{\partial r}(rv) = \frac{1}{r}\frac{\partial}{\partial r}\left(\frac{r^2}{a}\frac{da}{dt}\right) = \frac{2}{a}\frac{da}{dt} \tag{2.77}$$

so

$$\frac{D}{Dt}\frac{3}{2}p + \frac{5}{2}p(\nabla\cdot\underset{\sim}{v}) = 3nk\frac{dT}{dt} + \frac{4nkT}{a}\frac{da}{dt} \tag{2.78}$$

or the energy equation is

$$3nk \frac{dT}{dt} + \frac{4nkT}{a} \frac{da}{dt} = \eta j^2 - \text{bremsstrahlung} + \text{visc. heating} - \nabla \cdot \underset{\sim}{q} \ . \qquad (2.79)$$

The limitations of a self-similar solution of the equations are now evident; the consistent 1-D MHD energy equation will begin to alter any initial density profile. For example, the ohmic heating term, ηj^2, will have a profile dictated by the magnetic field distribution of Eq. (2.69) which is inconsistent with that required by Eq. (2.79). In addition, a third equation, governed by the driving circuit and based on Maxwell's equations, is required to close the system to solve for I, T, and r_p. This equation will reflect the diffusion of field into the column, again altering the field profile of Eq. (2.69). It is in the spirit of this model to retain the Gaussian density profile in spite of inconsistencies with the energy and circuit equations; the only alternative is to abandon the global model and return to a 1-D MHD code which can accommodate time-varying profiles. The effect of field profile alteration in the circuit equation is particularly minimal, as evidenced by the small change in inductance for two extreme current distributions. With an outer return conductor radius of 0.2 m and a plasma current-carrying column of 100 μ radius, the bulk of the magnetic field lies outside the column, and therefore the inductance is relatively insensitive to changes within the plasma. For a uniform current density profile, with length 0.05 m and the parameters above,

$$L = \frac{\mu_o \ell}{2\pi} \left(\ell n \ r_{outer}/r_{plasma} + \frac{1}{2} \right) = 81 \text{ nH} \quad ,$$

while for a plasma with a skin current at r_{plasma},

$$L = \frac{\mu_o \ell}{2\pi} \left(\ell n \ r_{outer}/r_{plasma} \right) = 76 \text{ nH}$$

where L is defined through

$$L = \frac{1}{I} \iint dzdr\ B_\theta(r,z) \quad . \tag{2.80}$$

We express the plasma resistance R as

$$R = \frac{1}{I} \int_{z=0}^{z=\ell} (\eta j)_{r=o}\ dz \tag{2.81}$$

which reduces to

$$R = \frac{\ell}{I}(\eta j)_{r=o} \tag{2.82}$$

for axially symmetric plasmas, and the circuit equation for the plasma becomes

$$V_{\text{applied}} = L\dot{I} + I\dot{L} + IR \tag{2.83}$$

with the geometry of Fig. 2.4. For a complicated driving circuit involving a Marx bank, water transmission lines, and a self-breaking water switch, all described in detail in Chapter 3, V_{applied} must be solved self-consistently with Kirchhoff's laws for the driver. In the global MHD code, the Marx bank is represented by Fig. 2.5a with experimentally determined parameters, while the water transmission line is modeled using discrete elements (Fig. 2.5b). The self-breaking water switch is incorporated into the driving circuit code using the empirical relations[14] shown in Fig. 2.5c. Combining Eqs. (2.73), (2.79), and (2.83) with a model for the current generator (Fig. 2.6) provides a scheme to solve simultaneously for the time dependence of the three plasma column variables I, T, and r_p. The plasma density is assumed to have the Gaussian spatial dependence of Eq. (2.66), the temperature is assumed to be uniform across the column, and for simplicity, the current density is also assumed uniform in the energy and circuit equations. The global model momentum equation additionally includes a term reflecting the drag produced by the surrounding neutral gas, and a pseudo-viscous damping force to limit the effects of gross plasma column oscillations. These oscillations are analogous to those observed

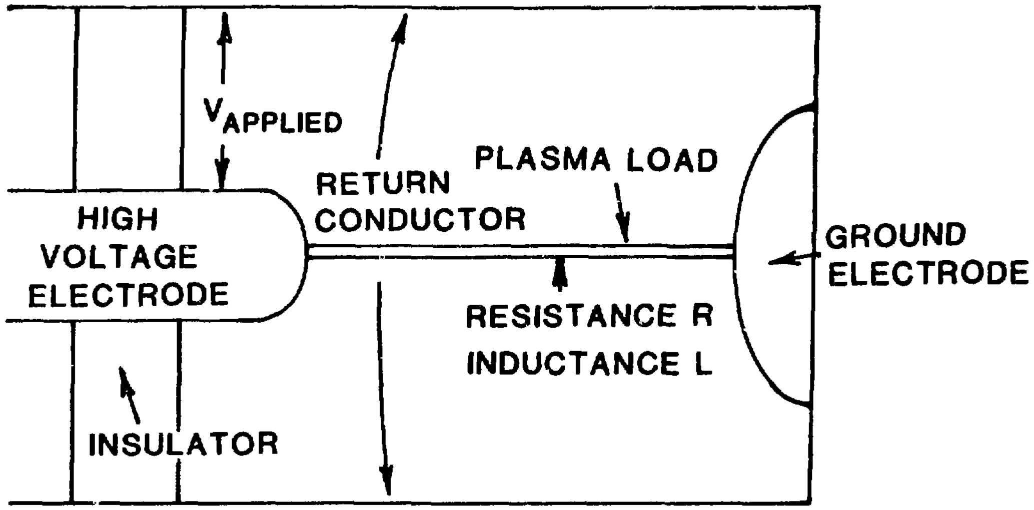

Fig. 2.4 Schematic diagram of plasma load

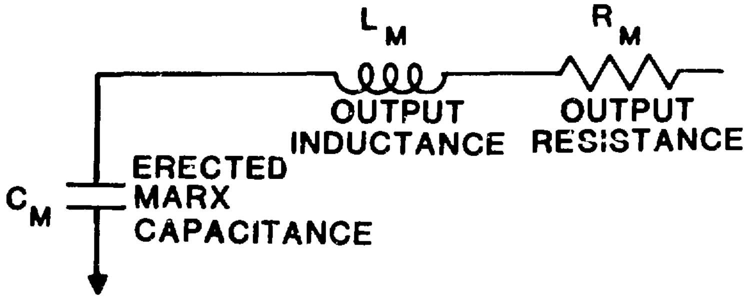

Fig. 2.5(a) Marx bank schematic for computational model

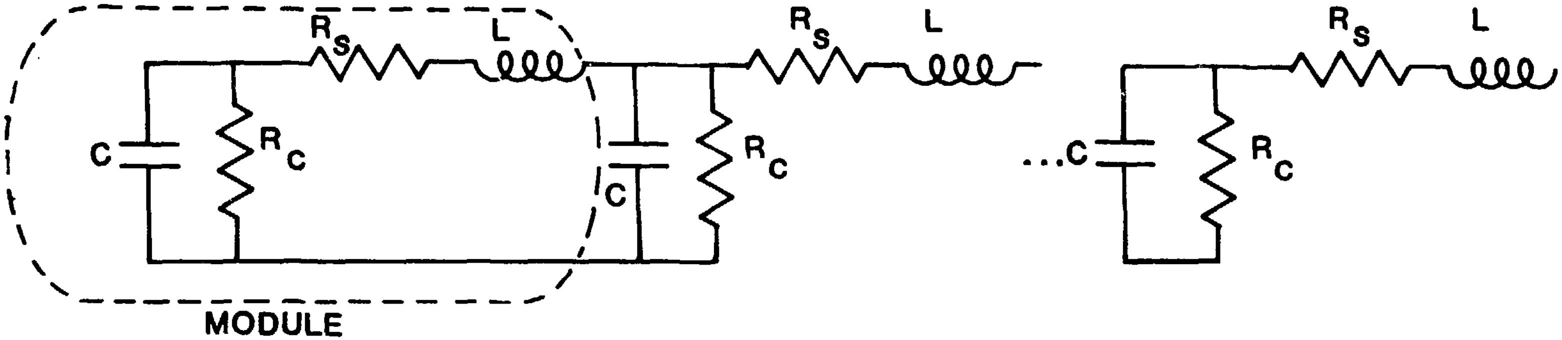

Fig. 2.5(b) Water transmission line schematic for computational model

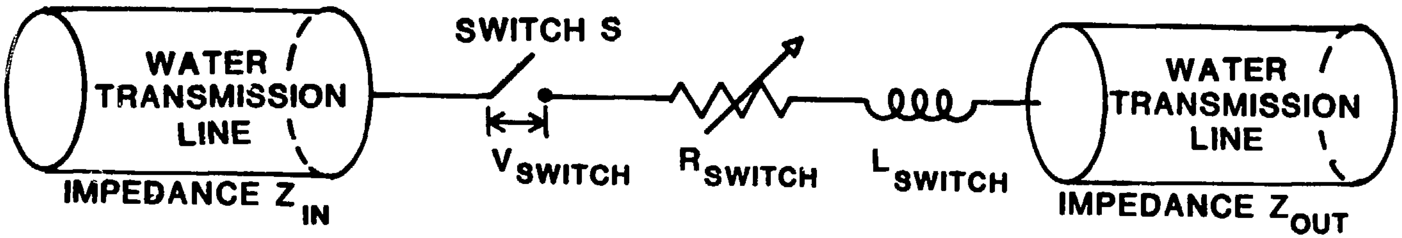

Switch S closes when $V_{switch} = V_{break}$ at time t_o

$$R_{switch}(t) = \infty \qquad t < t_o$$

$$R_{switch}(t) = (Z_{IN} + Z_{OUT}) \left[\frac{e^{-(t-t_o)/\tau_R}}{1 - e^{-(t-t_o)/\tau_R}} \right] \qquad t > t_o$$

$$\text{with } \tau_R = \frac{5}{\left[N(Z_{IN} + Z_{OUT})\right]^{1/3} \; E^{4/3}} \quad \text{ns}$$

E = breakdown field (MV/cm) ~ 0.3

N = number of channels

$$L_{switch} \approx \frac{10 \text{ nH}}{N}$$

Fig. 2.5(c) Water switch empirical model

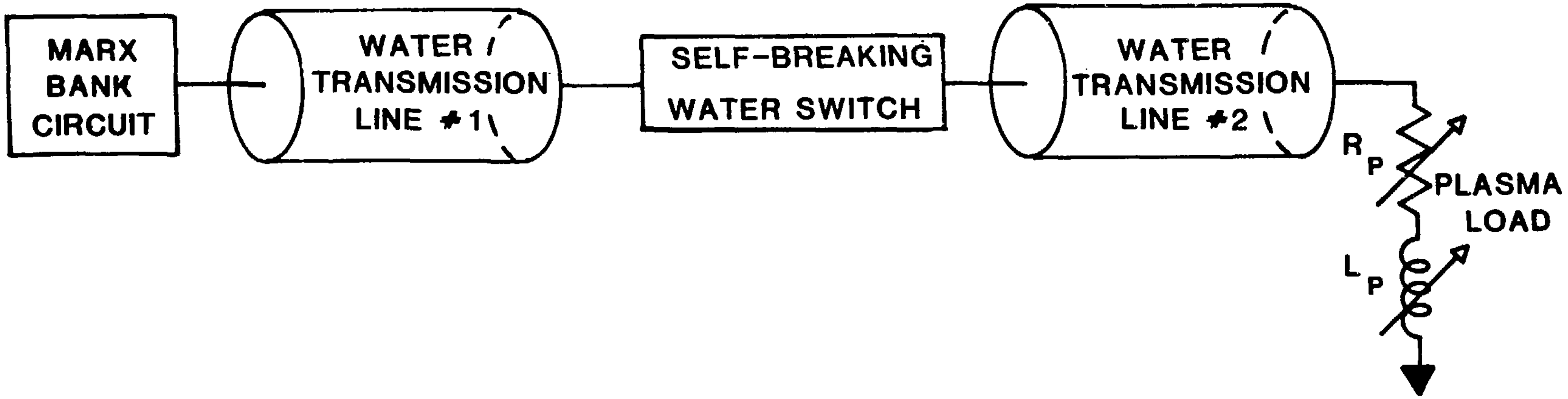

Fig. 2.6 Circuit schematic of HDZP experiment for global MHD calculations

experimentally in classical Z-pinches[15] and are attributable to the inclusion in (2.73) of the inertial term, resulting in a harmonic momentum equation.

A simple calculation easily illustrates the oscillation effect. We first consider an axial field stabilized shell pinch with no internal plasma pressure and a constant skin current associated with a highly conducting boundary. The equation of motion for this plasma is

$$\rho_s \ddot{\chi} = \frac{B_z^2(r)}{2\,\mu_o} - \frac{B_\theta^2(r)}{2\,\mu_o} \tag{2.84}$$

where ρ_s is the areal mass density of the plasma shell and $\chi \equiv (r-r_o)$ is the displacement of the shell from its equilibrium position r_o. The assumption of a perfectly conducting shell leads to a constant flux requirement,

$$B_z(r)\pi r^2 = B_z(r_o)\pi r_o^2 \rightarrow B_z(r) = B_z(r_o)\,\frac{r_o^2}{r^2} \quad , \tag{2.85}$$

while the assumption of constant current provides the constraint

$$B_\theta(r) = B_\theta(r_o)\,\frac{r_o}{r} \quad . \tag{2.86}$$

From the equilibrium, setting the inertial term equal to zero in (2.84), we have

$$B_\theta(r_o) = B_z(r_o) \quad . \tag{2.87}$$

Substituting Eqs. (2.85), (2.86), and (2.87) into (2.84) and expanding about the equilibrium point, r_o, we get

$$\rho_s \ddot{\chi} = \frac{-B_z^2(r_o)\chi}{\mu_o r_o} \quad , \tag{2.88}$$

which results in an oscillation frequency for the column radius of

$$\omega_{osc}^2 = \frac{B_z^2(r_o)}{\mu_o r_o \rho_s} \quad . \tag{2.89}$$

We recognize the similarity between (2.89) and the characteristic Alfvén frequency found for hydromagnetic waves. In the plasma model developed in this chapter, the plasma internal pressure is expected to replace the axial field pressure of the preceding analysis, and one obtains analogous oscillations in the global MHD code. Here, the oscillations are a bulk plasma column effect, and we estimate the frequency as

$$\omega_{osc}^2 \simeq v_A^2 \left(\frac{2\pi}{r_p}\right)^2 \tag{2.90}$$

where v_A is the Alfvén velocity. For a current of 100 kA, a number density $n_p = 1\times10^{26}$ m^{-3}, and $r_p = 200$ μ, we find in a hydrogenic ($M \simeq m_p$) plasma

$$v_A^2 = \frac{B^2}{\mu_o nM} = \left(\frac{\mu_o I}{2\pi r_p}\right)^2 \frac{1}{\mu_o nM} = 4.8\times10^{10} \text{ m}^2/\text{s}^2 \tag{2.91}$$

and

$$\omega_{osc} = 6.9\times10^9 \text{ s}^{-1} \text{ or } \tau_{osc} \simeq 0.9 \text{ ns} \quad . \tag{2.92}$$

These oscillations are evident in the numerical solution of the global MHD model, and it is expected that physical processes such as viscous damping will reduce this effect in the experiment. We therefore introduce a pseudo-viscous damping force in the momentum equation, (2.73), to limit these bulk oscillations. The typical viscous damping force used is proportional to the plasma column radial velocity and the ion viscosity transport coefficient,

$$\eta_o^i = 0.96 \; n \; T_i \; \tau_i \quad ,$$

where τ_i is the ion collision time. In addition, a term is added to the energy equation, (2.79), to represent the viscous heating associated with the dissipative effects of the damping force; this term is proportional to η_o and the square of the channel velocity, and it is positive definite.

A classical expression for thermal conductivity is included in Eq. (2.79) as an energy loss mechanism, H_{COND}, with

$$H_{COND} = 2\pi K_{COND} \frac{kT}{r_p} \quad \frac{J}{m^2 s} \tag{2.93}$$

where kT/r_p is an approximation to the thermal gradient and K_{COND} is the classical thermal conductivity. As the plasma current rises initially, the plasma undergoes a series of transitions through various regimes of conductivity. We use the following expressions for electron and ion strong and weak field conductivity limits:

$$\begin{aligned} K_{\parallel}^e &= \frac{3.2 \quad nkT}{m_e} \tau_e & K_{\parallel}^i &= 3.9 \, \frac{nkT}{m_i} \tau_i \\ & & & \qquad\qquad m^{-1}s^{-1} \\ K_{\perp}^e &= \frac{4.7 \quad nkT}{m_e \omega_{ce}^2 \tau_e} & K_{\perp}^i &= 2 \, \frac{nkT}{m_i \omega_{ci}^2 \tau_i} \end{aligned} \tag{2.94}$$

The subscript $\perp$ denotes a strong field limit,

$$\omega\tau >> 1 \quad , \tag{2.95}$$

where ω is the cyclotron frequency for the appropriate species and τ is the collision frequency for the same species,

$$\tau_e = \frac{3.44\times10^{11}T^{3/2}}{n\ell n\Lambda} \qquad \tau_i = \frac{2.09\times10^{13}T^{3/2}}{n\ell n\Lambda} \quad . \tag{2.96}$$

Similarly, the subscript $\parallel$ is the weak field limit with $\omega\tau \ll 1$. Initially, both the electrons and ions are unmagnetized (weak field limit), and we have

$$\frac{K_\parallel^e}{K_\parallel^i} \simeq \left(\frac{m_i}{m_e}\right)^{1/2} \simeq 40 \quad . \tag{2.97}$$

Thus, the early conductivity of the plasma is governed by electron weak field transport. At large currents, where both species are magnetized, we find

$$\frac{K_\perp^i}{K_\perp^e} \simeq \left(\frac{m_i}{m_e}\right)^{1/2} \simeq 40 \quad , \tag{2.98}$$

and the plasma is dominated by cross-field ion thermal conductivity. Using the Bennett equilibrium relation, a plasma radius of 100 μ, plasma density $n = 10^{26}\ m^{-3}$, and the expressions in (2.94), we obtain the following regimes of conductivity.

	Current and Temperature	Magnetization	H_{COND}	Dominant Conductivity
Region 1	$I < 25$ kA $T < 30$ eV	$\omega_e\tau_e < 1$ $\omega_i\tau_i < 1$	$\propto T^{7/2}$	$K_{\parallel}^{e}$
Region 2	25 kA $< I <$ 40 kA 30 eV $< T <$ 80 eV	$\omega_e\tau_e > 1$ $\omega_i\tau_i < 1$	$\propto T^{-1/2}$	$K_{\perp}^{e}$
Region 3	40 kA $< I <$ 60 kA 80 eV $< T <$ 180 eV	$\omega_e\tau_e > 1$ $\omega_i\tau_i < 1$	$\propto T^{7/2}$	$K_{\parallel}^{i}$
Region 4	$I > 60$ kA $T > 180$ eV	$\omega_e\tau_e > 1$ $\omega_i\tau_i > 1$	$\propto T^{-1/2}$	$K_{\perp}^{i}$

The temperature dependence of the quantity H_{COND} in Eq. (2.93) is graphically depicted in Fig. 2.7 and was the original motivation for gas embedded plasma experiments.[16] The thermal conductivity in the global MHD computer code is calculated using Eq. (2.94) for the appropriate region of interest.

The iterative FORTRAN program which solves the MHD momentum and energy equations along with the driving circuit equations reduces the differential equations to nonlinear difference equations, using an Eulerian approximation. For an equation of the form

$$\frac{dT}{dt} = g(r,I,T) \tag{2.99}$$

we use

$$T^{t+\Delta t} = T^{t} + \Delta t g(r^{t},I^{t},T^{t}) \quad . \tag{2.100}$$

Unfortunately, the set of equations we must solve is stiff in the numerical sense,[17] i.e., the solution is composed of components with vastly different time scales. Rapid Alfvén type oscillations, Eq. (2.92), are damped out by the pseudo-viscous force, and the remaining solution has a time constant governed by the water transmission line length, approximately 50 ns. While sophisticated techniques exist for solving stiff systems of equations, we have simply chosen a time step, Δt, sufficiently small to avoid numerical instabilities, and suffered an increase in running time. Nevertheless, a calculation modeling 200 ns of

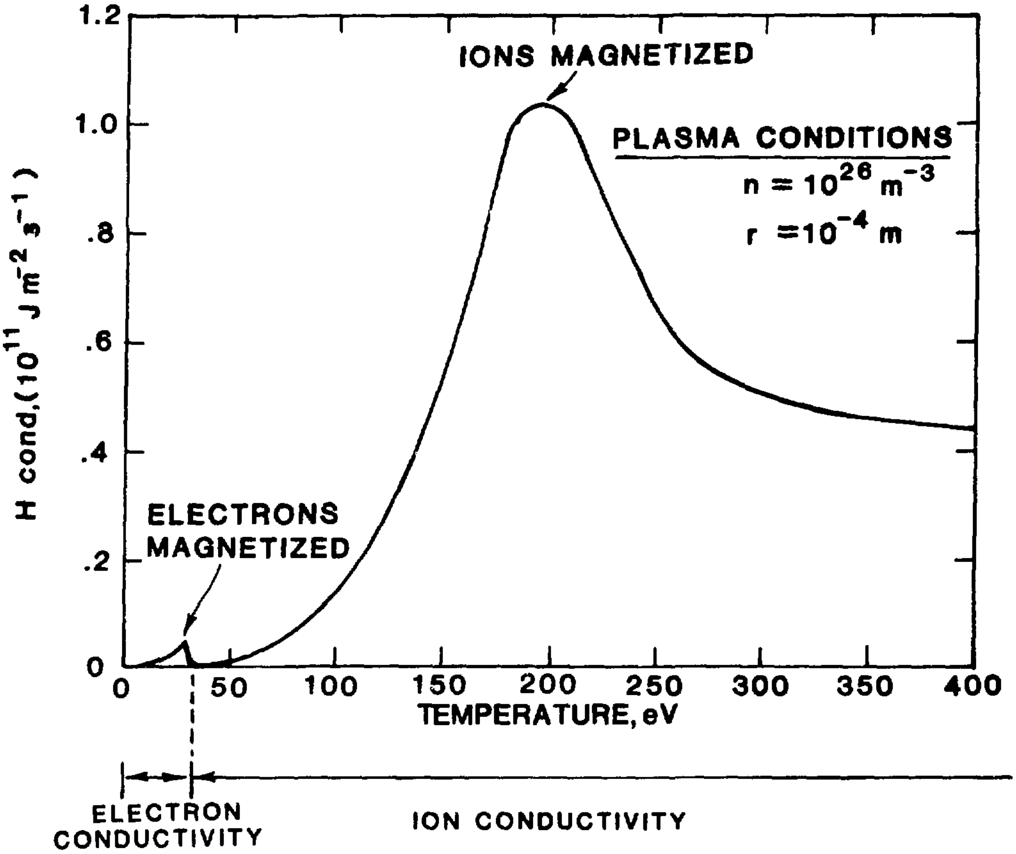

Fig. 2.7 Thermal conductivity energy loss, H_{COND}, used in global MHD calculations

real time for the prototype device can be performed on a DEC PDP-10 computer using only 15 minutes of CPU time.

One limitation of the global MHD model is its treatment of the initial plasma conditions. Neither the breakdown-avalanching process under the applied electric field nor the laser-gas interaction is modeled. Instead, the plasma is simply assumed to be fully ionized within a specified radius and to have an initial temperature of 5 eV. Extensive work by Lindemuth on the 2-D MHD MANIAC code suggests that the breakdown phase of plasma development has a critical effect on the eventual column behavior, and this view is supported by experiment. It is outside the scope of our global MHD model, however, to treat the channel formation physics.

2.4 Model Comparisons for Test Problems

It is instructive to compare the results of our model with those of the adiabatic model developed by Hagenson and the 1-D MHD model (RAVEN) of Oliphant. The test problem circuit is an early configuration of the prototype device which operated without a self-breaking water switch, at relatively low Marx bank voltages of 200 kV. All models use initial conditions of a fully ionized 200 μ radius column with $n_e = n_i = 7\times10^{25}\ m^{-3}$. In Fig. 2.8a, the predicted current waveforms from each of the three models are presented. It is found that the choice of plasma model has little effect on the current waveform, and one obtains reasonably similar predictions for the current from a static plasma model of fixed radius. The column radius is more sensitive to the specific model used; the RAVEN code makes a distinction between the radius of an outgoing shock wave and a radius for the current carrying channel, while the adiabatic[18] and global MHD models compute a solitary plasma dimension. Figure 2.8b shows a comparison of code predictions for radius and the limitations of the adiabatic model at early times. By eliminating the inertial term in the momentum equation, the adiabatic model exhibits an unrealistic initial expansion velocity which exceeds the thermal velocity, while the global and 1-D MHD codes, in reasonable agreement with each other, predict a more gradual expansion. For these experimental conditions, it is thus found that the simple global MHD model yields results similar to those obtained with a more sophisticated and costly computer code.

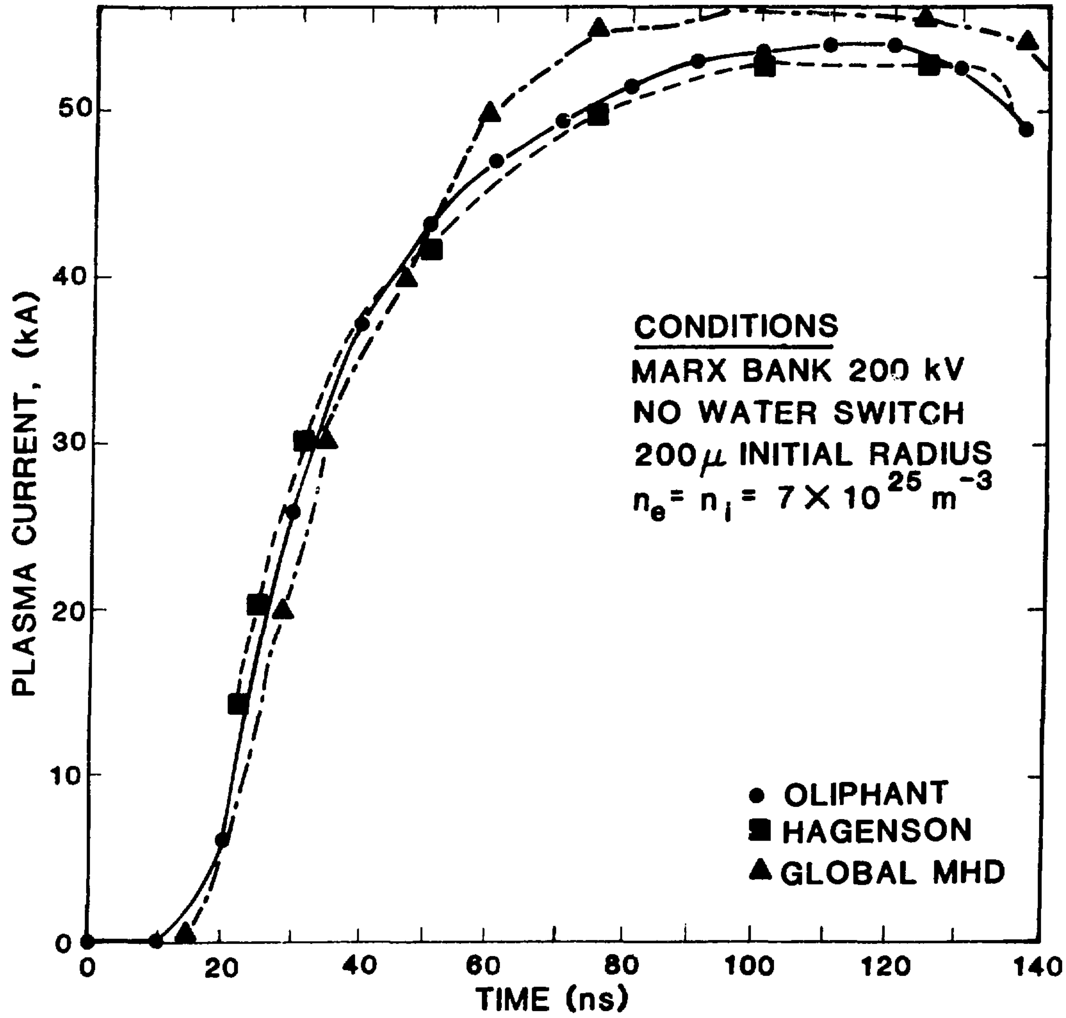

Fig. 2.8(a) Predicted current waveforms for three plasma models (Oliphant results reproduced with permission of T. A. Oliphant) [Hagenson results from R. L. Hagenson et al., Los Alamos Scientific Laboratory report LA-8186-MS, (1980)]

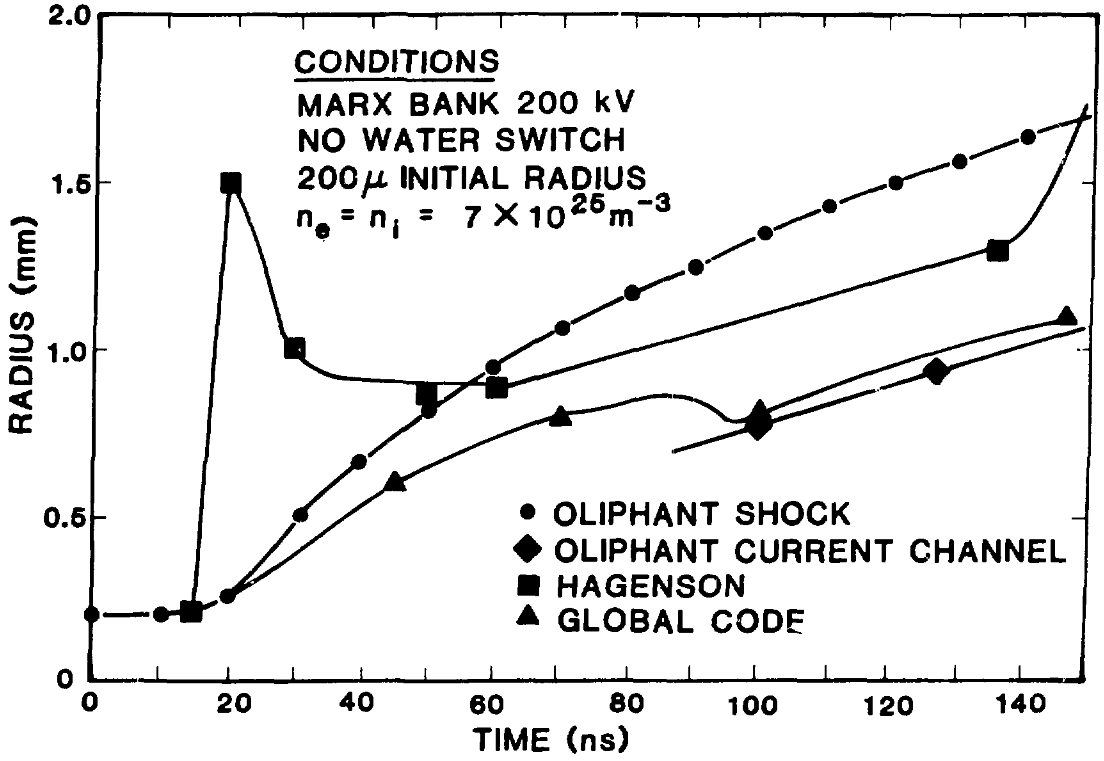

Fig. 2.8(b) Predicted column dynamics for three plasma models (Oliphant results reproduced with permission of T. A. Oliphant) [Hagenson results from R. L. Hagenson et al., Los Alamos Scientific Laboratory report LA-8186-MS, (1980)]

A final comparison, performed for a set of conditions achieved on an experiment similar to the prototype device, displays some of the inadequacies of the global MHD model. For this test, a plasma with an initial radius of 150 μ and a fill density of 3 atmospheres of H_2 ($n_e = n_i = 1.5\times10^{26}$ m^{-3}) is driven by a current which rises linearly to 260 kA in 200 ns (Fig. 2.9a). The 2-D MHD MANIAC code[19] predicts a monotonically increasing radius for the current-carrying channel with an asymptotic value of 1.3 mm (Fig. 2.9b). The global MHD code solution has a radius which increases to 0.8 mm and then decreases to 0.1 mm. Also observed in this solution are the Alfvén type oscillations described in Eq. (2.92). The global MHD model assumes a constant line density, and initially, the rise rate of the current ($\dot{I} = 1.3\times10^{12}$ A/s) is insufficient to match the Hammel curve for these plasma conditions, and the plasma expands. Eventually, however, the expansion increases r_p to a value capable of reducing the requirements of the Hammel equilibrium curve to $\dot{I}_H < 1.3\times10^{12}$ A/s, and the plasma contracts. In the MANIAC model, significant accretion occurs as a result of $m = 0$ sausage instabilities, and the plasma is predicted to have seven times the original line density at $t = 180$ ns. This accounts for the discrepancies between the two codes and displays the constant line density limitation of the global code; nevertheless, the sizable runtime savings using the global MHD code justify its application to a number of experimental problems of interest.

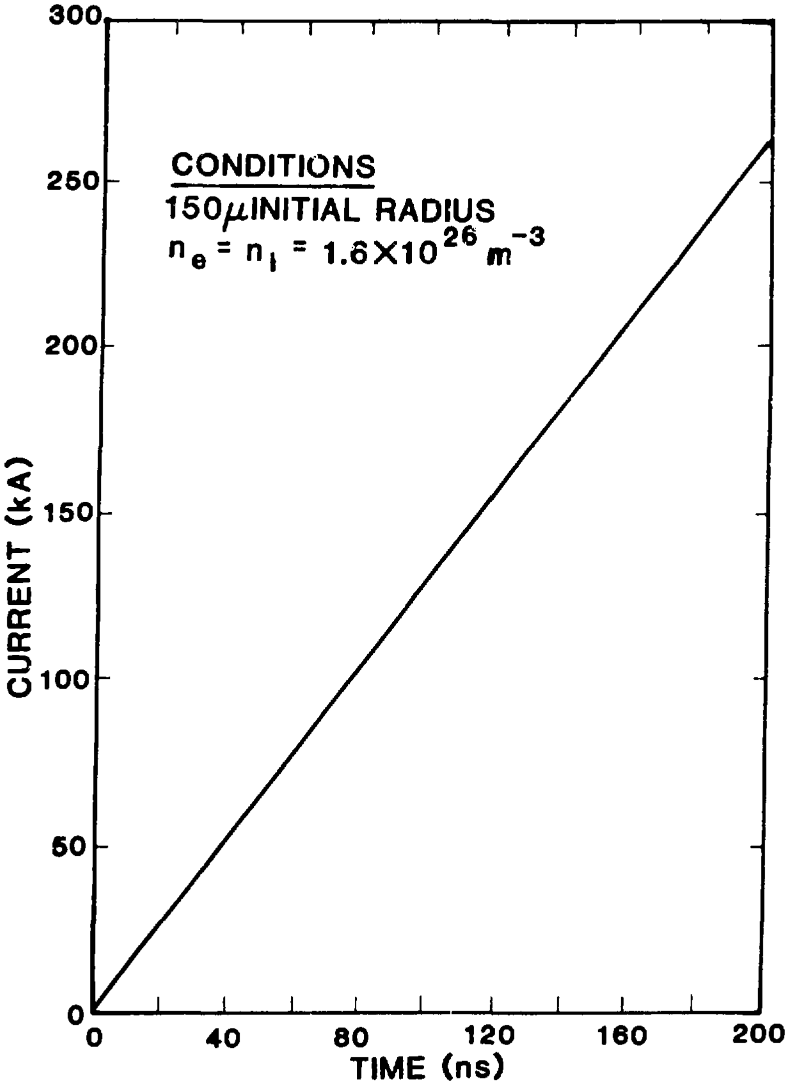

Fig. 2.9(a) Current waveform for code comparison with 2-D MANIAC results

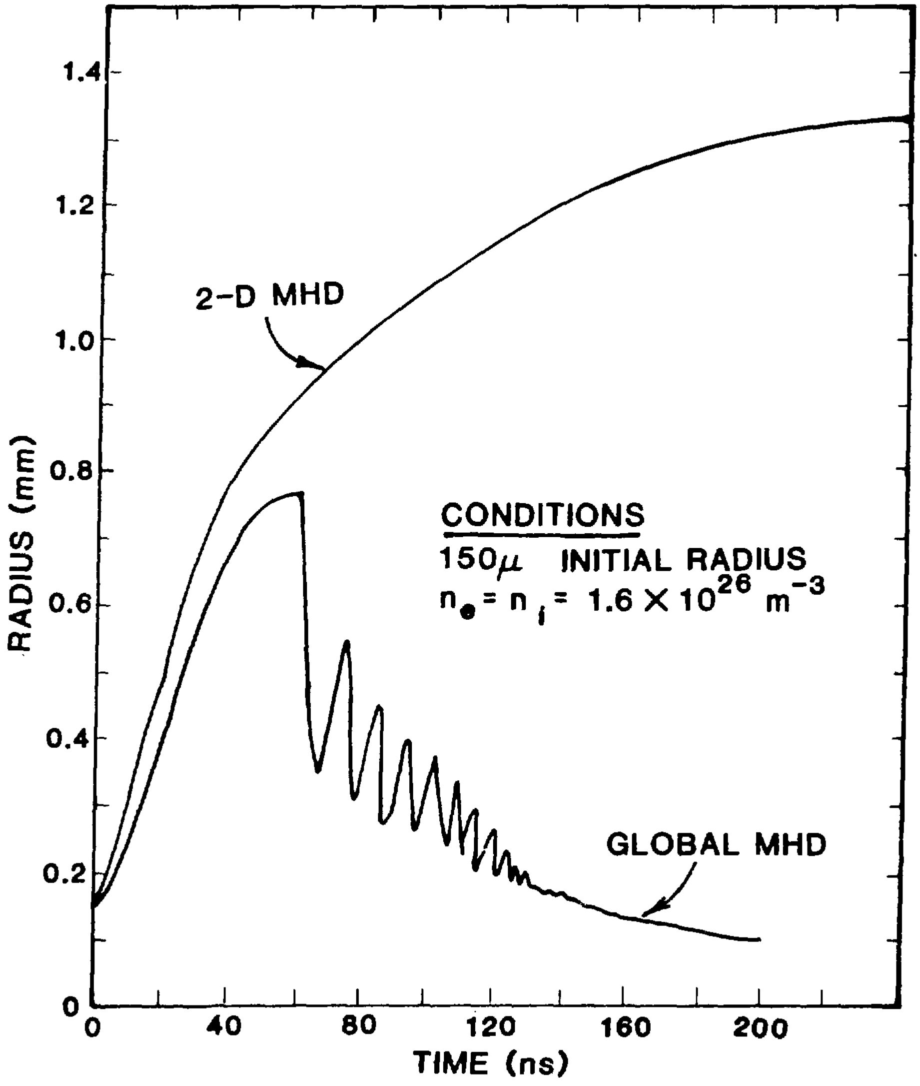

Fig. 2.9(b) Predicted column dynamics for linearly rising current [2-D MHD results from L. A. Jones et al., Appl. Phys. Lett. 38, 522 (1981)]

References for Chapter 2

1. D. Potter, *Computational Physics* (Wiley, London, 1973).
2. T. A. Oliphant, *Raven Physics Manual*, unpublished (1981).
3. I. R. Lindemuth, Lawrence Livermore Laboratory report UCRL-52492, (1979).
4. I. R. Lindemuth and J. H. Brownell, Bull. Am. Phys. Soc. **25**, 1012 (1980).
5. L. A. Jones, K. H. Finken, A. Dangor, E. Källne, S. Singer, I. R. Lindemuth, J. H. Brownell, and T. A. Oliphant, Appl. Phys. Lett. **38**, 522 (1981).
6. I. Lindemuth, J. Brownell, T. Oliphant, and D. Weiss, Los Alamos Scientific Laboratory report LA-UR-81-346, (1981).
7. W. H. Bennett, Phys. Rev. **45**, 890 (1934).
8. R. S. Pease, Proc. Phys. Soc. **70**, 11 (1957).
9. J. E. Hammel, Los Alamos Scientific Laboratory report LA-6203-MS, (1976).
10. R. L. Hagenson, A. S. Tai, R. A. Krakowski, and R. W. Moses, Los Alamos Scientific Laboratory report LA-8186-MS, (1980).
11. T. A. Oliphant, Los Alamos National Laboratory, personal communication, 1981.
12. R. C. Elton, in *Methods of Experimental Physics*, edited by H. R. Griem and R. H. Lovberg (Academic Press, New York, 1970), Vol. 9, part A, 154.
13. J. S. Shlachter and J. E. Hammel, Bull. Am. Phys. Soc. **25**, 923 (1980).
14. J. P. Vandevender, Sandia National Laboratory, personal communication, 1979.
15. L. C. Burkhardt and R. H. Lovberg, Proc. 2nd U.N. Conf. on Peaceful Uses of Atomic Energy, Vol. 32 (United Nations, Geneva, 1958), pp. 29-33.
16. C.-G. Fälthammar, Phys. Fluids **4**, 1145 (1961).
17. C. W. Gear, *Numerical Initial Value Problems in Ordinary Differential Equations* (Prentice-Hall, Inc., Englewood Cliffs, New Jersey, 1971) Chapter 11.
18. Hagenson, et al., loc. cit.
19. L. A. Jones, et al., loc. cit.
20. M. G. Haines, Physical Society of London Proceedings **76**, 250 (1960).

Chapter 3. Prototype HDZP Experiment

Experiments have been performed on the prototype high density Z-pinch (HDZP) machine at Los Alamos National Laboratory for the past three years.[1,2,3] This chapter will provide a detailed description of the apparatus, the two modes of operation of the experiment, and the diagnostic methods which have been employed.

The prototype experiment was designed to provide a peak current of 100 kA with a waveform approximating the Hammel[4] curve for a plasma with 100 μ radius and a fill pressure of 1/2-3 atmospheres of H_2 gas. Figure 3.1 shows the quasi-equilibrium current waveform for a plasma with $r_p = 100\ \mu$ and $n_e = n_i = 4.8\times10^{25}\ m^{-3}$, which requires the current to reach 50 kA in approximately 10 ns or

$$\dot{I} \approx 5\times10^{12}\ A/s \quad . \tag{3.1}$$

This fast current rise necessitates the use of electron-beam pulse power technology and represents a major departure from the capacitor bank-ignitron or capacitor bank-spark gap systems of conventional pulsed magnetic confinement experiments. The major components of the experiment, each of which will be discussed in detail, include a Marx bank generator, a water dielectric coaxial transmission line, a water peaking switch, and a plasma load chamber (Fig. 3.2). In addition, a ruby laser is used to control the breakdown in the load chamber and determine the size and uniformity of the initial plasma channel.

3.1 Marx Bank

To facilitate the generator design, we may treat the plasma load as a fixed inductance, and thus recognize that the current rise rate of Eq. (3.1) leads to a requirement for high voltages across the load. The plasma is approximated as a skin current at 100 μ radius with an outer radius equal to the radius of the load return current in the chamber walls, $r_{out} = 0.2$ m. We use an electrode spacing of $\ell = .05$ m to find

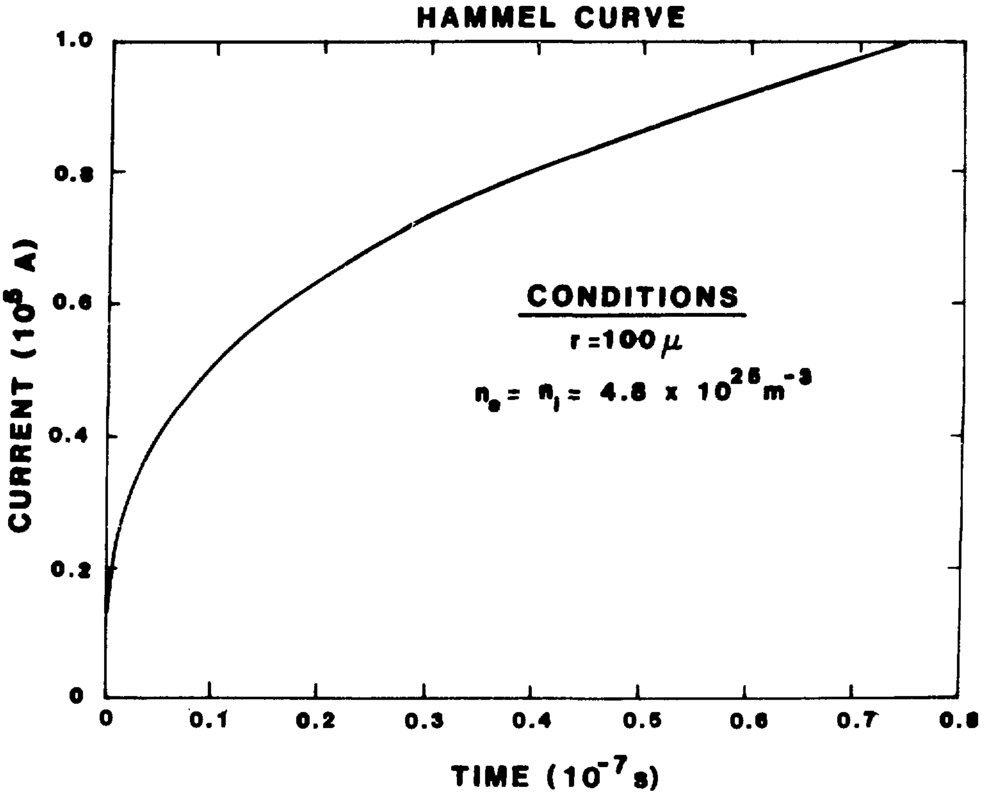

Fig. 3.1 Hammel equilibrium curve for typical plasma conditions

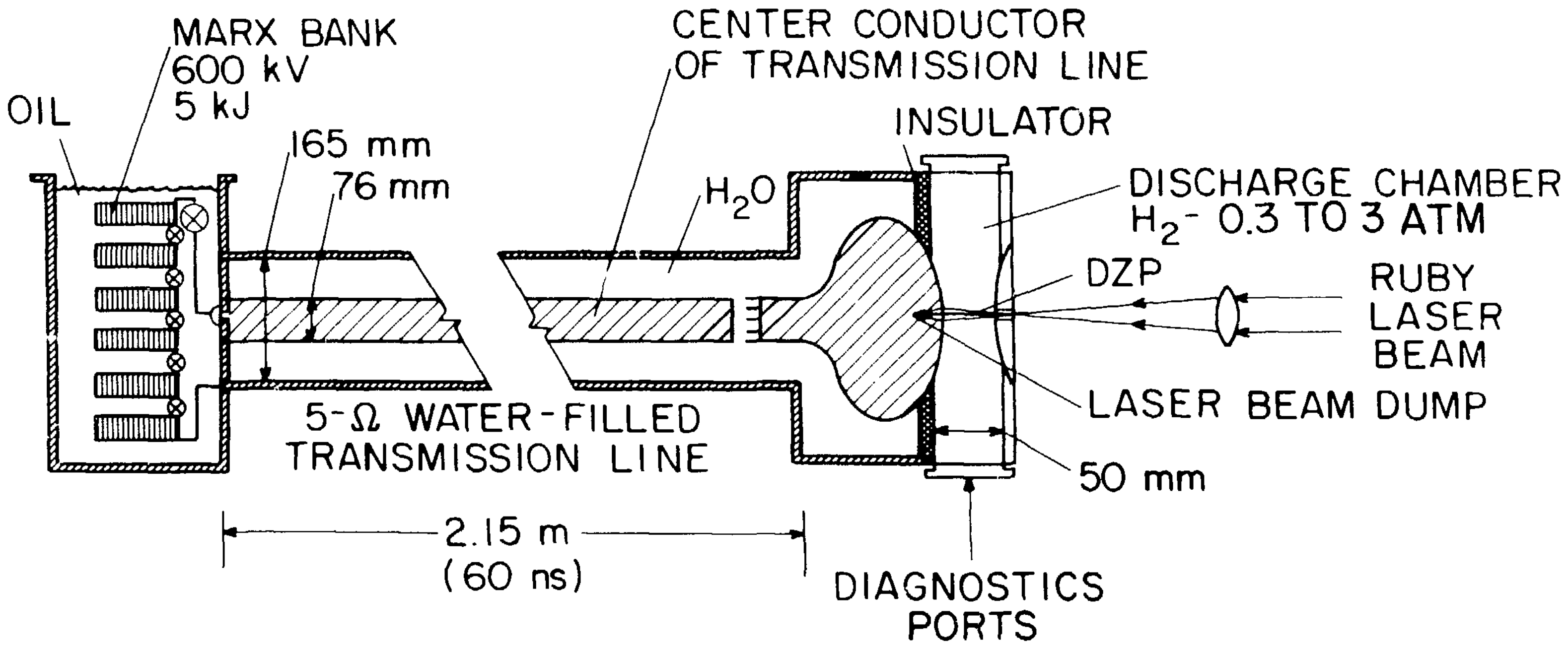

Fig. 3.2 Prototype High-Density Z-Pinch schematic

$$L_{plasma} \simeq \frac{\mu_o \ell}{2\pi} \ell n \; r_{out}/r_p \simeq 75 \text{ nH} \quad , \tag{3.2}$$

and combining (3.1) and (3.2), we obtain

$$V_{applied} \simeq L_{plasma} \dot{I} \simeq 400 \text{ kV} \quad . \tag{3.3}$$

Typical high voltage capacitors have 100 kV ratings, and Eq. (3.3) therefore suggests the use of a Marx bank generator,[5] consisting of capacitors which are charged in parallel, then rapidly switched to provide a series voltage multiplication. The prototype HDZP Marx generator, pictured in Fig. 3.3, is a six stage unit with twelve 0.1 μF 100 kV Maxwell Series S capacitors and six Physics International T670 triggered spark gap switches. The total stored energy of this generator is 6 kJ and is sufficiently small to allow rapid (≃ 20 s) charging using a modest power supply. The Marx is designed with a compact geometry to minimize the output inductance.[6] For machine operation without a water switch, the Marx inductance directly determines the current rise rate at the load, while for water switched operation, the proper performance of the switch again requires a minimized Marx inductance. By shorting the output of the Marx, the output inductance and series resistance of the generator can be measured, and for the HDZP unit, we find

$$L_{Marx} \simeq 0.8 \ \mu\text{H}$$

and (3.4)

$$R_{Marx} \simeq 0.4 \ \Omega \quad .$$

Additional compactness in the Marx construction is achieved by submerging the entire unit in a tank filled with Shell DIALA-AX high voltage transformer oil, which acts as an effective insulator for dc applications. An overhead 1/4 ton crane provides easy removal of the generator for maintenance and repair. When the Marx bank is erected, the effective capacitance is the series combination

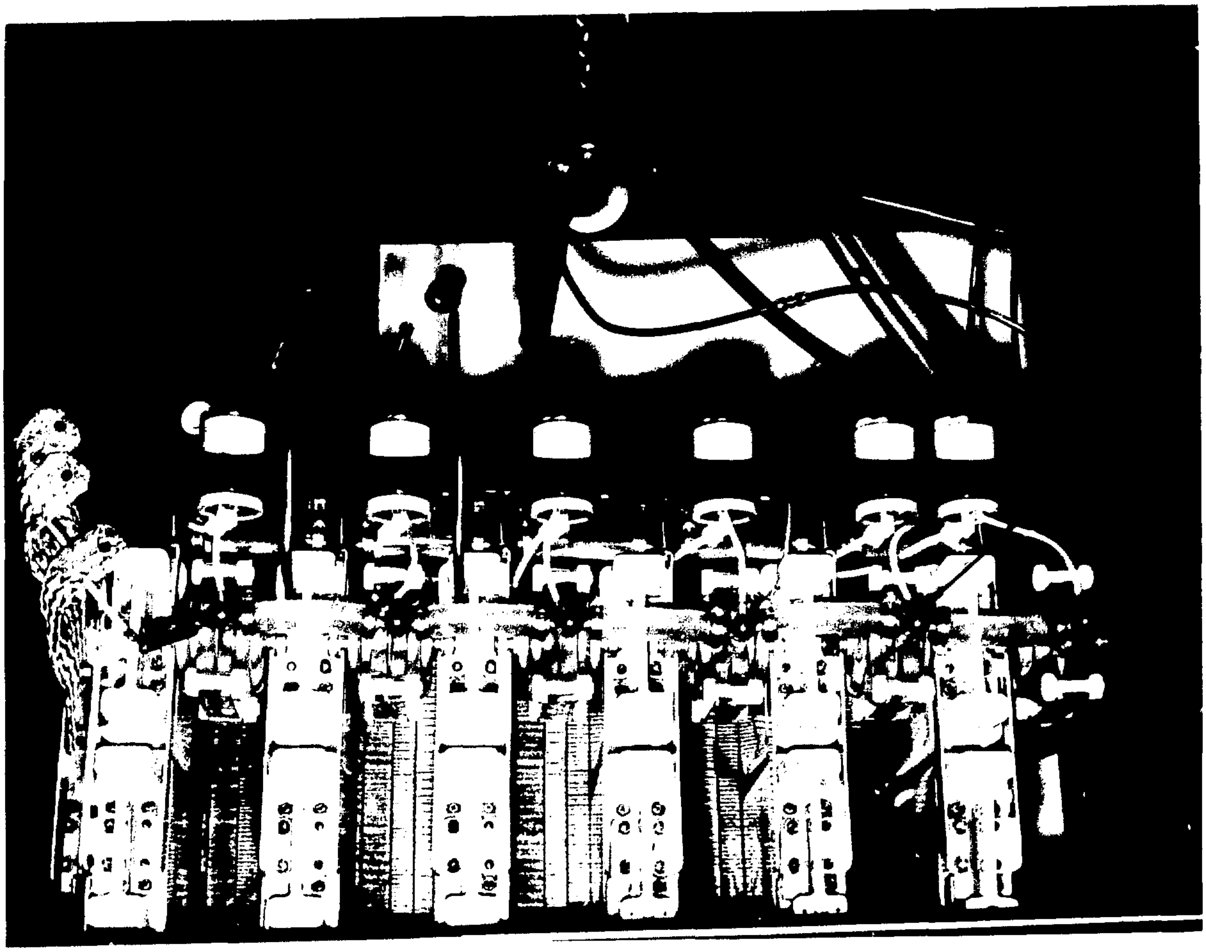

Fig. 3.3 Photograph of Marx bank generator

$$C_{Marx} \simeq 0.03\ \mu F \qquad (3.5)$$

so the Marx is underdamped, with

$$\left(\frac{L_{Marx}}{C_{Marx}}\right)^{1/2} \simeq 5\ \Omega >> R_{Marx} \quad . \qquad (3.6)$$

The first two spark gaps in the string are triggered externally by a low energy, fast pulse, 240 kV trigger generator (Micro-Marx),[7] and the closure of these two switches provides sufficient overvoltage to close the remaining four gaps. The Micro-Marx generator is completely enclosed in an aluminum cylinder which is pressurized with air at 40 psig. The eight-stage trigger generator uses "doorknob" capacitors and brass ball electrode spark gaps which are linearly arranged to take advantage of ultra-violet illumination from successive gaps. Each stage of the Micro-Marx can be charged to 30 kV, and triggering is provided by a 7 kV Krytron-switched pulse unit connected to the first gap trigatron electrode. The Krytron unit is an optically triggered system situated in the experimental area and contains an optical receiver section. This receiver diode and amplifier circuit responds to the output of a laser diode in the screen room through an optical fiber link. The use of fiber optics for triggering reduces the number of unwanted ground loops and greatly minimizes the noise level in the screen room; high frequency (300 MHz) analog signals, however, must still be transported along heavily shielded coaxial cables. Timing of the laser diode output pulse is controlled by a Cordin 438-10 delay generator, and the entire system up to the main Marx generator has a measured jitter of 5 ns. Jitter in the Marx generator is controlled to some extent by the pressure of the gas in the spark gaps. The Physics International gaps are filled with 8.5 psig of sulphur-hexafluoride (SF_6) which has a high affinity for electrons and thus allows operation at reduced pressures. Following each machine shot, the gaps are automatically flushed and refilled as a precautionary measure. Charging of the Marx bank is provided by a Universal Voltronics 100 kV, 50 mA power supply, and the ground, trigger, and charge strings in the bank all consist of liquid resistors. The resistors are an aqueous solution of either K_2SO_4 or $CuSO_4$ in a length of polyethylene tubing sealed with brass electrodes. A phenolic frame acts as a support structure for the Marx generator, and Fig. 3.4 is a schematic diagram of the capacitors, gaps, and resistors which form the bank. Also located in the oil tank are a resistive voltage divider monitor string and a chassis containing a large water resistor which acts as a safety dump for the Marx energy.

3.2 Water Transmission Line, Switch, and Load Chamber

The output of the Marx generator is coupled to the second major component of the HDZP system, a water transmission line. The line acts as a simple pulse forming network or intermediate capacitor storage and is composed of two coaxial aluminum cylinders with water between them. The spacing between the cylinders is determined by the voltage holdoff properties of the water;[8] for short pulses, water is an excellent insulator with a dielectric constant K = 80. The use of water as a dielectric reduces the system size both radially and axially. Because the speed of propagation of an electrical signal down the transmission line is

$$C_p = \frac{c}{n} = \frac{c}{K^{1/2}} \approx \frac{c}{9} \quad , \tag{3.7}$$

the water transmission line need only be 1/9 the length of an air dielectric line with the same transit time. The prototype HDZP has a 60 ns one-way transit (2 m) transmission line coupled to the Marx bank which is easily compatible with the physical limitations of the experimental area. The characteristic impedance of the transmission line determines the peak current through the load, and the design goal of 100 kA peak current using a 600 kV Marx bank constrains the line to

$$Z_{char} \lesssim 6\ \Omega \quad . \tag{3.8}$$

Lower impedance lines are more expensive and awkward to construct because the impedance only drops as the logarithm of the conductor diameter ratios; a 1 Ω system constitutes a rather momentous undertaking. The prototype device

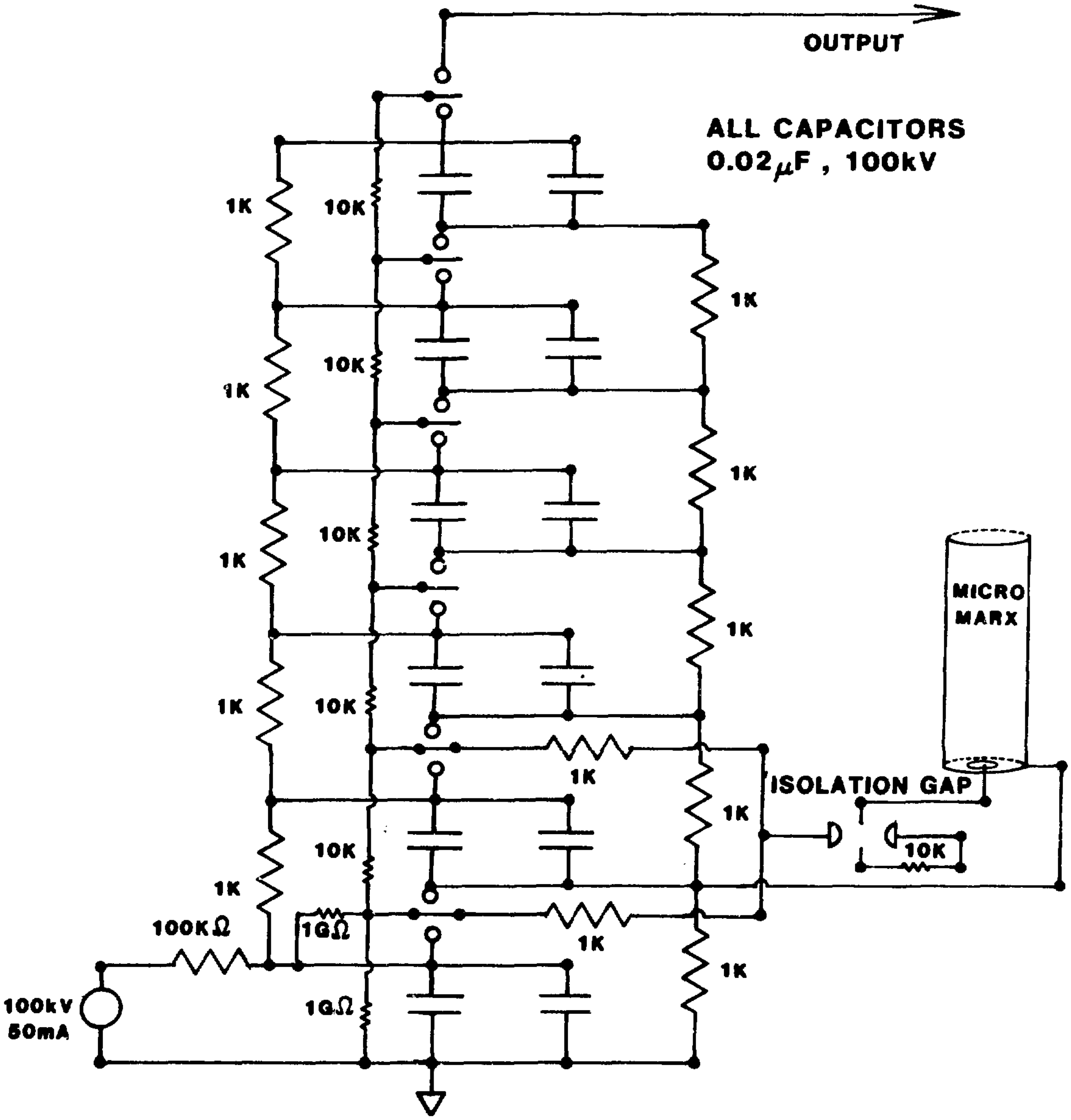

Fig. 3.4 Marx bank electrical schematic

therefore was designed using an outer cylinder diameter of 6.5 inches and an inner cylinder diameter of 3 inches, yielding

$$Z_{char} = \frac{1}{2\pi\varepsilon_o c} \frac{1}{K^{1/2}} \ln \frac{r_{outer}}{r_{inner}} = 5.2\ \Omega \quad . \tag{3.9}$$

Both cylinders are standard diameter aluminum tubes with 1/4 inch wall thicknesses. Because water has a finite resistivity, the transmission line will self-discharge in a characteristic time

$$\tau_{discharge} = R_L C_L = \varepsilon\eta \quad , \tag{3.10}$$

where η is the resistivity of the water and $\varepsilon = K\varepsilon_o$. For an experiment with a 100 ns characteristic time, we set

$$\tau_{discharge} \gtrsim 1\ \mu s \tag{3.11}$$

and find

$$\eta \gtrsim 1.4\times10^3\ \Omega\text{-m} \quad . \tag{3.12}$$

Ordinary tap water has

$$\eta_{tap} \simeq 10^2\ \Omega\text{-m} \quad , \tag{3.13}$$

and the need for deionized water is apparent. The prototype HDZP experiment is equipped with a deionizing system which can circulate and refresh approximately 3 gallons of water per minute. The connections between the transmission line and the Marx bank must maintain a low inductance. We couple the negative high voltage output of the Marx to the inner conductor of the line using a wide aluminum plate, while the outer conductor of the line bolts directly onto the oil tank which is tied to ground potential. The oil and water are separated by a one inch thick Lexan insulator, and a plexiglass viewing port on the opposite side of the oil tank allows visual observation down the line during a machine shot. This has proved to be a useful method to determine whether an undesirable breakdown has occurred between the two conductors. Using water in the transmission line has the advantage that the dielectric medium is self-healing after a breakdown. Standpipes are provided at all flange contacts in the transmission line to alleviate the problem of trapped air bubbles which can result in breakdowns.

The transmission line is directly coupled to a self-breaking water switch section which acts as a peaking gap to provide the load with both higher dV/dt and higher V than would be available otherwise. In effect, the switch isolates the plasma from the Marx output inductance and allows the 60 ns transmission line to fully charge before current flows through the load. The switch is a physical interruption in the inner conductor of the transmission line. The length of the gap between the two switch electrodes (~ 2 cm) is easily adjusted and determines the voltage at which the switch will self-break. For voltages below 1 MV,[9] it is preferable to have the cathode be a plane surface; in our experiment it is a 1/2" thick disc of tungsten-copper alloy known as elkanite. The ground side (anode) of the switch is composed of a number of sharp points formed from elkanite. Multi-channel closure of the water gap reduces the switch inductance and decreases the voltage drop across the gap. There is a limit to the number of channels which will form in the switch, however, because the channels must be physically distant enough from one another to avoid voltage reduction effects. Open shutter photographs of the prototype HDZP switch typically display 2-5 well formed channels, indicating a satisfactorily low switch inductance of ~ 5 nH. In addition, the switch exhibits a time dependent series resistance as a result of the breakdown processes associated with the water arcs. By monitoring the voltage trace on a probe near the water switch, the proper gap spacing can be determined, and it is adjusted using 3" diameter shims placed behind the elkanite cathode. Using the model of the water switch shown in Fig. 2.5c, network computer codes were run to optimize the design of the transmission line which couples the switch to the load chamber, based on an analysis of the predicted peak load current. The result of these simulations was a 15 ns one way transit, 5.2 Ω water transmission line section following the water switch. The prototype HDZP can be operated in two distinct modes to investigate different regimes of current rise rate at the load. In the shorted switch mode, the inner conductors of the 60 ns and 15 ns transmission lines are connected by a brass or copper sleeve, and the inductance of the Marx determines the relatively slow rate of rise of current at the load,

$$\dot{I}_{\text{short}} \simeq \frac{V_{\text{Marx}}}{L_{\text{Marx}}} \simeq \frac{6\times10^{5}\ \text{V}}{8\times10^{-7}\ \text{H}} \lesssim 8\times10^{11}\ \text{As}^{-1} \quad . \tag{3.14}$$

With the water switch in operation, we observe

$$\dot{I}_{\text{Switch}} \simeq \frac{V_{\text{Marx}}}{L_{\text{Plasma}}} \simeq \frac{6\times10^{5}\ \text{V}}{7.5\times10^{-8}\ \text{H}} \lesssim 8\times10^{12}\ \text{As}^{-1} \quad . \tag{3.15}$$

In practice, the Marx voltage rarely exceeds 400 kV, and $\dot{I}_{\text{Switch}} \lesssim 5\times10^{12}\ \text{As}^{-1}$.

Calibration of the electrical diagnostic probes and tests of the operation of the Marx, transmission line, and switch section are conducted with the aid of "dummy loads." In addition, these dummy loads test the circuit models used in the computer codes. Resistive and inductive dummy loads have been employed, and both are simple to construct and install. Typically, the load chamber must be filled with deionized water to prevent sparking along the surface of the dummy load. The resistive load which provides the most valuable information is a water resistor with the proper K_2SO_4 concentration, measured using a 1 KHz bridge, to produce 5.2 Ω. This load matches the transmission line impedance and represents a perfect termination, thereby eliminating reflections and allowing for analytical computation of the current and voltage waveforms at each probe location. The inductive dummy load is a 5 cm length of copper wire, typically 1/16" diameter, which bridges the gap in the load chamber. This load provides a reasonable electrical approximation to the plasma properties and tests the effects of reflections which can result in breakdown of the transmission line or voltage reversal damage to the Marx generator capacitors.

The aluminum load chamber is connected to the 15 ns transmission line in a wholly coaxial coupling; this feature is essential to reducing the stray inductance in series with the plasma which can limit $\dot{I}$. Systems have been built which allow for variation in transmission line impedance through the use of a parallel plate geometry,[10] but such devices suffer a large (~ 100 nH) inductance penalty at the crossover between the line and the load. In the prototype HDZP, the cathode in the plasma chamber is a simple extension of the inner conductor of the 15 ns transmission line, while the chamber walls and ground electrode are contiguous with the outer conductor of the line (Fig. 3.5), and virtually no inductance in series with the load is observed. The gas which normally fills the chamber is isolated from the water in the line by a one inch thick plexiglass insulator, which further acts as a mechanical support for the inner conductor of the transmission line. Return current is carried by 12 bolts which couple the chamber to the line. The load chamber, machined from a single block of aluminum, will easily withstand pressures up to 70 psia (5 atm) and is typically filled with high purity (99.999%) H_2 at 5-30 psia. The vacuum system for the load chamber illustrates a major advantage of high pressure backfilling with H_2; the simple and inexpensive components include only a mechanical forepump, an LN_2 cold trap, a thermister gauge, and associated valves (Fig. 3.6). A base pressure of 10 μ, which is sufficient for our experiments, is easily achieved, and the chamber can be cycled between atmospheric pressure and base pressure in 15 minutes. Diagnostic access to the chamber is provided by four viewing ports, each 4"×3", located symmetrically around the perimeter. These ports are sealed with 1/4" thick pyrex windows or with diagnostic devices.

3.3 Probe Diagnostics

Because of the transient nature of the experiment, all electrical signals from diagnostics are recorded photographically on high speed Tektronix 7844 dual beam 350 MHz bandwidth oscilloscopes. No affordable system consisting of fast digitizers and fiber optics is yet available which can obviate the use of oscilloscopes and signal cables. The oscilloscopes are housed in a double walled screen room; the inner wall is coupled to the outer wall by a bolt at one spot. Signal cables are all made from double shielded RG-223 50 Ω coaxial cable with BNC fittings, and they are additionally shielded by copper tube extensions of the outer screen room wall. Wherever possible, however, optical fibers are used to avoid ground loops. They are exclusively employed to provide diagnostic and Micro-Marx trigger signals and are used to pipe several optical signals into the screen room, where they are converted to electrical signals by photodetectors and recorded on oscilloscopes.

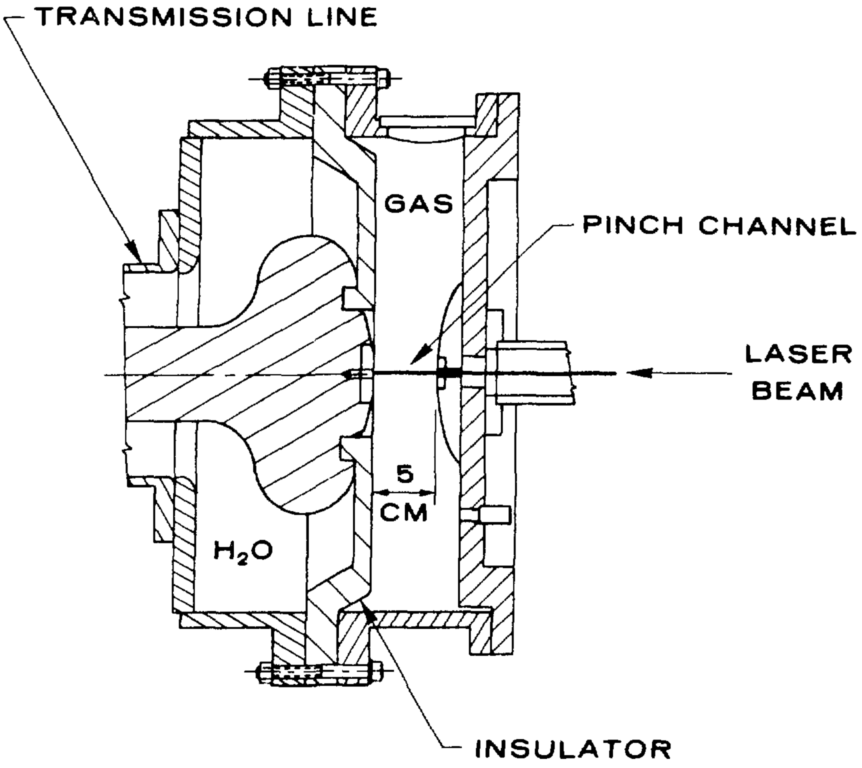

Fig. 3.5 Plasma load geometry

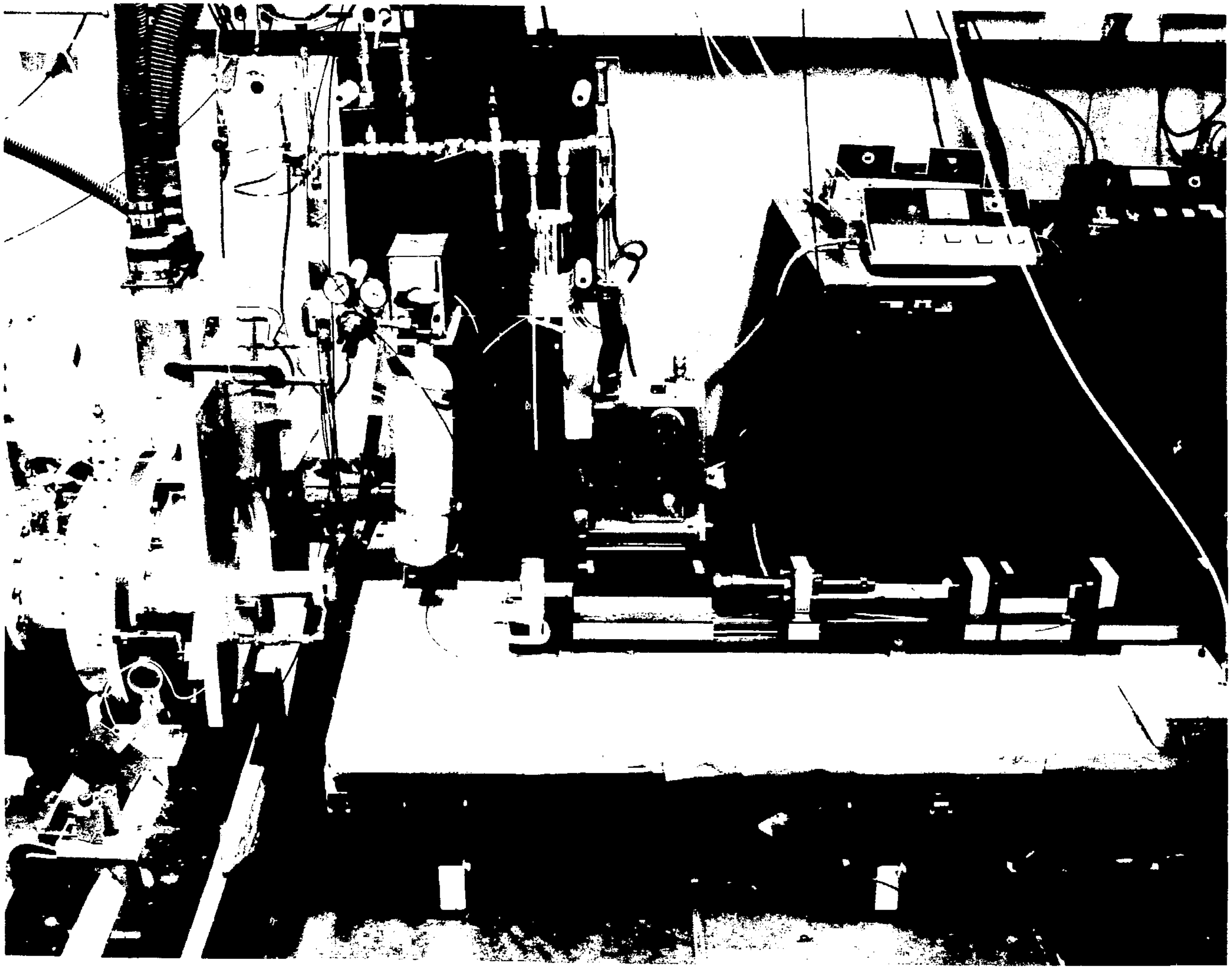

Fig. 3.6 Photograph of HDZP vacuum system and load chamber

The electrical properties of the Marx, line, switch, and load, are monitored with numerous current and voltage probes. The current probes (Fig. 3.7) are inductive shunts located at various flanges in the outer conductor of the transmission line. The shunts are formed by an annular channel which is machined into one of a pair of mating flange surfaces, with an insulating gap to force current flow around the channel.[11] Using the notation of Fig. 3.7, we find the voltage induced at the pickoff point from Maxwell's equations.

$$V = \frac{-d}{dt} \int B dr dz = - \frac{d}{dt} \int \frac{\mu_o I}{2\pi r} dr dz = - \frac{\mu_o}{2\pi} \frac{dI}{dt} \int \frac{dr dz}{r} \qquad (3.16)$$

and

$$L_{tot} = \frac{\mu_o}{2\pi} \int \frac{dr dz}{r} = \mu_o \frac{(w+\Delta)}{2\pi} \ell n \frac{r_o}{r_i} + \frac{\mu_o \Delta}{2\pi} \ell n \, r_i / r_p \qquad (3.17)$$

where r_p is the radius of the pickoff point. For the typical probes on the HDZP device, $r_o = 11.6$ cm, $r_i = 10.8$ cm, $\Delta = 0.15$ cm, $w = .64$ cm, and $r_p = 9.2$ cm, and the total inductance of the shunt, L_{tot} in (3.17), is given by the sum of two terms representing the contributions from the narrow insulating gap and from the machined channel.

$$L_{tot} = L_{channel} + L_{gap} = 0.113 \text{ nH} + 0.048 \text{ nH} = 0.16 \text{ nH} \qquad (3.18)$$

The current signal cable is terminated at both ends by 50 Ω carbon composition resistors to insure elimination of unwanted reflections, and this results in a reduction of the signal by a factor of 2. The signal is integrated at the oscilloscope by a passive RC network with a time constant RC = 5 μs, much greater than experimental times of interest. The capacitors in the integrators are of a low inductance feedthrough design. The resultant predicted current sensitivity from Eqs. (3.16) and (3.18) is

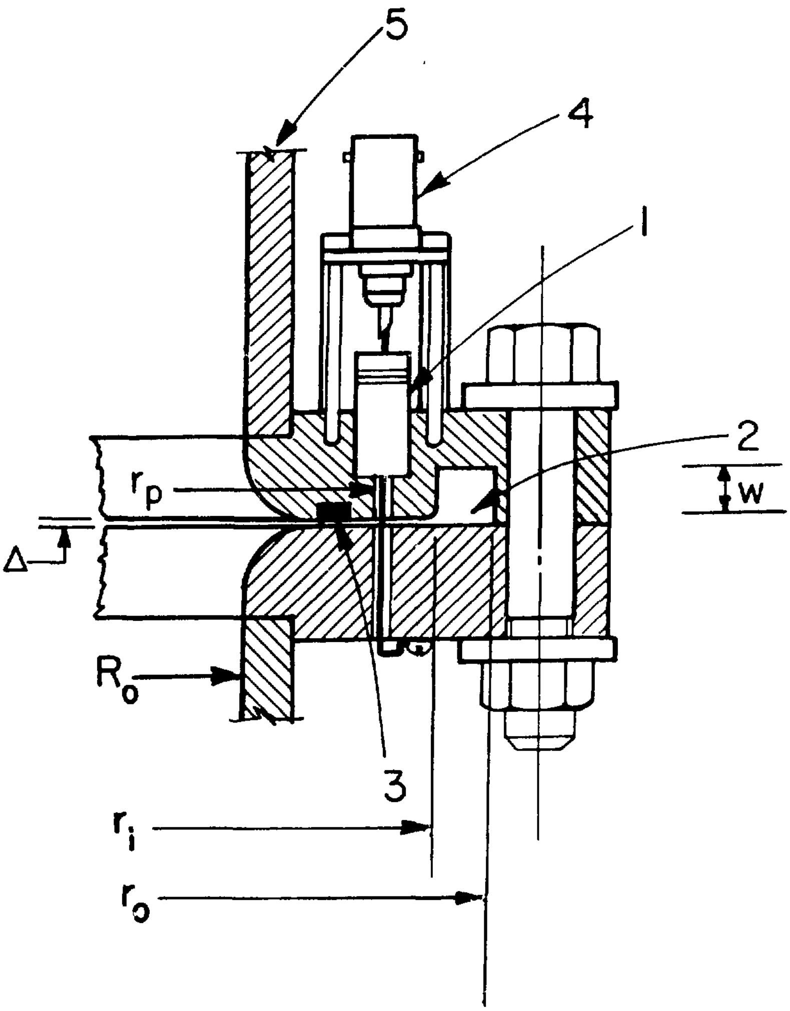

Fig. 3.7 Current probe [Reproduced from C. A. Ekdahl, R.S.I. 51, 1645 (1980)]

(1) Series resistor (50 Ω) connected to opposing flange by insulated wire at radius r_p

(2) Annular inductive channel machined in flange surface with outer radius r_o, inner radius r_i, and depth $(w+\Delta)$

(3) "O"-ring

(4) BNC cable connector

(5) Outer conductor of transmission line with radius R_o

$$V_{Scope} = \frac{0.16\ \text{nH}}{5\ \mu\text{s}} \frac{I}{2} \text{ or } \frac{V_{Scope}}{I} = 16\ \text{mV/kA} \quad (3.19)$$

which agrees with observations using dummy loads.

The voltages on the prototype HDZP are measured using capacitive dividers (Fig. 3.8), which offer numerous advantages over resistive dividers for multi-hundred kilovolt applications.[12] By coupling to the inner conductor high voltage electrode through the water, they eliminate surface breakdowns and reduce field distortions, and there is no requirement for voltage-grading rings or precision balanced components. These probes[11] contain a conducting disc which is insulated from the outer conductor by a teflon or acrylic sleeve and lies flush with the outer transmission line surface. The equivalent circuit of the probe (Fig. 3.9) is used to analyze the operating mode of this diagnostic. The capacitance to both the high voltage and ground conductors can be estimated by geometrical approximations. For the coupling capacitance through the water, we consider the probe surface to be a segment of a coaxial capacitor with a water dielectric, and

$$C_1 \simeq \frac{2\pi K_{water}\varepsilon_o \ell}{\ell n \dfrac{r_{outer}}{r_{inner}}} \left(\frac{A_p}{A_t}\right) \quad (3.20)$$

where A_p is the probe surface area and A_t is the total surface area of an annulus at the probe position. With $\ell \simeq 2a = 1.6$ cm, $A_p = \pi(0.8)^2 = 2.0\ \text{cm}^2$, $r_{outer} = 8.25$ cm, $r_{inner} = 3.81$ cm,
$A_t = 2\pi r_{outer}(2a) = 82.9\ \text{cm}^2$, and $K_{water} = 78$, we find

$$C_1 \simeq 2.2\ \text{pF} \quad . \quad (3.21)$$

We estimate C_2, the capacitance to ground through the insulating sleeve, ignoring fringing fields in the water, and again use a coaxial formula,

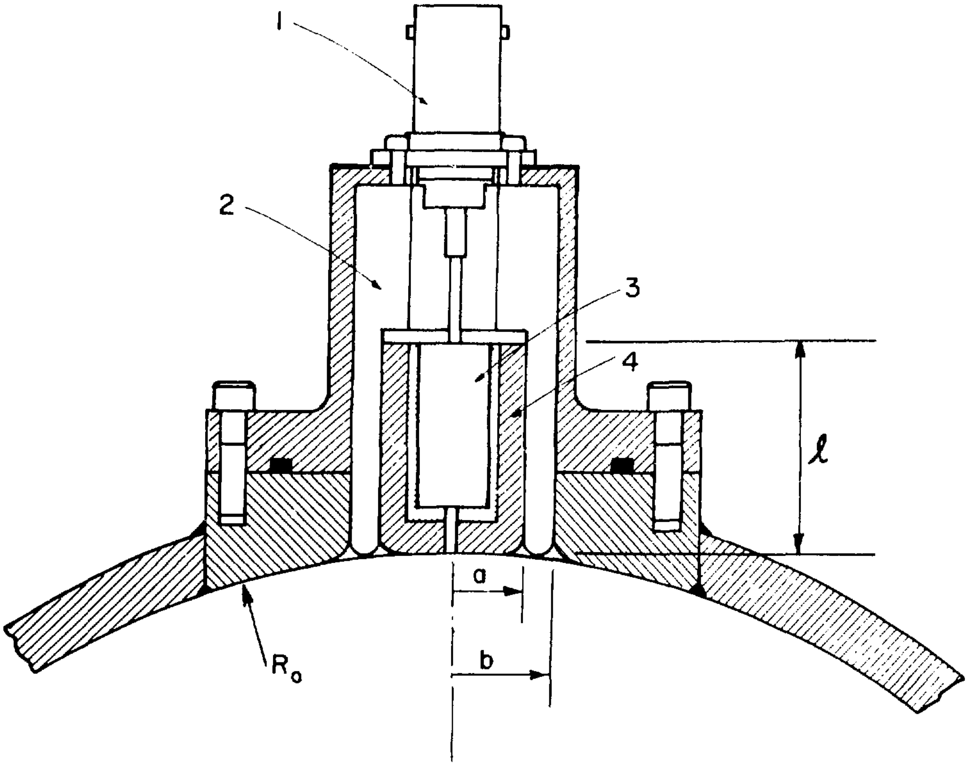

Fig. 3.8 Voltage probe [Reproduced from C. A. Ekdahl, R.S.I. 51, 1645 (1980)]

(1) BNC connector

(2) Teflon insulating sleeve

(3) Series resistor (50 Ω) soldered to coupling electrode

(4) Brass coupling electrode--Surface typically at outer radius of water transmission line, R_o

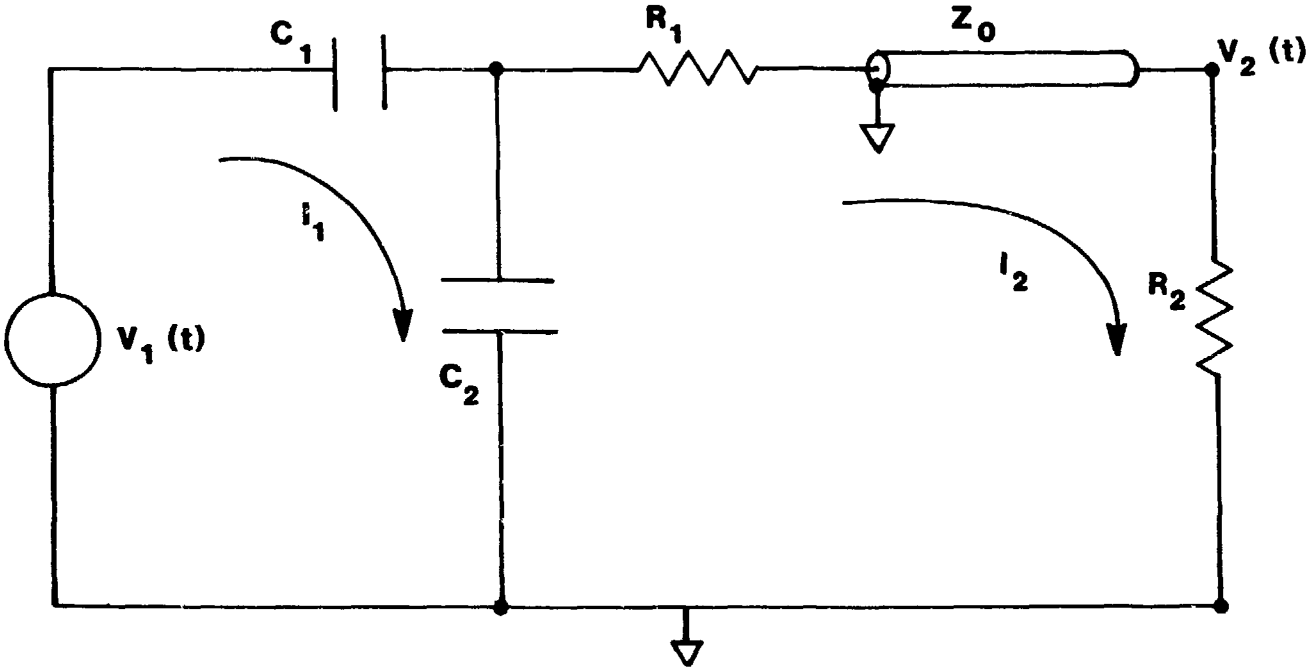

Fig. 3.9 Equivalent circuit of voltage probe

$$C_2 \simeq \frac{2\pi\varepsilon_o K_{Teflon}\ell}{\ell n\ r_{outer}/r_{inner}} \quad . \tag{3.22}$$

For $K_{Teflon} \simeq 2.1$, $\ell \simeq 2.3$ cm, $r_{outer} \simeq 1.1$ cm, and $r_{inner} \simeq 0.8$ cm, we find

$$C_2 \simeq 8.4 \text{ pF} \quad . \tag{3.23}$$

For a load resistance, R_2, matching the signal cable characteristic impedance, we obtain a differential equation relating the output voltage, $V_2(t)$, to the input voltage, $V_1(t)$, using the circuit of Fig. 3.9.

$$\frac{dV_1}{dt} = \frac{I_1}{C_1} - \frac{(I_1-I_2)}{C_2} \tag{3.24}$$

$$I_2R_2 = V_2$$

$$\frac{I_1-I_2}{C_2} = \frac{dI_2}{dt} R_1 + \frac{dV_2}{dt}$$

Thus

$$\frac{C_1R_2}{RC}\frac{dV_1}{dt} = \frac{dV_2}{dt} + \frac{V_2}{RC} \tag{3.25}$$

where

$$R = R_1 + R_2 \text{ and } C = C_1 + C_2 \quad .$$

The voltage probes for the prototype HDZP have

$$R_1 = R_2 = 50\ \Omega \quad , \tag{3.26}$$

and using numbers from (3.21) and (3.22) we calculate

$$RC \simeq 1\times10^{-9}\ \text{s} \quad . \tag{3.27}$$

For RC much less than the fastest time scale of interest ($RC \ll \tau_{\text{signal}}$), Eq. (3.25) reduces to

$$C_1 R_2 \frac{dV_1}{dt} \simeq V_2 \tag{3.28}$$

and our probes are therefore operated in the "V-dot" mode. A passive RC integrator with 5 μs time constant is used at the oscilloscope to allow direct voltage measurements.

3.4 Optical Diagnostics

The high electric fields in the load chamber preclude the use of conventional physical probes and motivate the development of nonperturbing optical diagnostics. To date, optical techniques have allowed measurement of plasma column size and gross behavior, electron density profile, and overall symmetry. The dispersion relation for electromagnetic waves in the plasma is

$$\omega^2 = \omega_{p_e}^2 + k^2c^2 \tag{3.29}$$

where

$$\omega_{p_e} = \left(\frac{ne^2}{\varepsilon_o m}\right)^{1/2} \simeq 57\sqrt{n}\ \text{s}^{-1} \quad . \tag{3.30}$$

For frequencies well above ω_{p_e}, Eq. (3.29) becomes

$$\mu-1 \approx -\frac{\omega_{p_e}^{2}}{2\omega^{2}} \tag{3.31}$$

where μ is the index of refraction of the plasma. For an electron density of $10^{26}\ m^{-3}$, we constrain the optical wavelengths for a diagnostic source by the relation

$$\lambda_{opt} << 33000\ Å \tag{3.32}$$

to avoid absorption or severe refraction, and this suggests an ultra-violet laser. Further constraints on the source are set by data acquisition techniques and the short plasma lifetime; recording on a time-integrating medium, i.e., photographic film, requires a short duration light pulse to avoid smearing resulting from plasma motion. The N_2 superluminescent laser[13,14,15] emitting light at 3371 Å has been particularly valuable as a diagnostic source on the prototype HDZP because of both its short wavelength and short pulse length. Temporal output of our inexpensive and easily constructed N_2 laser has been measured with a fast risetime (0.5 ns) vacuum photodiode (ITT FW114A) and a Tektronix 519 direct input (0.3 ns) oscilloscope, and we have observed a pulse with FWHM of 3 ns. This is sufficiently short to prevent blurring and eliminates the need for costly and complicated fast shutters. The N_2 laser (Fig. 3.10) has a transverse discharge configuration with a Blumlein pulse forming network and a triggered spark gap switch (Fig. 3.11). The discharge tube, filled with 0.1 atm N_2, is 3.9 cm diam and 1.0 m long and is sealed by a flat mirror at the back end and a window at the front. There is no front mirror in the "optical cavity," and the light uses only a single pass gain before exiting. The air-filled spark gap has a trigatron design and is triggered by the output of an optical receiver Krytron-switched 7 kV unit identical to that used with the Micro-Marx. Measured jitter for this system is approximately 20 ns and does not allow complete control of the laser timing with respect to other diagnostics. The vacuum photodiode pick-off monitor, however, gives accurate post-shot information used in the data analysis. By reducing the air

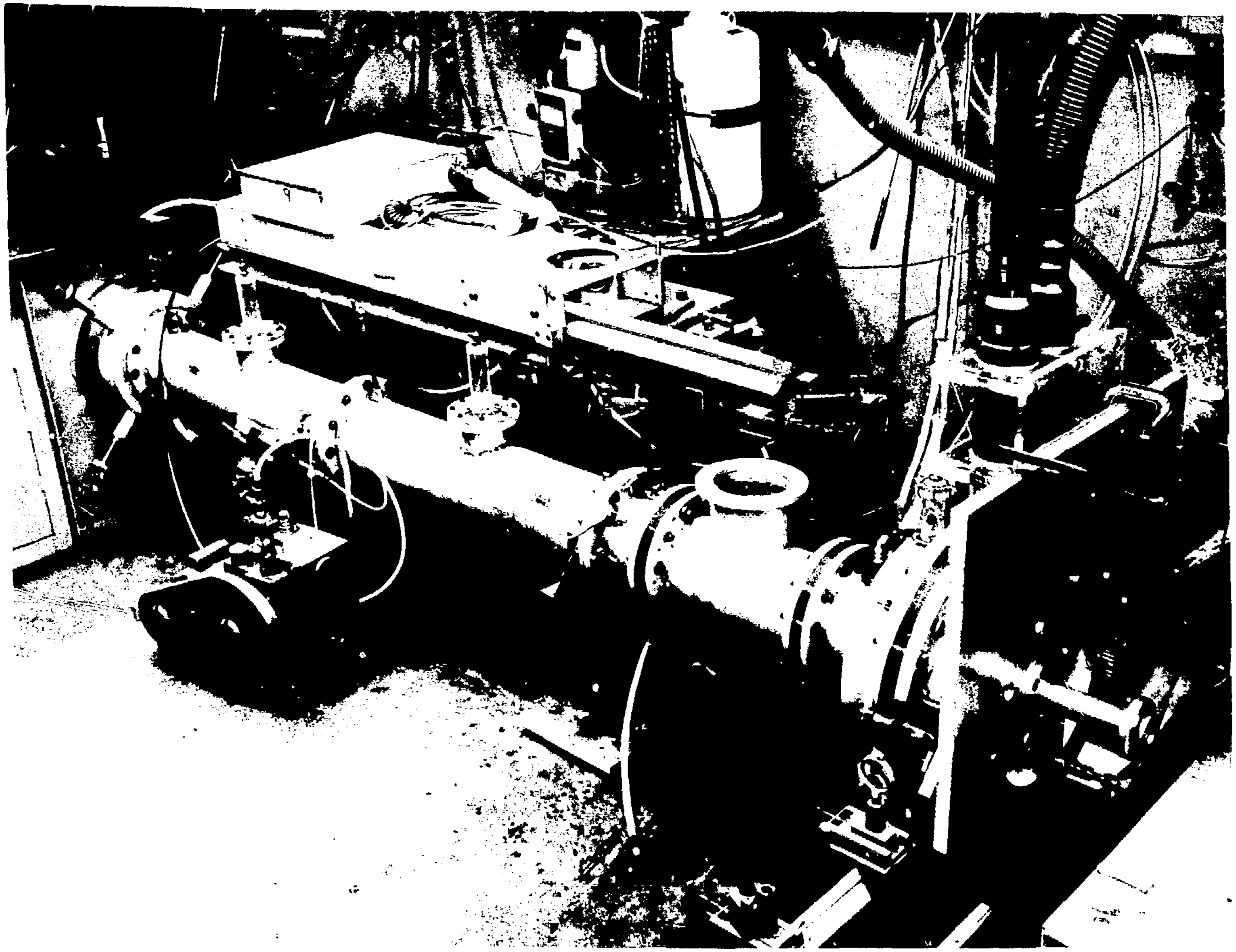

Fig. 3.10 Photograph of prototype HDZP water line with aluminum shield box and optical rail from N_2 laser visible in the background

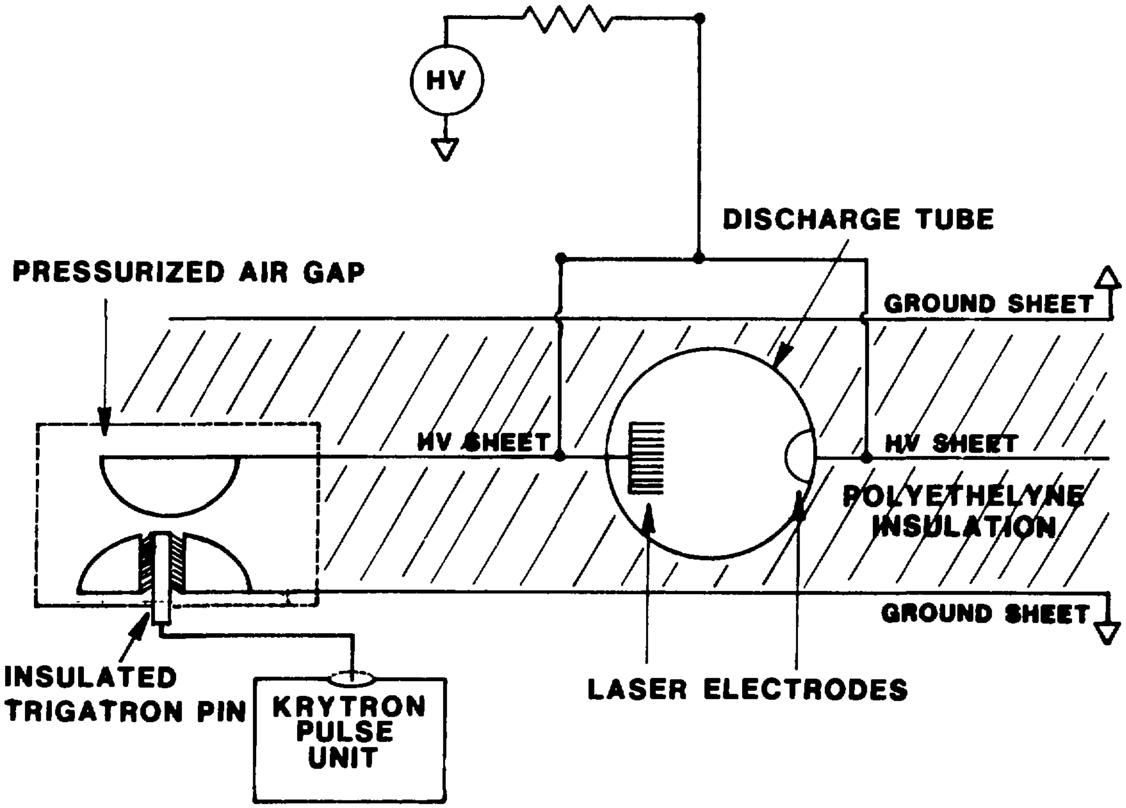

Fig. 3.11 N_2 laser Blumlein circuit

pressure in the spark gap below the hold-off value for the Blumlein charge voltage (14 kV), the laser can be operated in a relaxation oscillator mode, producing one pulse per second. This mode is useful during alignment, and the beam location is traced through the diagnostic system with fluorescent orange tape.

The simplest N_2 laser diagnostic to construct is a pinhole Schlieren-shadowgraph scheme shown in Fig. 3.12. The laser beam is transmitted through the load chamber ports transverse to the z-axis of the plasma. The light then passes through a lens (typically 30 cm focal length) which images the plasma onto a film plane. At the focus of the lens, a pinhole (typical diameter 1.5 mm) is placed which obstructs only light which has been refracted by an angle greater than θ_{min}, given by

$$\theta_{min} = \frac{r_{pin}}{f} \tag{3.33}$$

where r_{pin} is the pinhole radius and f is the focal length of the lens. The lens preserves an image-object relation, and thus a dark region on the film corresponds to a region of plasma which causes refraction exceeding θ_{min}. We can estimate the refraction angle, α, caused by the plasma using the Schlieren formula,[16]

$$\alpha_{refraction} = \int_o^{\ell} \frac{1}{\mu} \frac{\partial \mu}{\partial y} dx \quad , \tag{3.34}$$

where the beam travels along the x-axis a distance ℓ and $\partial\mu/\partial y$ is the index gradient perpendicular to the beam. Using Eqs. (3.31) and (3.34) we find

$$\alpha_{refraction} \simeq - \Delta\ell \frac{\partial n_e}{\partial y} \frac{r_e}{2\pi} \lambda^2_{laser} \tag{3.35}$$

where r_e is the classical electron radius. For a column with radius 100 μ and density 10^{26} m^{-3}, we estimate

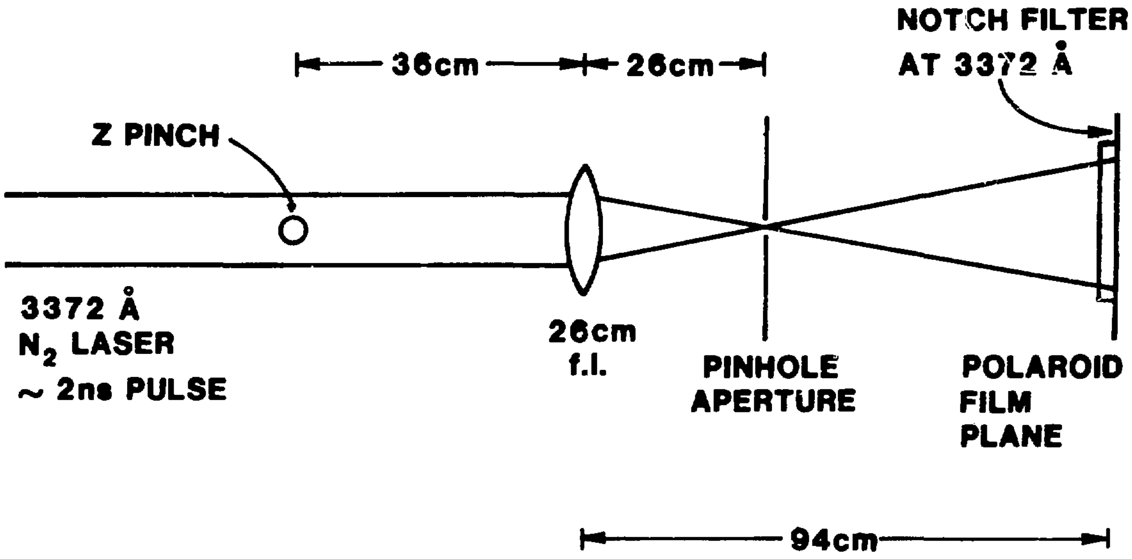

Fig. 3.12 Pinhole Schlieren optical configuration

$$\alpha_{\text{refraction}} \simeq 10^{-4} \left(\frac{10^{26}}{10^{-4}}\right) \frac{2.8\times10^{-15}}{2\pi} (3.37\times10^{-7})^2 = 5 \text{ mrad} \tag{3.36}$$

while from (3.33),

$$\theta_{\min} = \frac{7.5\times10^{-4}}{3\times10^{-1}} = 2.5 \text{ mrad} \quad , \tag{3.37}$$

and we might expect some Schlieren exposure for these parameters. To reduce film fogging from plasma light, the aperture of the camera is covered by a notch dielectric filter with peak transmission at 3371 Å and 100 Å bandwidth. Additional filtering, if necessary, is provided by neutral density filters, and exposures are made on Polaroid Type 107 film which has good response in the soft ultraviolet. The imaging system results in a magnification of 3:1, and 10 μ features in the plasma are easily resolved. While the Schlieren diagnostic provides a qualitative view of the refractive region, it is incapable of easily supplying quantitative information about the plasma electron density. In addition, no distinction is made between refraction caused by electrons and that resulting from neutral gas shock waves. The conventional diagnostic for determining electron density is an interferometric scheme which examines phase changes, given by

$$\Delta\phi = \int (\mu-1) \frac{\omega_{\text{laser}}}{c} d\ell \simeq r_e \lambda_{\text{laser}} \int n_e d\ell \tag{3.38}$$

using Eq. (3.31). Coherence problems in the N_2 laser output lead to difficulties in obtaining high quality fringes, however, and we have therefore developed a novel diagnostic[17] which uses the plasma refractivity to obtain quantitative density information. This Moiré-Schlieren technique interposes two coarse Ronchi transmission gratings between the plasma and the imaging lens (Fig. 3.13). The gratings, with 26 lines per mm, are oriented with the rulings nearly parallel to the plasma symmetry axis, and a slight angular misalignment between the plates results in beat or Moiré fringes. These fringes can be

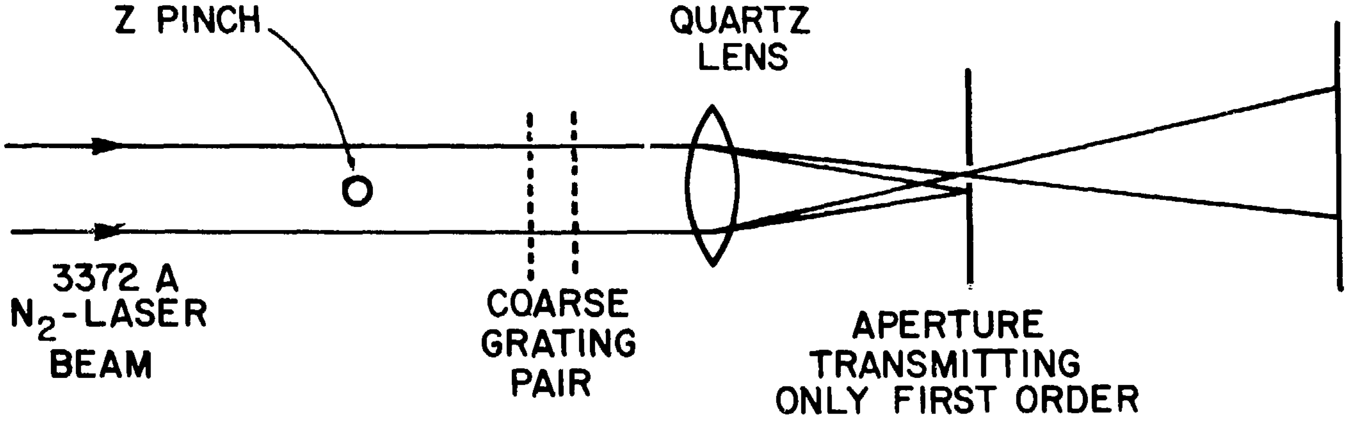

Fig. 3.13 Moiré-Schlieren optical configuration

predicted from geometrical optics[18] and are simply the shadows cast by one set of grating lines through a second similar set (Fig. 3.14). In actuality, a number of orders of Moiré fringes are observed at the focus of the lens because of diffraction through the gratings,[19] and a pinhole is used to select a single order. The first off-center order is typically chosen, as it provides the best combination of intensity and contrast. The sensitivity of the Moiré-Schlieren diagnostic is controlled by the separation, d, between the two gratings and the coarseness of the gratings. A ray which passes through the gratings at an angle $\phi_\perp$ given by

$$\phi_1 = \frac{\Delta}{d} \quad , \tag{3.39}$$

where Δ is the distance between lines on the grating, will exhibit a full fringe shift. For $\Delta = 3.85\times10^{-3}$ cm and d = 2.0 cm,

$$\phi_1 = 1.9 \text{ mrad} \tag{3.40}$$

which is comparable to the refraction expected from the plasma in Eq. (3.36). The fringe deflection essentially provides a continuous quantitative Schlieren measurement and is a multiple extension of the inclined-slit Schlieren technique.[20] An additional advantage of the Moiré diagnostic over conventional Schlieren is its ability to differentiate between refractive regions with index greater than unity (compression shocks) and those with index less than unity (electrons) by detecting the direction of the fringe excursion from its background position. For cylindrically symmetric refractive objects, the observed fringe shifts can be unfolded by Abel inversion to yield the radial density gradient profile, then integrated to find the density profile, with the assumption that the object acts as a thin lens and does not displace rays. The thin lens approximation is valid for plasma columns of 100 μ diameter with refraction angles of 5 mrad as this corresponds to a displacement of

$$\delta < 5 \text{ mrad} \times 100\ \mu = 0.5\ \mu \quad , \tag{3.41}$$

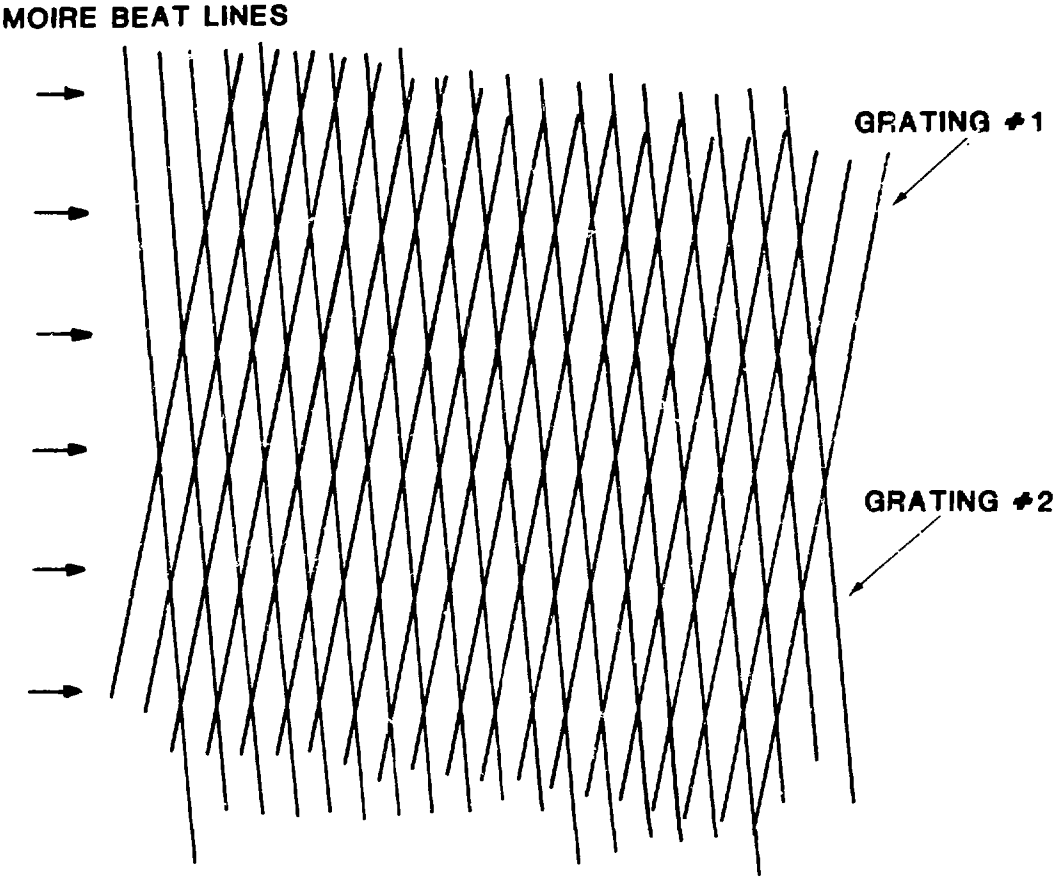

Fig. 3.14 Moiré pattern generated by crossed gratings

which is well below the resolution of the diagnostic. Test objects have been inserted at the position of the plasma to confirm the Moiré diagnostic data interpretation. An SF_6 gas jet from a small needle nozzle easily deflects the background fringes and establishes the direction corresponding to index greater than unity, while a cylindrical lens produces a constant angular shift of the fringe pattern for quantitative calibration of the refraction angle sensitivity.

The unfolding technique begins with the Schlieren formula, Eq. (3.35), and divides the cylindrical refraction region into discrete concentric annuli (Fig. 3.15a).[21] We assume the density gradient within a shell of inner radius r_i to be constant with a value $(\partial n/\partial r)_i$. The innermost cylinder in this analysis has a uniform density, and radius r_1, and the total channel has a radius r_N. There are N-1 nontrivial shells. Rays are denoted by the subscript of the radius of the innermost shell to which they are tangent, r_j, which is effectively an impact parameter. The traversal distance ℓ through annulus r_i for ray r_j is shown in Fig. 3.15b,

$$\ell = (r^2-r_j^2)^{1/2} - (r_i^2-r_j^2)^{1/2} \tag{3.42}$$

or

$$d\ell = \frac{rdr}{(r^2-r_j^2)^{1/2}} , \tag{3.43}$$

while the transverse density gradient is related to the radial gradient by

$$\frac{\partial n}{\partial y} = \sin\psi \frac{\partial n}{\partial r} = \frac{r_j}{r}\frac{\partial n}{\partial r} . \tag{3.44}$$

Thus the refraction suffered in shell r_i is

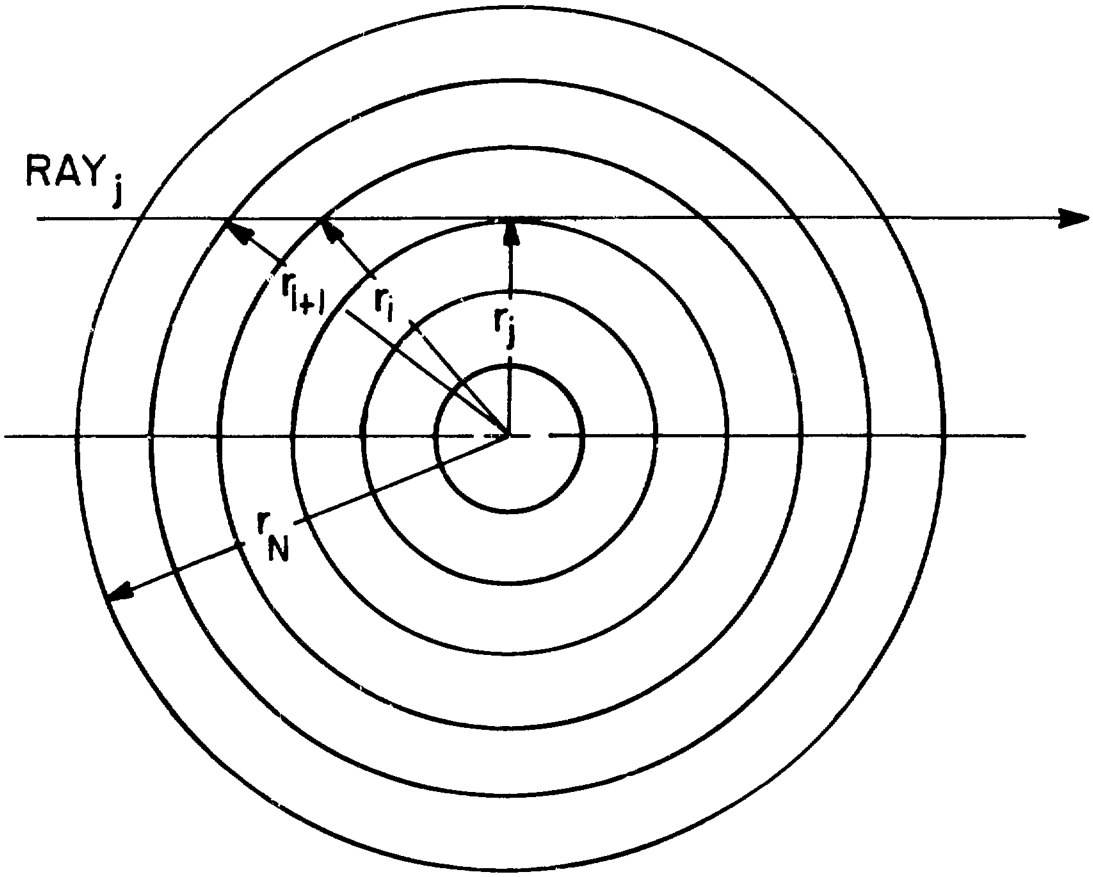

Fig. 3.15(a) Cylindrical geometry for Abel inversion of Moiré results

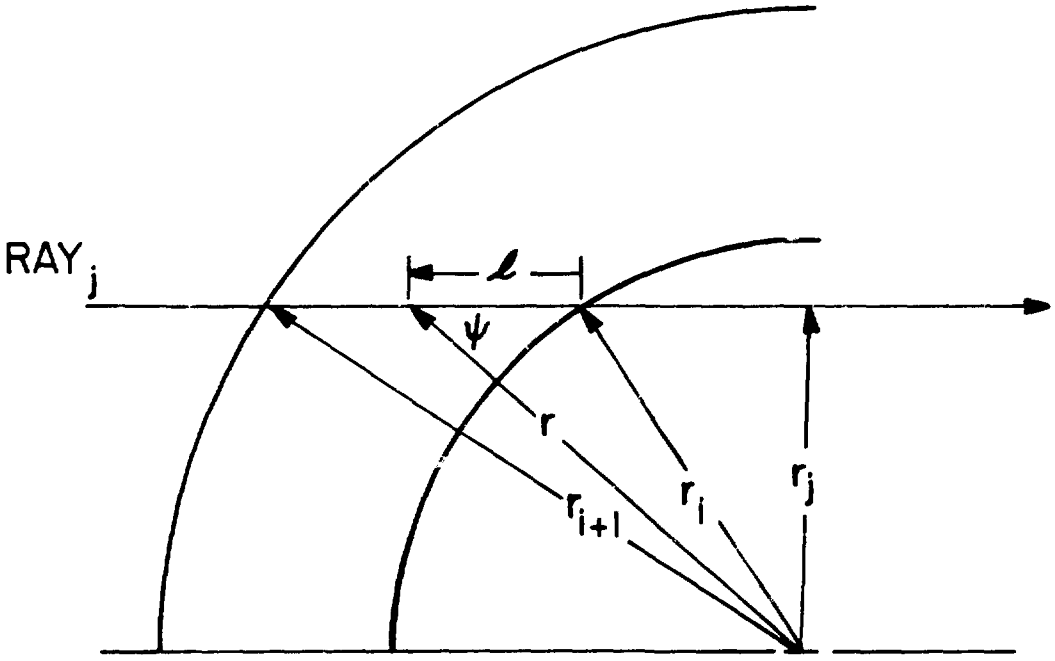

Fig. 3.15(b) Ray traversal through a single annulus
[Reproduced from M. Raleigh and J. R. Grieg, NRL Memorandum report 4390 (1981)]

$$\Delta\theta = 2 \int \frac{\partial n}{\partial y}\, d\ell = - \frac{\lambda_L^2 r_e}{\pi} \int_{r_i}^{r_{i+1}} \frac{r_j dr}{(r^2-r_j^2)^{1/2}} \left(\frac{\partial n}{\partial r}\right)_i \tag{3.45}$$

$$= - \left(\frac{\partial n}{\partial r}\right)_i \frac{\lambda_L^2\, r_e}{\pi}\, r_j\, \ell n \left(\frac{r_{i+1} + (r_{i+1}^2-r_j^2)^{1/2}}{r_i + (r_i^2-r_j^2)^{1/2}}\right) .$$

The full refraction angle for the ray with impact parameter j, using the thin lens approximation, is given by a summation of (3.45) over the shells outside r_j,

$$\theta_j = \frac{-\lambda_L^2\, r_e r_j}{\pi} \sum_{i=j}^{N-1} \left(\frac{\partial n}{\partial r}\right)_i \ell n \left(\frac{r_{i+1} + (r_{i+1}^2-r_j^2)^{1/2}}{r_i + (r_i^2-r_j^2)^{1/2}}\right) . \tag{3.46}$$

The unfolding scheme involves separating the first term of the summation from the remaining terms, or equivalently, finding the density gradient in a given shell from information about all the shells outside it. Using (3.46), we have

$$\frac{\theta_j}{r_j} = \frac{-\lambda^2{}_L\; r_e}{\pi} \left.\frac{\partial n}{\partial r}\right)_j \ell n\, \frac{r_{j+1} + (r_{j+1}^2-r_j^2)^{1/2}}{r_j}$$

$$- \frac{\lambda_L^2\; r_e}{\pi} \sum_{i=j+1}^{N-1} \left.\frac{\partial n}{\partial r}\right)_i \ell n \left(\frac{r_{i+1} + (r_{i+1}^2-r_j^2)^{1/2}}{r_i + \left(r_i^2-r_j^2\right)^{1/2}}\right) \tag{3.47}$$

or

$$\left.\frac{\partial n}{\partial r}\right)_j = -\frac{\theta_j \pi}{r_j \lambda_L^2 r_e \ln\left(\frac{r_{j+1} + (r_{j+1}{}^2 - r_j^2)^{1/2}}{r_j}\right)}$$

$$-\sum_{i=j+1}^{N-1} \left.\frac{\partial n}{\partial r}\right)_i \frac{\ln\left(\frac{r_{i+1} + (r_{i+1}^2 - r_j^2)^{1/2}}{r_i + (r_i^2 - r_j^2)^{1/2}}\right)}{\ln\left(\frac{r_{j+1} + (r_{j+1}^2 - r_j^2)^{1/2}}{r_j}\right)} \quad . \tag{3.48}$$

Finally,

$$n_j = n_{j+1} - \left.\frac{\partial n}{\partial r}\right)_j (r_{j+1} - r_j) \tag{3.49}$$

allows us to integrate the density gradient to find the density profile. Equation (3.48) is a solution algorithm, easily adapted to a computer, which calculates the density gradient in a given shell based on knowledge of the gradient in each shell beyond it and the angular deflection, θ_j, at that impact parameter. The θ_j information is contained in the Moiré fringe deflection through the diagnostic sensitivity and involves determining the fractional fringe shift as a function of impact parameter. We can analyze a simple test fringe pattern (Fig. 3.16a) and find the resultant density profile in Fig. 3.16b. The Moiré diagnostic also provides a measurement of electron line density by numerical integration of the density profile, and this quantity is a requisite to estimating a Bennett equilibrium temperature for the plasma.

3.5 Temperature Diagnostics

The direct measurement of temperature on the prototype experiment is a formidable task because of the high electron density and small channel dimensions in an HDZP plasma relative to more conventional magnetically confined plasmas. Thomson scattering is virtually impossible for the conditions of $n_e = 10^{26}$ m^{-3} and $T_e \sim 200$ eV because collective effects in the cloud surrounding a test electron overshadow the Doppler shift caused by thermal

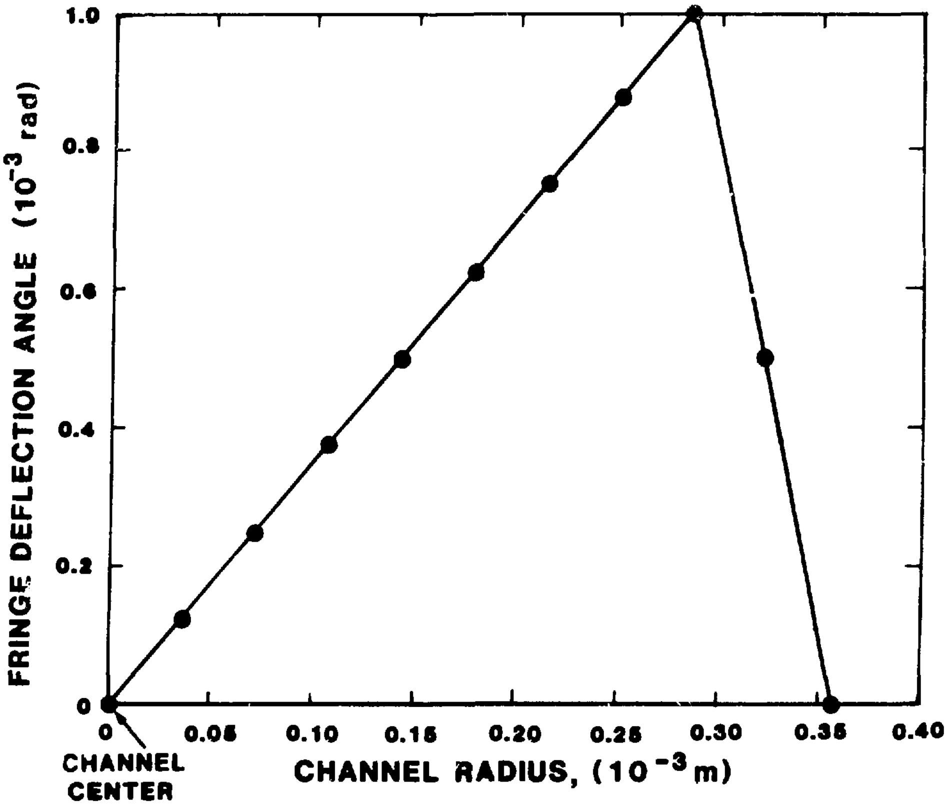

Fig. 3.16(a) Test fringe pattern for Moiré-Schlieren inversion algorithm

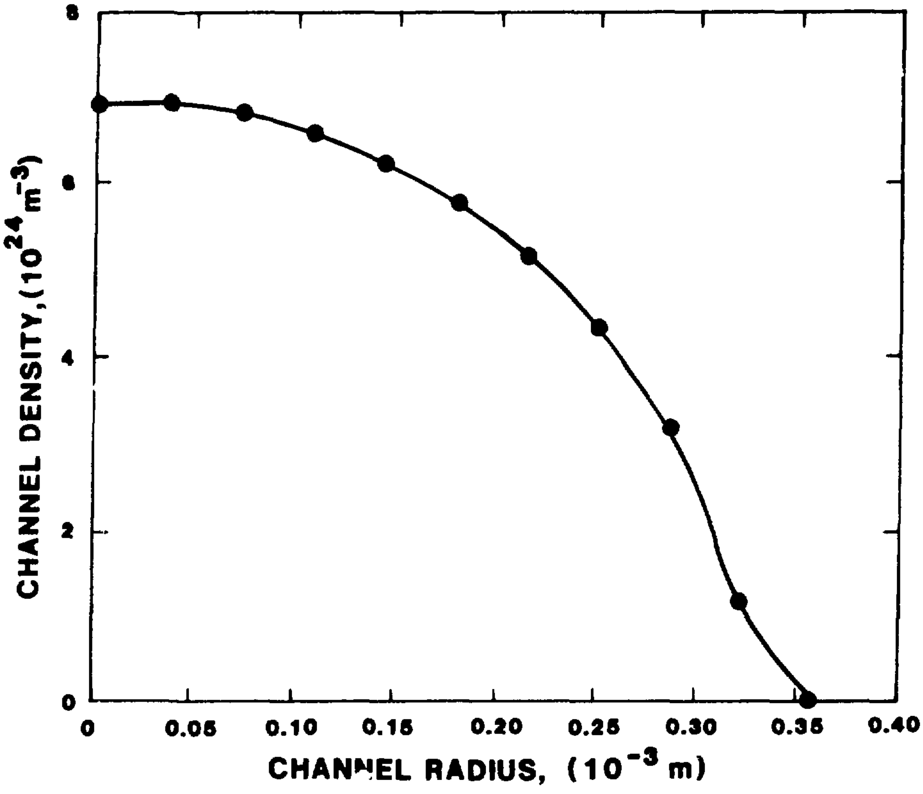

Fig. 3.16(b) Density profile obtained from test fringe pattern

motion. Using a ruby laser and the plasma conditions above, we find the scattering parameter

$$\alpha \simeq \frac{1}{2K_{\mathrm{Laser}}\sin(\theta/2)\lambda_{D_e}} \gtrsim 10 \gg 1 \tag{3.50}$$

while Thomson scattering usually requires $\alpha < 1$.[22] Furthermore, the laser power density needed for a signal-to-noise ratio greater than unity would perturb the neutral hydrogen surrounding the plasma and possibly result in optical breakdown of the gas.

Spectroscopic measurements are often used as a temperature diagnostic but are plagued by spatial resolution problems for an HDZP plasma. Any line or continuum observation involves some integration along the line of sight, and it is not possible to localize the viewing volume to the plasma column itself. A surrounding coronal region might radiate effectively at a temperature well below that of the main channel and invalidate measurements based on line ratios for different ionization species. We have, nevertheless, obtained some results using quartz-UV spectroscopy on the prototype HDZP experiment. Because of the high pressure backfilling of the chamber (~ 1 atm H_2), no emission from impurities was readily detected, and a small fraction (~ 3 atomic %) of methane (CH_4) was added to the fill gas. Spectral line broadening of all but lithium-like ionization states is several hundred angstroms as a result of the Stark effect at high densities; thus, only emission from CIII and CV was of interest. Time-resolved information at 2297 Å (CIII) and at 2273 Å (CV) using 1P28 photomultipliers at the output of a Jarrell-Ash 1/4 m monochromator was obtained but has not proved to be particularly useful. The detection of any emission from CV probably implies a lower bound temperature of 45 eV,[23] but no upper bound can be easily determined by spectroscopic means.

Fusion neutrons produced in D-D reactions are a sensitive temperature diagnostic in many magnetic confinement devices; the total yield is a strong function of ion temperature in the range 100 eV-10 keV. One difficulty is that the measurements are based on the high-energy tail of the distribution because of the cross-section energy dependence, and one must make inferences about the Maxwellian nature of the ions. For the reactivity of an isotropic Maxwellian ion velocity distribution,[24] we use

$$\langle\sigma v\rangle_{DD} = 1.17\times10^{-14}\ T_i^{-2/3}\ \exp(-18.76/T_i^{1/3})\ \mathrm{cm^3/s} \tag{3.51}$$

with T_i in keV, and the total emission rate, R, is

$$R \simeq \pi r_p^2 \ell n_i^2\ \langle\sigma v\rangle_{DD}\ \ \text{neutrons/s}\ . \tag{3.52}$$

With $r_p = 100\ \mu$, $\ell = 5$ cm, $n_i = 10^{26}\ m^{-3}$, and a pulse length $\tau = 50$ ns, the total number of neutrons (Fig. 3.17) produced at 500 eV is less than 10^6, however, and with any practical solid angle, this is below the sensitivity of a time-integrating detector.

In principle, the most valuable temperature diagnostic for an HDZP plasma is based on observations of bremsstrahlung emission. In time-resolved measurements, the soft x-rays (100 eV-10 keV) produced by free-free collisions between electrons and ions pass through thin metallic foil energy filters and are absorbed in an organic scintillator which produces visible photons.[25,26] These photons are detected by a high gain photomultiplier tube, and the signal is recorded on a fast oscilloscope. In the most common diagnostic configuration, two identical scintillator-photomultiplier systems are employed; after relative responsivity calibration with the same metallic foil, additional foils may be interposed in front of one scintillator. On a given plasma discharge, the ratio of x-ray transmission for two different thickness foils uniquely determines the electron temperature for a true Maxwellian electron distribution. The use of an array of scintillator-photomultipliers constitutes a measurement of spectral emission profile but is often a physical impossibility because of limited diagnostic access to the plasma chamber. The metallic foils are essentially high pass filters above a characteristic energy edge, and they shield the sensitive photomultiplier from the high flux of visible emission associated with the plasma discharge. Often, the foils are also vacuum seals isolating the plasma chamber from the scintillator-photomultiplier combination. The organic scintillators used are typically NE102 or Pilot B, plastics which contain wavelength shifters that produce a light output spectrum sharply peaked at 423 nm or 408 nm. The plastic conversion efficiency, defined as photons out per eV of absorbed x-ray energy, is found to be a function of the x-ray energy

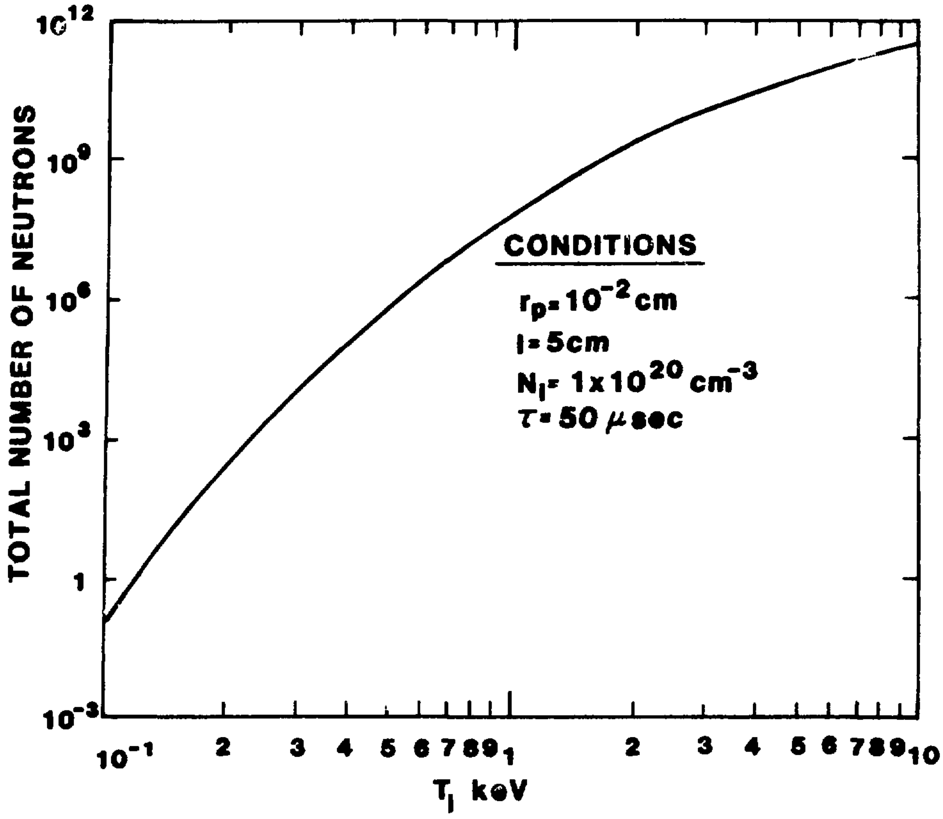

Fig. 3.17 Neutron yield for typical HDZP conditions

itself,[27,28] with approximately 1 photon out per keV absorbed for a 3 keV x-ray. A computer program has been developed to predict the ratio of signal intensities for different foils as a function of electron temperature. The code convolves the bremsstrahlung spectrum for a given temperature plasma of specified density, volume, and solid angle with the absorption associated with a particular material and thickness foil. In addition, the program calculates the absorption resulting from the intervening H_2 gas. This net x-ray flux is then converted to a visible photon flux using the absorption and conversion efficiency of the scintillator. Finally, using the manufacturer-supplied photocathode sensitivity and the tube gain, the program yields a prediction for the total photomultiplier anode current.[29] In practice, the construction of an x-ray diagnostic requires careful attention to the problems of vacuum and light leaks, electrical noise, and photomultiplier space charge and leakage current effects. In addition, the requirement of high speed (~ 3 ns) time resolution necessitates the use of fast scintillators and photomultipliers. A further complication involves spatial localization of the x-ray emission; the electrodes in the plasma chamber are a potential source of anomalous x-rays which can lead to an erroneous interpretation of the data. One localization scheme which has been implemented (Fig. 3.18) incorporates a collimator or telescope which eliminates the electrodes from the scintillator field-of-view. The collimator is simply a pair of vertically displaced slits in 1/2" thick brass plate which block x-rays from all but the central 3 cm of the 5 cm long plasma. The top slit of the telescope is vacuum sealed with a metallic foil (typically Al) which also acts as a reference filter and light seal. Foils which are thinner than 0.5 mil do not have sufficient strength to withstand the pressure differential during pumpout of the chamber. For a 1.0 mil Al reference foil, we have calculated the ratio of signal intensities for the two detectors with a variety of additional absorbers (Fig. 3.19). The relatively weak dependence of this ratio on plasma temperature in the range

$$200 \text{ eV} < T_e < 800 \text{ eV} \tag{3.53}$$

illustrates the difficulty in obtaining accurate temperature measurements using this diagnostic. Two identical, fast (1.8 ns decay constant), Pilot B scintillators are placed side-by-side above the foil, and the scintillator

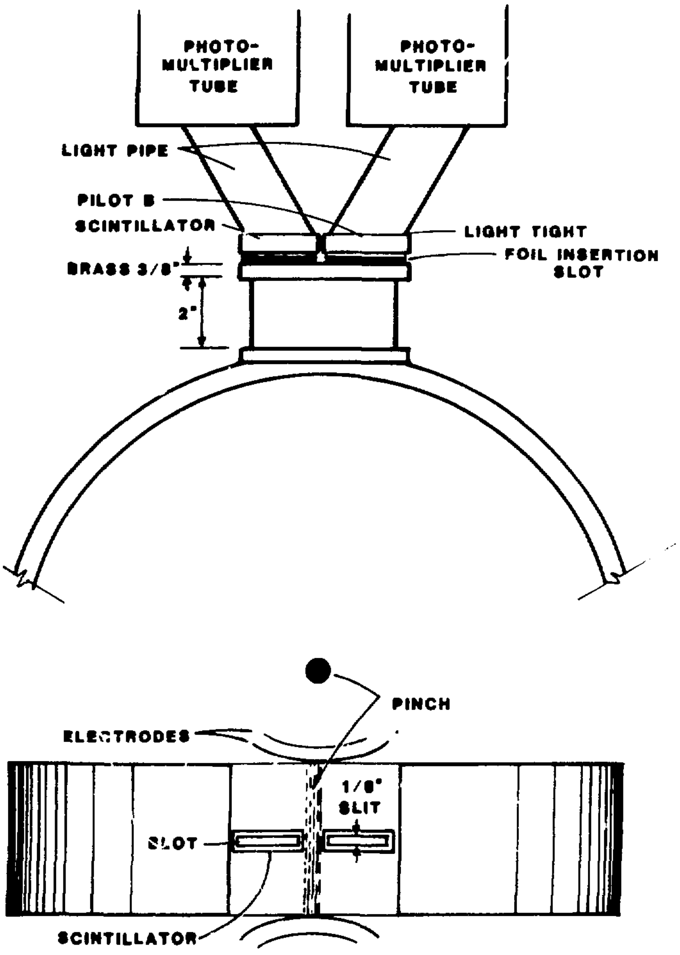

Fig. 3.18 Two-foil x-ray absorption diagnostic

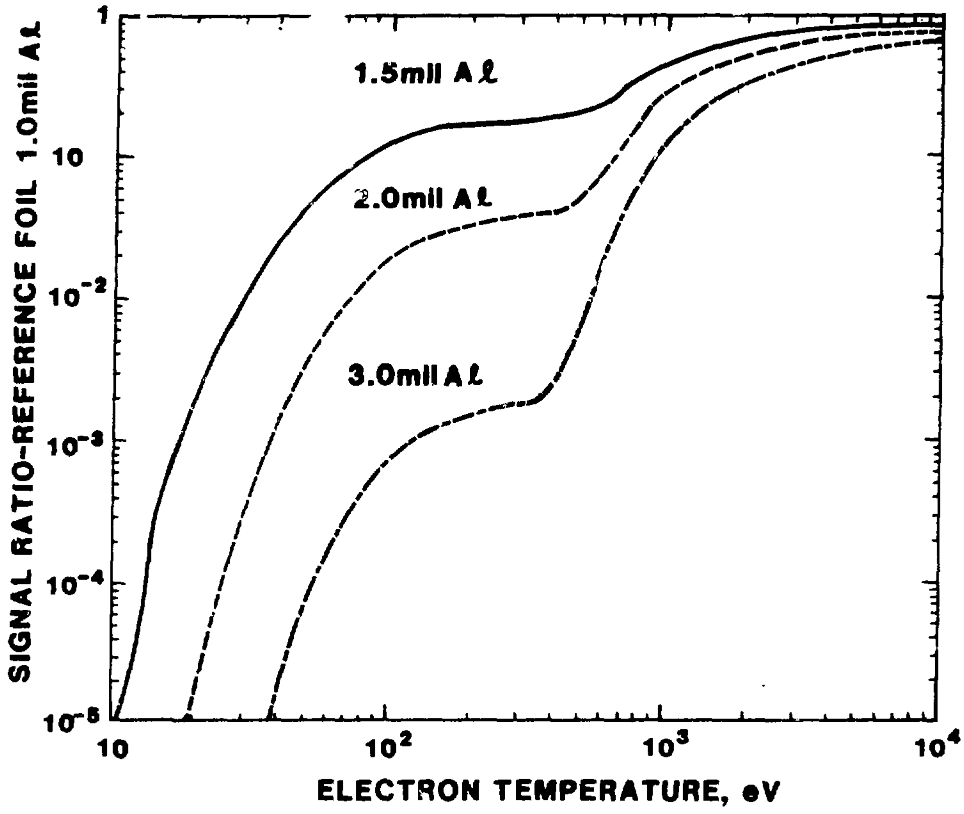

Fig. 3.19 Computed transmission ratios for various aluminum foils

output photons are coupled to bundles of 1 mm^2 light fibers. Each bundle contains 75 fibers and is in turn optically coupled through silicon grease to an RCA 8575 2" diam bialkali 116 response photomultiplier tube. The tubes are operated with the photocathode at negative high voltage (-2000 Vdc) to avoid the need for coupling capacitors at the anode; feedthrough capacitors would severely limit the signal rise time because of their stray inductance. The high voltage photocathode surface must be protected from grounded surfaces or even insulators capable of providing picoampere leakage currents which would upset the field. The 8575 photomultiplier was chosen for its low dark current and partially conducting dynode supports, which help eliminate charge-up inside the multiplying structure. The tube is, however, susceptable to afterpulsing by ion bombardment of the photocathode.[30] These afterpulses typically occur 200-350 ns after the main pulse and must be distinguished from the actual x-ray signal. Linearity of the tube response is measured using light-emitting diodes and Wratten neutral density filters. The photomultipliers are carefully double shielded by copper pipe, and the 50 Ω coaxial cables from the anodes are terminated at the oscilloscopes <u>and</u> at the tube bases to prevent reflections. Additional foils may be added to either system and are placed between the vacuum seal foil and the scintillators. Light-emitting diodes are used to establish timing information for the photomultiplier signals and support manufacturer-supplied information on propagation delay for a given applied voltage. Cable lengths are critical parameters in determining overall relative timing for nanosecond experiments and are carefully noted to avoid confusion.

3.6 Initiation Laser

The initiation of the plasma channel is provided by a laser pulse which enters the load chamber through a 1/4" diameter hole in the ground electrode. In the standard configuration, the exit high voltage aluminum electrode contains a large cavity with a 1/4" diameter entrance hole (Fig. 3.20). This cavity is an effective dump for the laser light and eliminates effects resulting from the interaction of the H_2 gas with 1) reflected light or 2) ultra-violet radiation generated during laser bombardment of the electrode surface. All of the aluminum electrodes contain heavy metal elkanite inserts which survive the discharges relatively undamaged. A brass electrode with annular grooves and pickoff leads similar to the mating flange current detectors is often used on the ground side of the chamber to crudely diagnose the region of current flow.

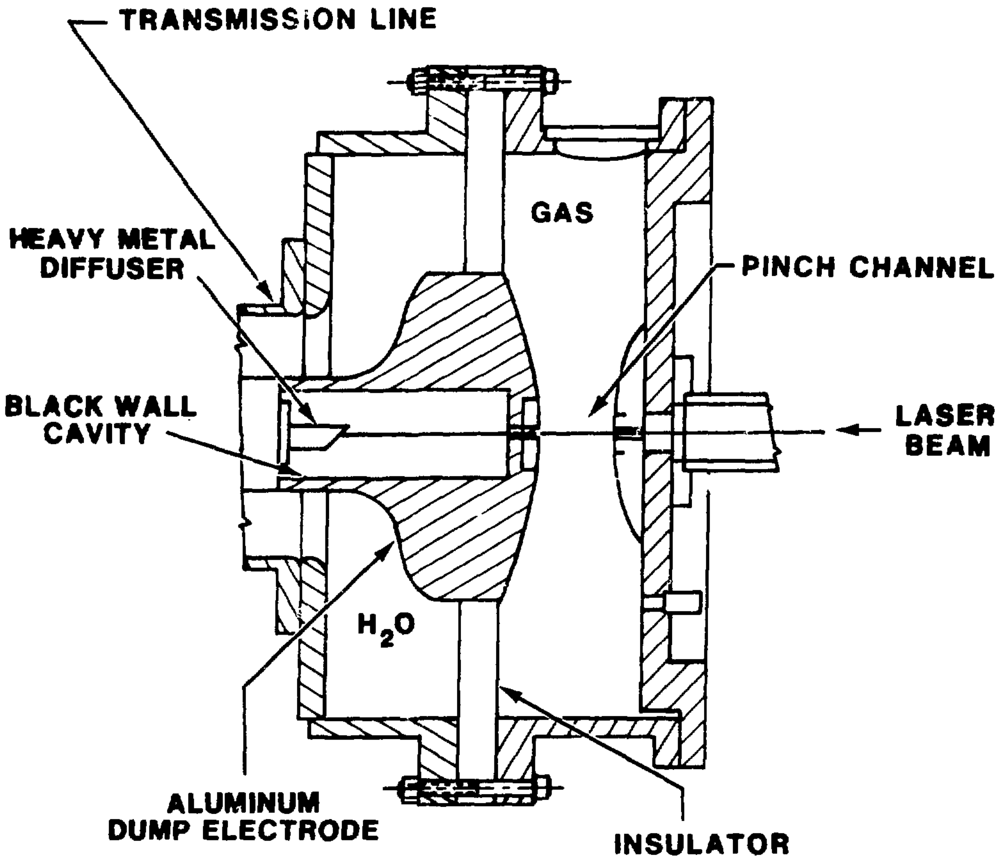

Fig. 3.20 Load chamber modification illustrating dump electrode

The plasma chamber entrance port is sealed with a high quality glass window mounted at Brewster's angle to reduce reflections of the polarized laser beam, and the window is located sufficiently far from the focus to withstand the power loading. Present operation of the prototype HDZP uses a ruby laser at 6943 Å because of its availability and high power. The laser is an oscillator-amplifier combination (Holobeam 800) capable of producing a maximum energy of 8 joules in the giant pulse mode. The oscillator is Q-switched using a KD*P Pockels cell and produces a pulse with FWHM of 30 ns. The amplifier output is typically focused through a weak (60 cm focal length) lens into the center of the load chamber, and the laser is triggered between 20 ns and 300 ns before application of high voltage across the gap by the Marx generator-transmission line circuit. The maximum output power of the laser, with the 60 cm focal length lens, is sufficient to generate optical breakdown in 1 atmosphere of H_2 gas as evidenced by Schlieren photographs of the focal region. This asymmetry is undesirable because it results in nonuniform channels, and the laser is operated below the breakdown threshold. The oscillator is a flat-flat resonator with either an output mirror or longitudinal mode-selecting etalon available, and pinholes are used in the cavity to produce single transverse mode pulses if desired.

In normal operation, the laser requires 60 seconds cooling and recharge time between shots; if the load chamber is not flushed and refilled, the system repetition rate is one shot per minute. To date, over 6000 shots have been recorded, attesting to the simplicity and reliability of operation. For personnel safety, the entire experimental apparatus is enclosed in an interlocked blast wall area.

References for Chapter 3

1. J. E. Hammel, W. C. Nunnally, and D. B. Thomson, Bull. Am. Phys. Soc. 23, 847 (1978).

2. J. E. Hammel, F. C. Jahoda, J. Shlachter, and D. A. Platts, Bull. Am. Phys. Soc. 24, 1078 (1979).

3. J. S. Shlachter and J. E. Hammel, Bull. Am. Phys. Soc. 25, 923 (1980).

4. J. E. Hammel, Los Alamos Scientific Laboratory report LA-6203-MS, (1976).

5. R. A. Fitch, IEEE Transactions on Nuclear Science NS-18, 190 (1971).

6. W. C. Nunnally, C. A. Ekdahl, J. E. Hammel, K. W. Hanks, and L. A. Jones, Los Alamos Scientific Laboratory report LA-UR-78-1692, (1978).

7. W. C. Nunnally, Los Alamos Scientific Laboratory report LA-UR-78-2150, (1978); see also D. A. Platts, 3rd IEEE International Pulsed Power Conference, unpublished (1981).

8. J. C. Martin, Dielectric Strength Notes, No. 1, AWRE, unpublished (1970).

9. D. H. McDaniel, Sandia National Laboratory, personal communication, 1979.

10. W. C. Nunnally, L. A. Jones, and S. Singer, Los Alamos Scientific Laboratory report LA-UR-79-1436 (1979).

11. C. A. Ekdahl, R.S.I. 51, 1645 (1980).

12. W. A. Edson and G. N. Oetzel, R.S.I. 52, 604 (1981).

13. E. E. Bergmann, R.S.I. 48, 545 (1977).

14. J. L. Lachambre and Z. Szili, Appl. Opt. 18, 425 (1979).

15. E. E. Bergmann, Appl. Phys. Lett. 31, 661 (1977).

16. F. C. Jahoda and G. A. Sawyer, in Methods of Experimental Physics, edited by H. R. Griem and R. H. Lovberg (Academic Press, New York, 1970), Vol. 9, part B, Chapter 11.

17. J. S. Shlachter, J. E. Hammel, F. C. Jahoda, and D. A. Platts, Bull. Am. Phys. Soc. 25, 700 (1980).

18. G. Oster and Y. Nishijima, Sci. Am. 208, #5, 54 (1963).

19. J. Guild, The Interference Systems of Crossed Diffraction Gratings, (Oxford University Press, Oxford, 1956).

20. F. C. Jahoda and G. A. Sawyer, loc. cit.

21. M. Raleigh and J. R. Greig, NRL Memorandum report 4390 (1981).

22. A. W. DeSilva and G. C. Goldenbaum, in Methods of Experimental Physics, edited by H. R. Griem and R. H. Lovberg (Academic Press, New York, 1970), Vol. 9, part A, Chapter 3.

23. L. J. Suter, Lawrence Livermore National Laboratory, personal communication, 1978.

24. C. A. Ekdahl, Los Alamos Scientific Laboratory report LA-UR-79-815 (1979).

25. F. C. Jahoda, E. M. Little, W. E. Quinn, G. A. Sawyer, and T. F. Stratton, Phys. Rev. 119, 843 (1960).

26. R. C. Elton, NRL report 6738 (1968).

27. P. B. Lyons and D. W. Lier, IEEE Transactions on Nuclear Science NS-22, 88 (1975).

28. P. B. Lyons, D. W. Lier, R. H. Day, and T. L. Elsberry, Los Alamos Scientific Laboratory report LA-UR-76-189 (1976).

29. C. A. Ekdahl, Los Alamos National Laboratory, personal communication, 1980.

30. F. T. Kuchnir and F. J. Lynch, IEEE Transactions on Nuclear Science NS-15, 107 (1968).

Chapter 4. Experimental Results

The diagnostics described in Chapter 3 have been used to investigate the behavior of the plasma produced in the prototype HDZP experiment. Pinhole Schlieren photographs indicate that the refraction region is initially uniform, less than 300 μ in radius, and one-dimensional. Approximately 50 ns after current begins to flow in the load, the photographs suggest that a helical structure is present. The majority of the observations documented in this chapter are restricted to the early plasma phase.

The prototype machine has been operated in two distinct modes, "shorted switch" and "switch operative," characterized by the state of the self-breaking water switch. Sections 4.1 and 4.2 contain qualitative descriptions of the plasma formed in each mode, with an emphasis on the ruby initiation laser requirements for the formation of an apparently isolated and well defined column. In section 4.3, the data from both the quantitative Moiré-Schlieren diagnostic and the scintillator-photomultiplier diagnostic are discussed. The results underscore the importance of accretion processes in an HDZP plasma; the measured line density increases at a non-negligible rate. A discrepancy between the x-ray signals and the measured line density is noted for the switch operative mode. The final section describes a non-localized current model which can explain these observations. This model is indirectly supported by calculations, additional experiments, and the results of a two-dimensional MHD code.

4.1 Shorted Switch Mode

The "shorted switch" configuration effectively couples the plasma load directly to the Marx bank output inductance, limiting $(dI/dt)_{ave}$ to approximately 8×10^{11} As^{-1}. Preliminary observations of the channel consisted of pinhole Schlieren photographs in N_2 laser light and signals from current and voltage probes in the water transmission line. To facilitate global MHD computer modeling of the plasma dynamics, the voltage across the electrodes at which current begins to flow (V_{break}) must be known. While the true breakdown process cannot be adequately represented by a single parameter, we find only minor variations in the code results with changes in V_{break}. A capacitive coupled voltage probe installed in the insulator separating the load chamber from the water transmission line provides a direct measurement of this quantity. For conditions which will subsequently be referred to as "standard operation," namely a fill pressure of 11 psia H_2 and erected Marx bank voltage of 396 kV, we find that

$$V_{break} \simeq 150 \text{ kV} \tag{4.1}$$

for the shorted switch mode. In Figs. 4.1 and 4.2 the predicted voltage and current waveforms are presented along with probe data from a representative machine shot. After an early (~ 5 ns) resistive phase, one expects the plasma load characteristics to resemble those of an ideal inductor, independent of the channel dynamics, and the agreement between experiment and theory in these figures is not necessarily indicative of accurate modeling. Pinhole Schlieren photographs of the plasma taken within 40 ns of t_o, the onset of current flow, reveal a uniform, axisymmetric, narrow (100-300 μ diam) channel (Fig. 4.3) formed along the path of the ruby initiation laser. The laser is typically fired 100 ns before the arrival of the voltage wave from the Marx, and as the optical pulse is only 30 ns FWHM, the gas does not act under the simultaneous influence of both electric fields. While the laser is operated below the threshold for optical breakdown, the Marx bank voltage alone is sufficient to cause gas breakdown between the electrodes, for standard operating conditions. Pinhole Schlieren photographs of this "bulk breakdown" for shots without a ruby laser pulse display a full field of parallel filamentary structures, each presumably carrying a fraction of the total load current (Fig. 4.4). Schlieren photography of these fine-scale (10 μ diam) structures provides a refractive view of objects normally observed in their own visible emission using fast framing or streak techniques, and suggests a unique method to study breakdown processes, offering excellent spatial and temporal resolution.

Under standard conditions, pinhole Schlieren photographs of the laser-initiated channel taken more than 40 ns after t_o display a complex, multi-dimensional structure (Fig. 4.5). The structure remains within a straight but expanding well-defined boundary as the current continues to rise. Photographs taken at peak current (~ 90 kA, t_o + 150 ns) show the same complex, straight structure, with a boundary of approximately 3 mm. The expansion rate

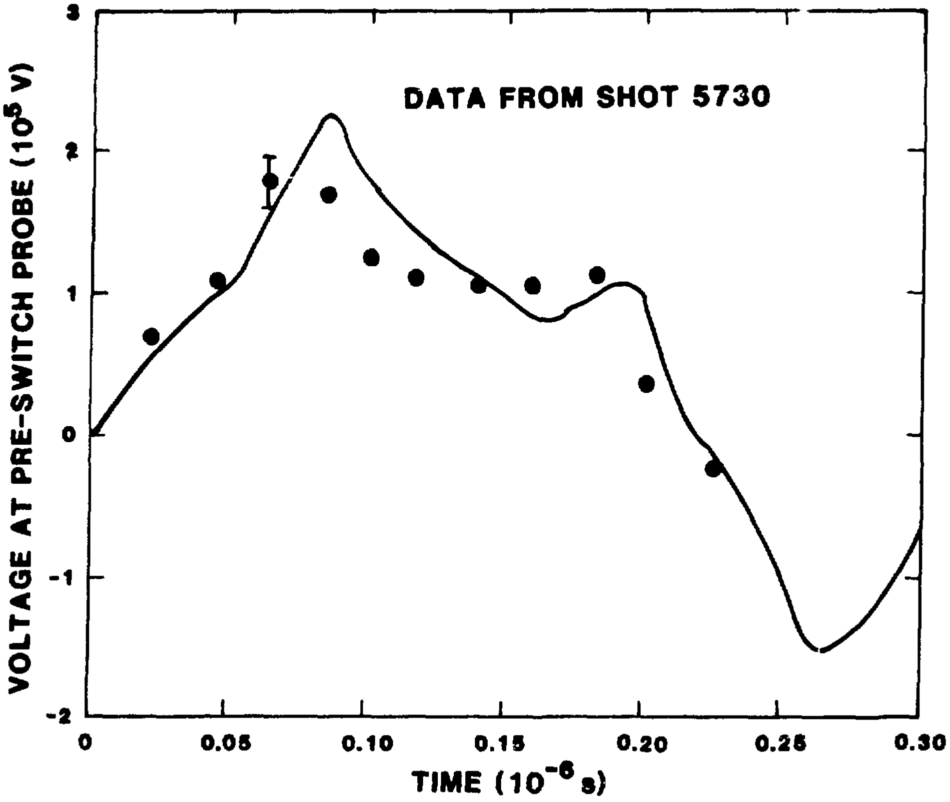

Fig. 4.1 Voltage waveforms for shorted switch mode, global MHD predictions and experimental observations

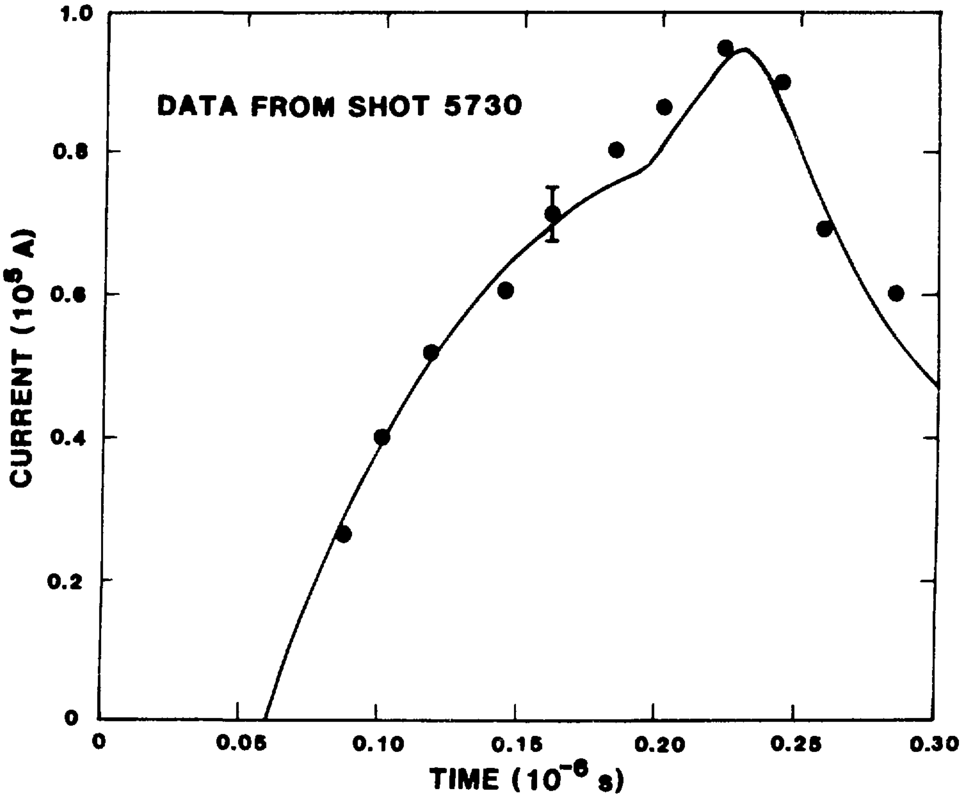

Fig. 4.2 Current waveforms for shorted switch mode, global MHD predictions and experimental observations

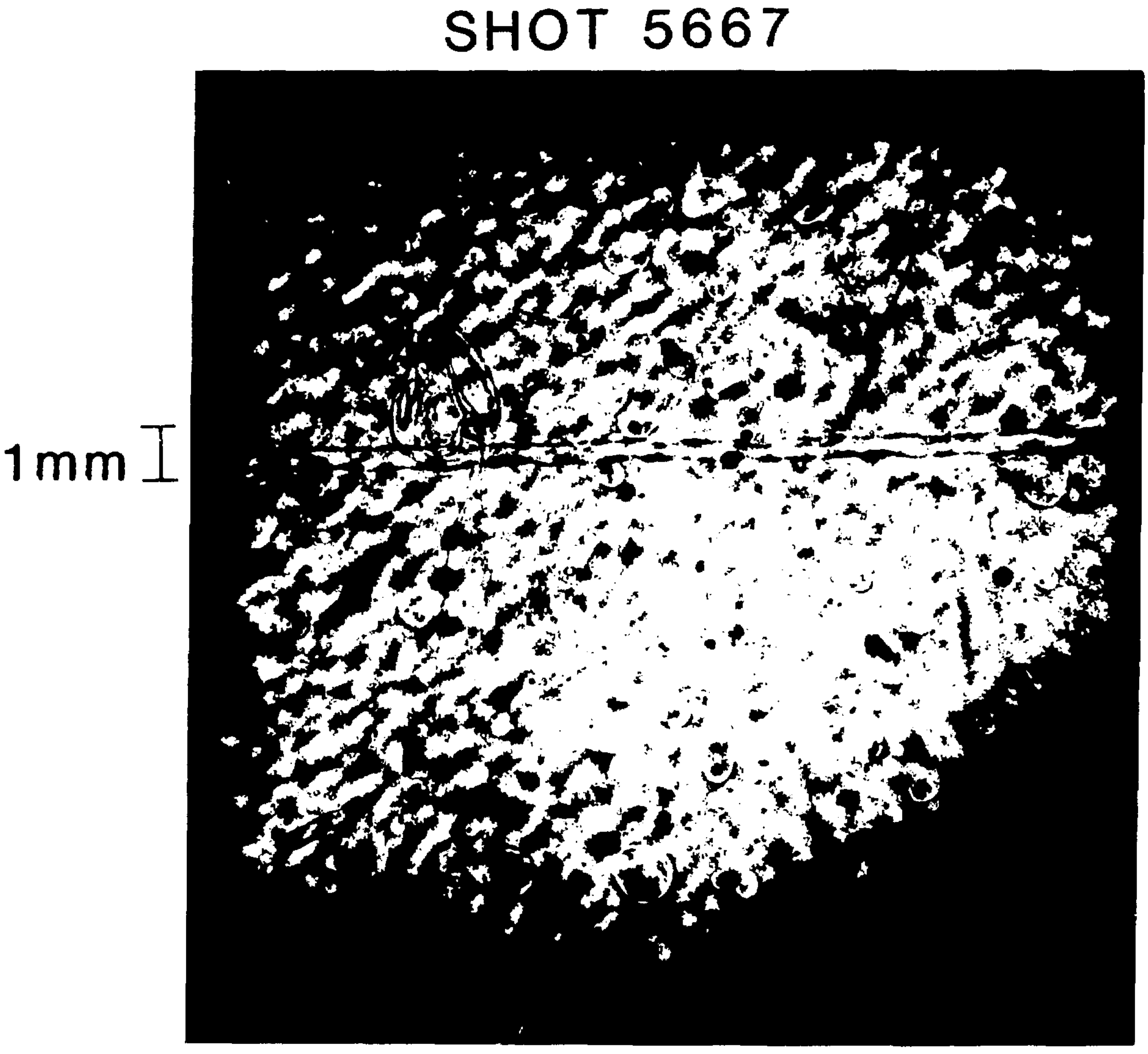

Fig. 4.3 Early pinhole-Schlieren photograph of plasma column for shorted switch mode

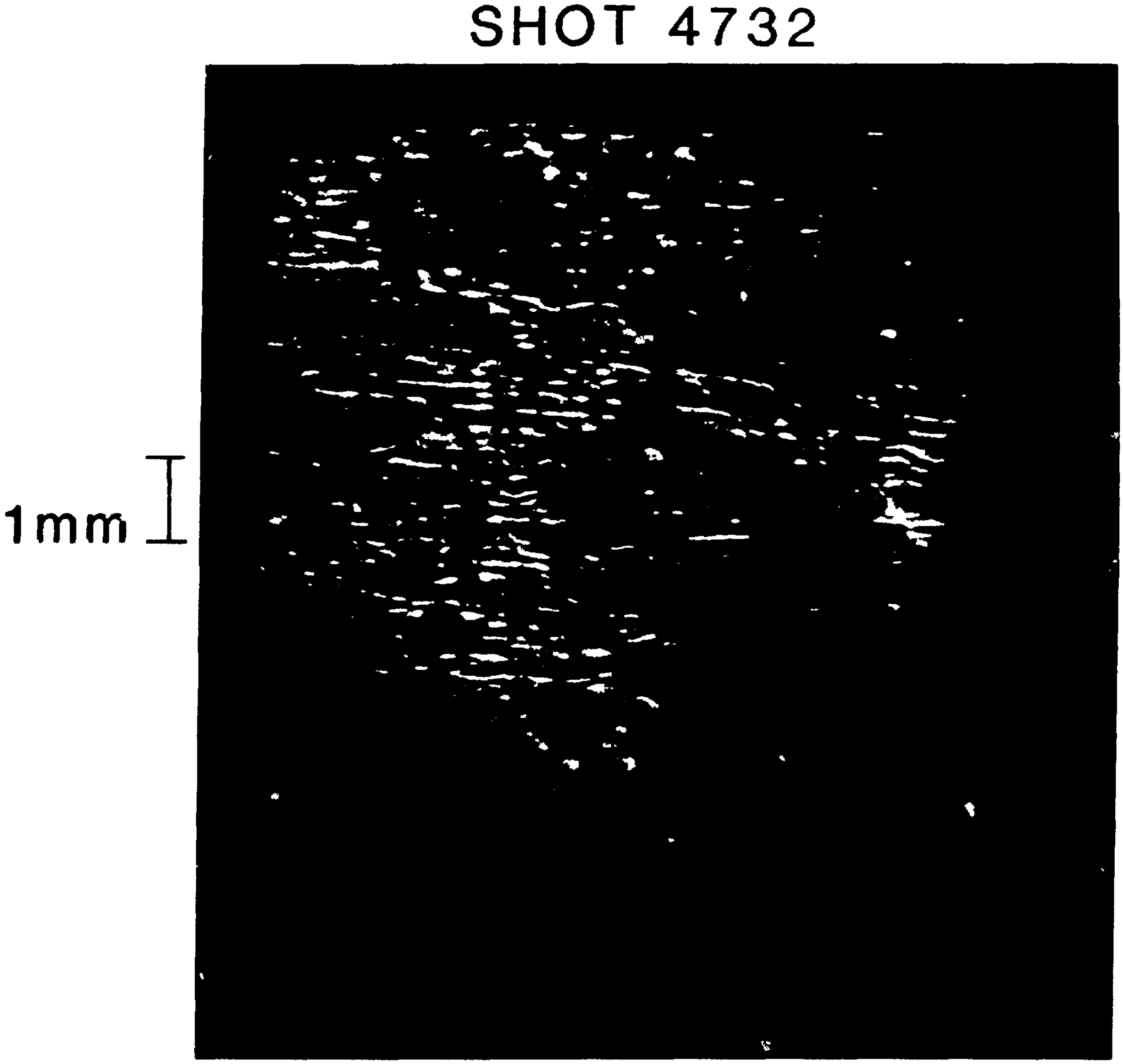

Fig. 4.4 Filamentary structures associated with bulk breakdown

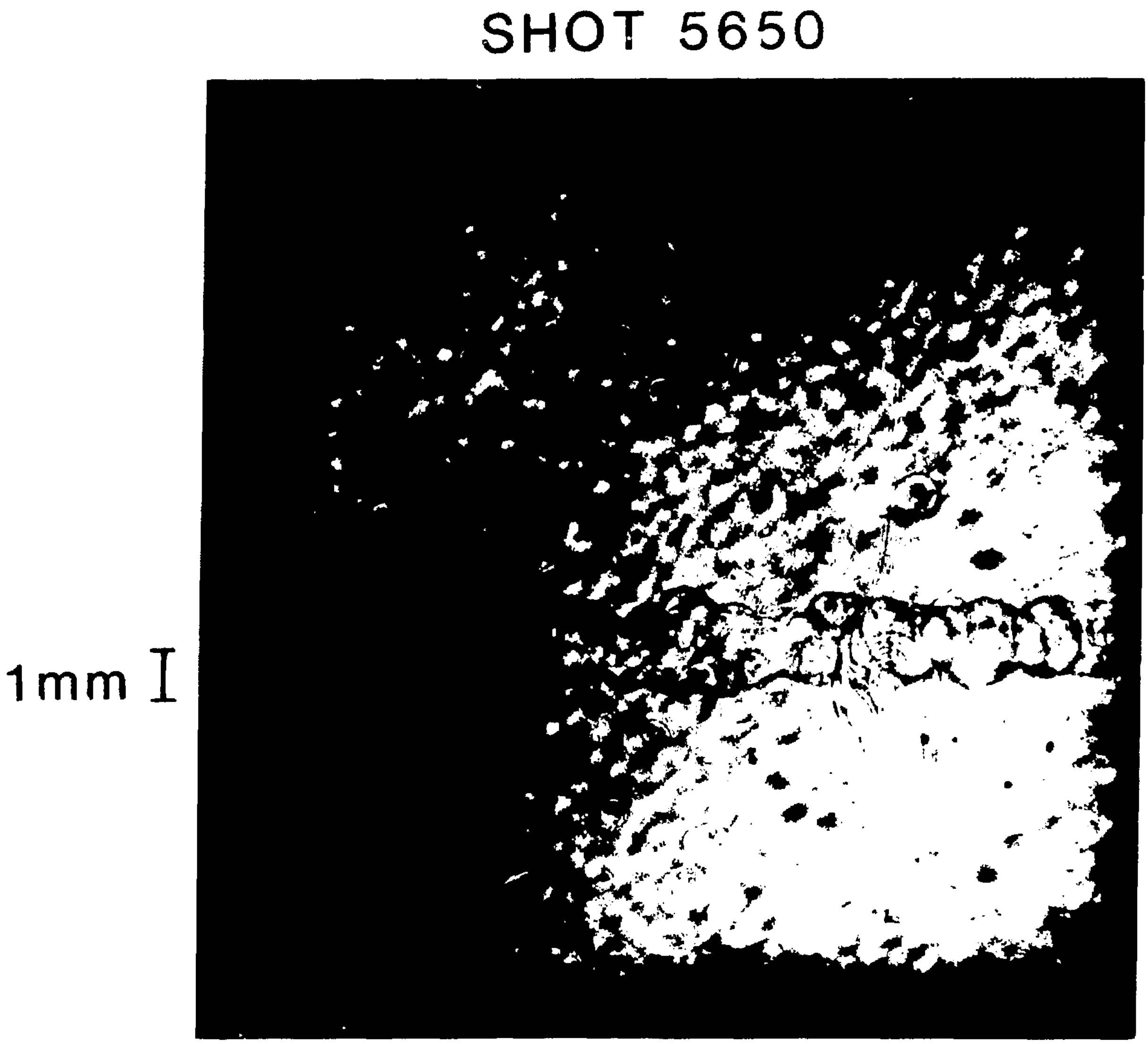

Fig. 4.5 Pinhole Schlieren photograph of three-dimensional structure

of the boundary envelope is nearly constant over the full rise of current (Fig. 4.6), with

$$v_{\text{boundary}} \approx 2\times10^4 \text{ ms}^{-1} \tag{4.2}$$

determined on a shot-to-shot basis. To guarantee that the observed structure was three-dimensional, the N_2 laser diagnostic beam was split into two components, and pinhole Schlieren photographs were taken simultaneously from two transverse directions separated by 90^0. Figure 4.7 is representative of these wide stereo views, and while it is nearly impossible to identify most individual features of the refractive structure in both photographs, three-dimensionality is clearly established.

Speculation on the nature of this structure leads to the hypothesis that the plasma channel winds up into a helix with a characteristic instability growth time of ~ 40 ns. Simple energy considerations, in particular, suggest that an initially linear current system will evolve into a helical structure. For a purely inductive plasma load, the stored field energy, E, is expressed by

$$E = \frac{LI^2}{2} = \frac{\Phi^2}{2L} \tag{4.3}$$

where Φ is the magnetic flux, LI, and L is the inductance. For a plasma which is a good conductor, we can consider the flux to be trapped, and thus constant. Therefore to minimize its energy, the plasma will act to maximize its inductance, i.e., form a helix. Experimental and theoretical work[1] on reversed field pinch systems supports this simple picture, as do observations of $m = 1$ helical instabilities in classical Z-pinches. To investigate the possibility of an inductance rise correlated with a helical onset, detailed voltage and current measurements were obtained, along with early ($t \sim t_0 + 10$ ns) pinhole Schlieren photographs used to establish the initial inductance. Using the expression

$$V_{\text{Load}} = \frac{d}{dt}(LI) \tag{4.4}$$

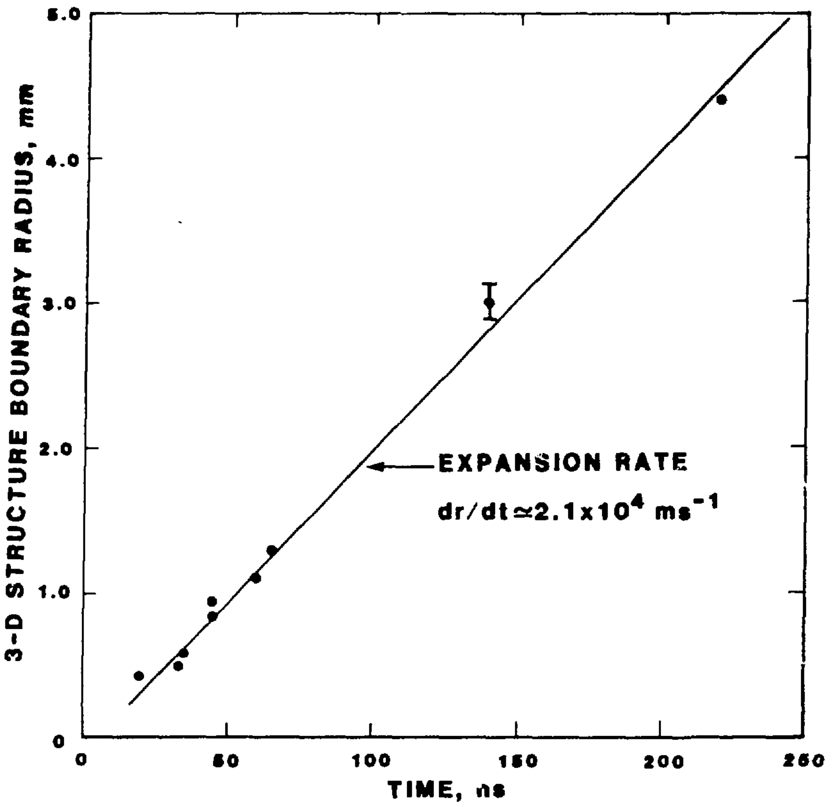

Fig. 4.6 Boundary envelope expansion rate

TEST OBJECT 0.0625 INCH DIAMETER ROD WITH REFERENCE POINT

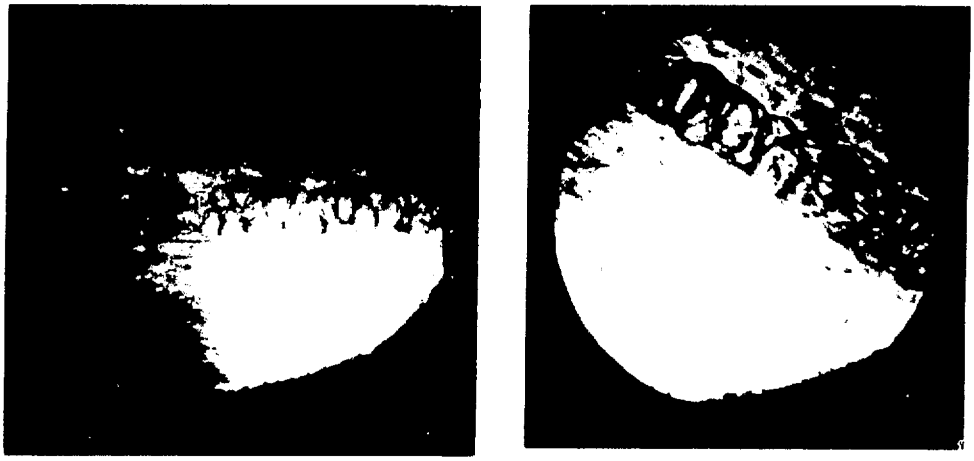

SHOT 2644

Fig. 4.7 Stereo (90°) pinhole-Schlieren photographs we compute an inferred inductance from

$$L(t) = \frac{\int_{t_1}^{t} V(\tau)d\tau + L(t_1)I(t_1)}{I(t)} \qquad (4.5)$$

where t_1 is the time at which a one-dimensional uniform channel is photographed. Figure 4.8 is a plot of L(t) showing an overall increase in inductance but no abrupt change at t = 40 ns. One difficulty with this analysis is that resistive effects are ignored in Eqs. (4.4) and (4.5). It is clear that one cannot experimentally distinguish between a resistance and a time-varying inductance from current and voltage traces alone. We note, however, that the observed channel expansion alone would suggest a decrease in overall inductance, perhaps masking the increase one expects from a helical structure.

The beam split N_2 laser diagnostic which resulted in 90^0 views of the plasma was modified to estimate the growth time of three-dimensional structuring. For these experiments, one beam was delayed by time-of-flight using a relay mirror; two Schlieren photographs were then taken, separated by 8 ns. With proper laser triggering, data were obtained for which the "main" beam photograph shows a one-dimensional channel while the "delayed" beam photograph indicates a three-dimensional structure (Fig. 4.9). This is consistent with an Alfvên transit time, if the ions have a temperature given by

$$T_{ION} \gtrsim 15 \text{ eV} \qquad (4.6)$$

from Eq. (1.4).

To detect the axial field, B_z, which might be associated with a helix, a magnetic probe measurement was attempted. A single turn, 2.54 cm radius loop centered in the axial midplane was designed to encircle the plasma and detect residual solenoidal return flux. The loop consists of a string of 10 series resistors, each 22 Ω, with two light emitting diodes of opposite bias in a parallel configuration (Fig. 4.10). Voltages induced in the loop, proportional to $\dot{B}$, result in currents through the diodes, which are nearly linear devices (Fairchild FLV-104A) converting current to light. Fiber optics are used to

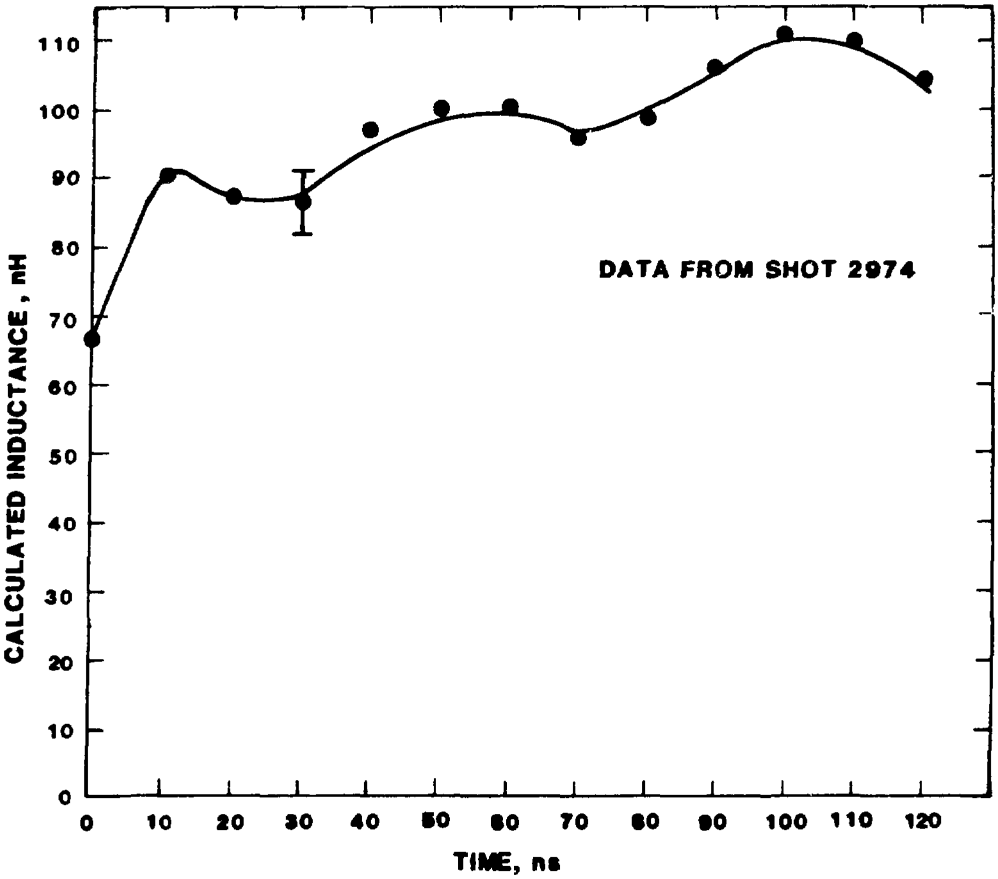

Fig. 4.8 Calculated inductance from current and voltage data

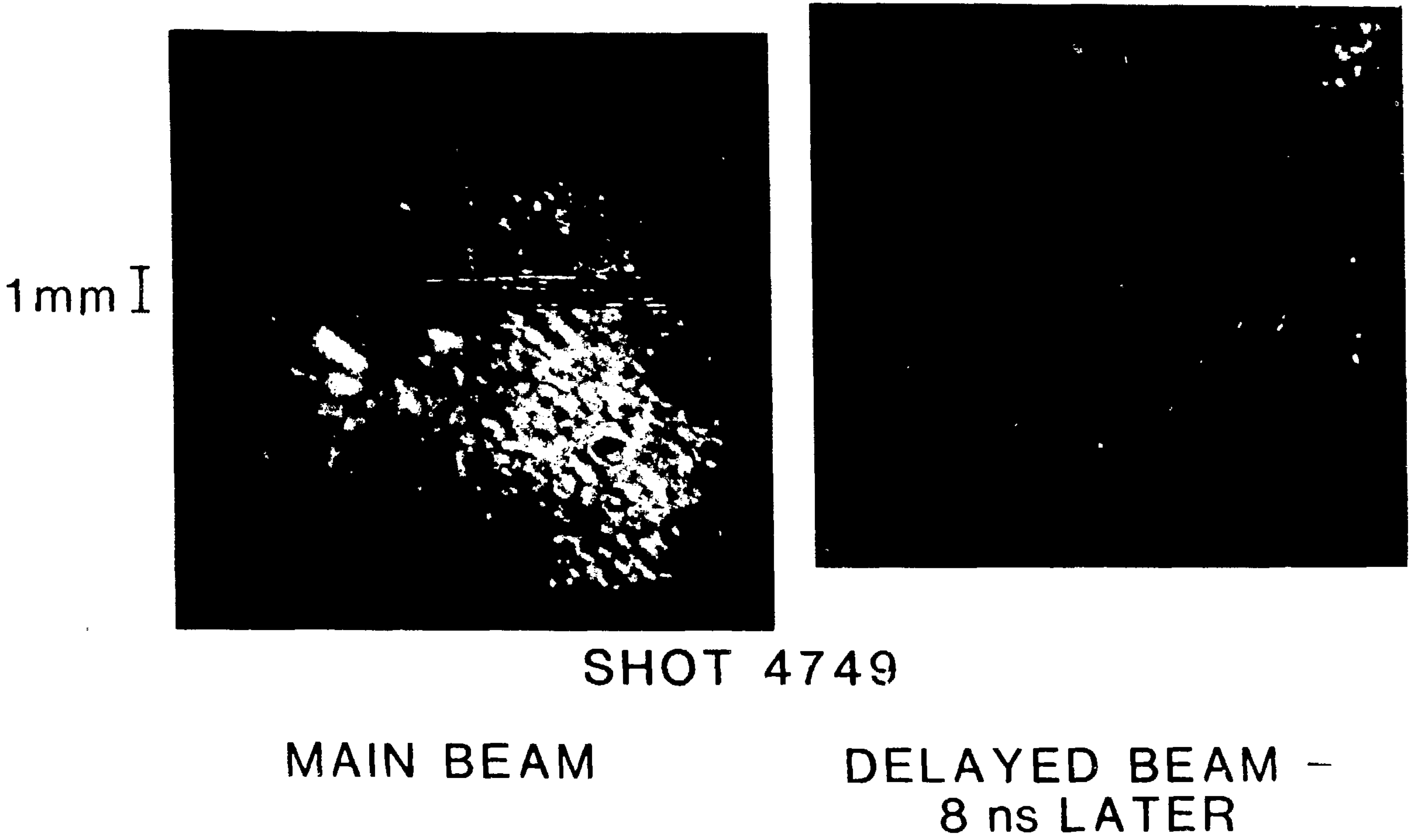

Fig. 4.9 Beam-split pinhole-Schlieren photographs illustrating transition from 1-D to 3-D structure

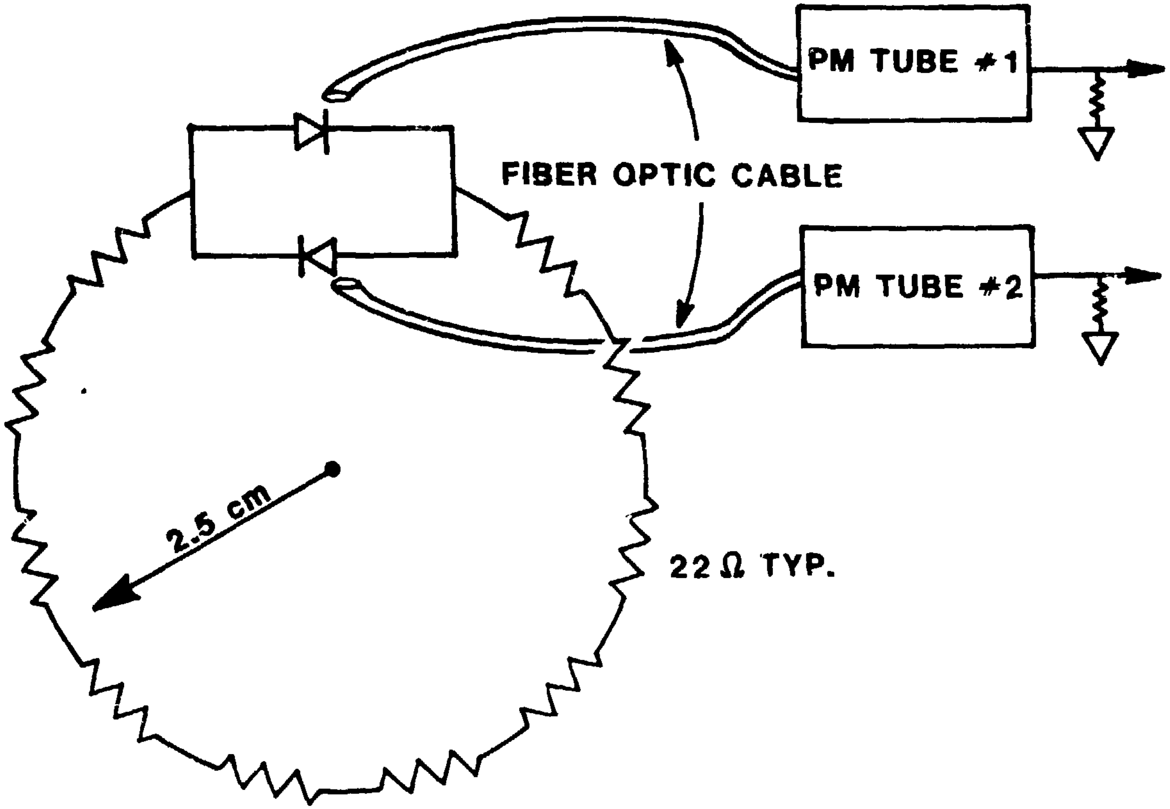

Fig. 4.10 Axial field diagnostic

extract the light out of the chamber to RCA 1P-28 photomultipliers in the screen room, one for each diode, thereby eliminating the problem of high voltage insulation associated with direct probe measurements using coaxial cables. On several shots, there has been evidence for a delay between the onset of plasma current and the onset of a signal from one of the LEDs, possibly attributable to the time before formation of a helical structure. Additional evidence for a helical configuration comes from an examination of the data from two consecutive shots (Fig. 4.11); the signals from the two diodes appear to have reversed roles, suggesting a reversal of helicity between shots. Unfortunately, the presence of a large B_θ field in the vicinity of the probe complicates this interpretation; a slightly skewed misalignment of the loop with respect to the plasma column will allow both components of the field to register a signal, and B_θ will be indistinguishable from B_z.

In the preceding discussion we have assumed that the three dimensional structures observed at late times ($t > 40$ ns) were correlated with electron density perturbations of the refractive index. The Moiré-Schlieren diagnostic, which can establish the nature of the refraction region, has indicated that the uniform structure seen in the early, axisymmetric plasma phase is associated with electron refractivity. We have been unable to distinguish between electron and neutral shock refraction once axisymmetry is lost, however, because of large refraction, lens imperfections, minor focusing errors, or improper laser beam quality; i.e., the Moiré fringes cannot be followed. The three-dimensional structure observed in pinhole Schlieren photographs might in fact be a hydrodynamic phenomenon at a surface well outside the plasma and not indicative of MHD effects in the main channel. The nature of this complex structure is an issue which has not yet been resolved.

A number of experiments have been conducted to establish the ruby initiation laser requirements for the creation of a single, narrow (100 μ) channel unaccompanied by bulk breakdown filaments. For the shorted switch operation with standard conditions of pressure and Marx voltage, a number of effects have been observed, although quantitative data is difficult to obtain as a result of wide shot-to-shot variations. These variations are not understood and may be caused by spatial and temporal changes in the ruby laser output.

The output pulse energy from the ruby laser is measured with a Scientech surface absorbing disc calorimeter (36-0001) and controlled by both the amplifier and oscillator flash lamp voltages. Single channel Schlieren

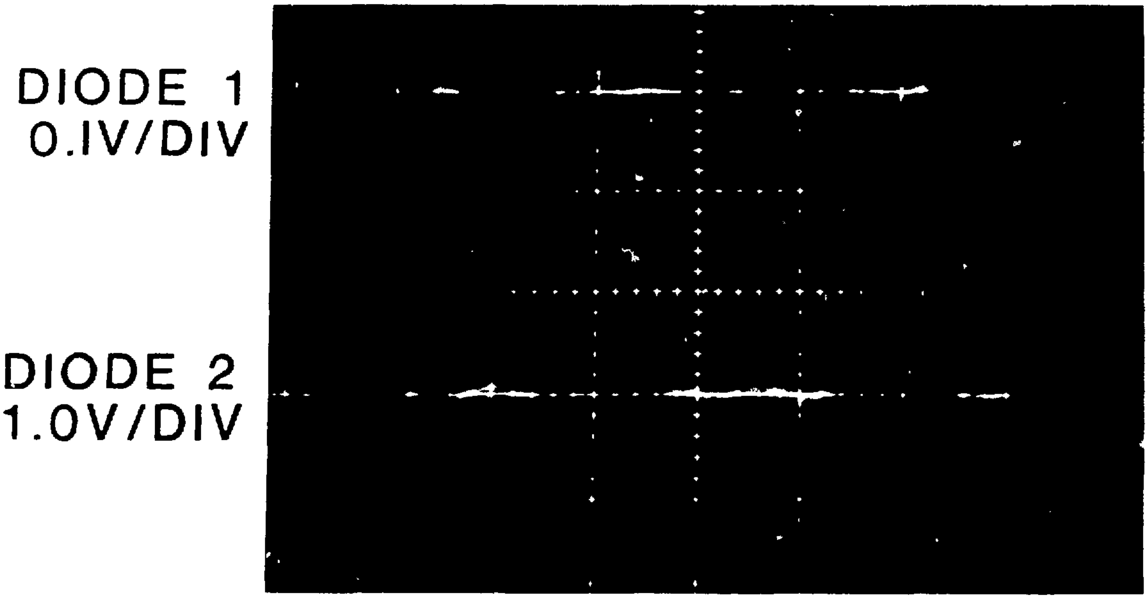

SHOT 3241

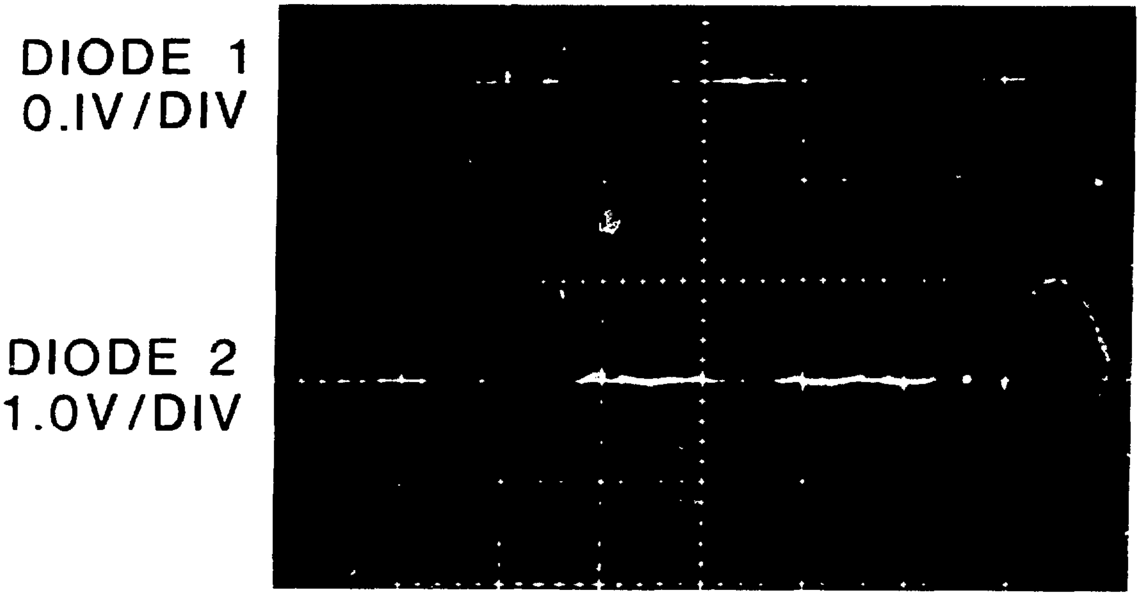

SHOT 3242

100 ns/DIV

Fig. 4.11 Successive machine shot data from axial field diagnostic photographs showing no evidence of colinear filamentary breakdown structures have been obtained for

$$\sim 0.01\ \mathrm{J} < E_{\mathrm{laser}} < 6\ \mathrm{J} \quad , \tag{4.7}$$

where the smallest energy pulses are produced by firing the oscillator beam through an unpumped, and therefore absorbing, amplifier rod. Laser pulse energies exceeding 6 J create optical breakdown plasmas under standard conditions and are avoided.

To determine the effect of the laser focal spot location on the channel formation, the lens position was varied by ± 5 cm from the nominal position, which places the beam focus midway between the two chamber electrodes. Over this range, with a laser pulse energy of 2 J, no filamentary structures were observed, and the initiated channel remained unchanged in appearance.

The laser angular divergence can be controlled by spatial filtering (transverse mode selection) within the oscillator cavity and has been measured with both a linear charge coupled device array (Reticon G-256) and a wedge-multiple burn spot technique. For the values

$$1\ \mathrm{mrad} < \alpha < 5\ \mathrm{mrad} \tag{4.8}$$

we have not seen evidence of bulk breakdown filaments in pinhole Schlieren photographs. These observations suggest that the channel initiation process has a relatively weak dependence on the laser parameters, for the shorted switch mode of operation.

4.2 Switch Operative Mode

The HDZP "switch operative" mode produces substantially higher voltages and current rise rates than those observed under "shorted switch" conditions. For standard conditions (11 psia, 396 kV Marx) we observe

$$V_{\mathrm{break}} \approx 200\ \mathrm{kV}\ \text{and}\ \frac{dI}{dt} \approx 5\times10^{12}\ \mathrm{As}^{-1} \quad . \tag{4.9}$$

A numerical model for the self-breaking water switch, based on recent experiments at Sandia National Laboratory,[2] is given in Fig. 2.5c, and it is used to obtain the global MHD code predictions for current and voltage waveforms (Figs. 4.12 and 4.13). As in the shorted switch mode, the agreement with experiment is to be expected for even the simplest constant inductance load model. The original motivation for the use of a self-breaking water switch is illustrated in Fig. 4.14, which compares the observed current waveforms for the two experimental modes with that of a Hammel equilibrium curve[3] for a channel with 100 μ radius and a density corresponding to 11 psia fill pressure.

Pinhole Schlieren photographs taken under "switch operative" conditions indicate a strong correlation between ruby initiation laser parameters and the presence or absence of filamentary breakdown structures parallel to the central channel. We have found that operation of the ruby laser in the range

$$2\ \mathrm{J} < E_{laser} < 6\ \mathrm{J} \tag{4.10}$$

is required to produce a channel without filamentary background structures. The increase in the minimum laser energy for the "switch operative" mode, Eqs. (4.7) and (4.10), is undoubtedly related to the increased electric field across the gap under these conditions. The strong dependence of the filaments on laser energy made it impossible to vary the ruby laser divergence in the switched mode because any spatial filtering decreased E_{laser} below 2 J, and all experiments were conducted with α = 5 mrad.

The position of the laser focal spot between the chamber electrodes was also found to have a substantial effect on the apparent breakdown character seen in the pinhole Schlieren photographs. The nominal lens position is established by exceeding the threshold for optical breakdown and determining the location of the resultant detonation wave using the N_2 laser Schlieren diagnostic; the Marx bank is not operated during these tests. For shots with the ruby focal spot more than 1 cm away from the axial electrode midplane, the laser initiated channel is accompanied by filamentary structures, depicted in Fig. 4.15.

In addition to affecting the region of peak laser electric field, changes in the lens position also modify the interaction of the ruby light with the high voltage electrode surface. The original electrode "dump" was a tapered hole with a 1/4 inch diameter entrance aperture, and several pinhole Schlieren

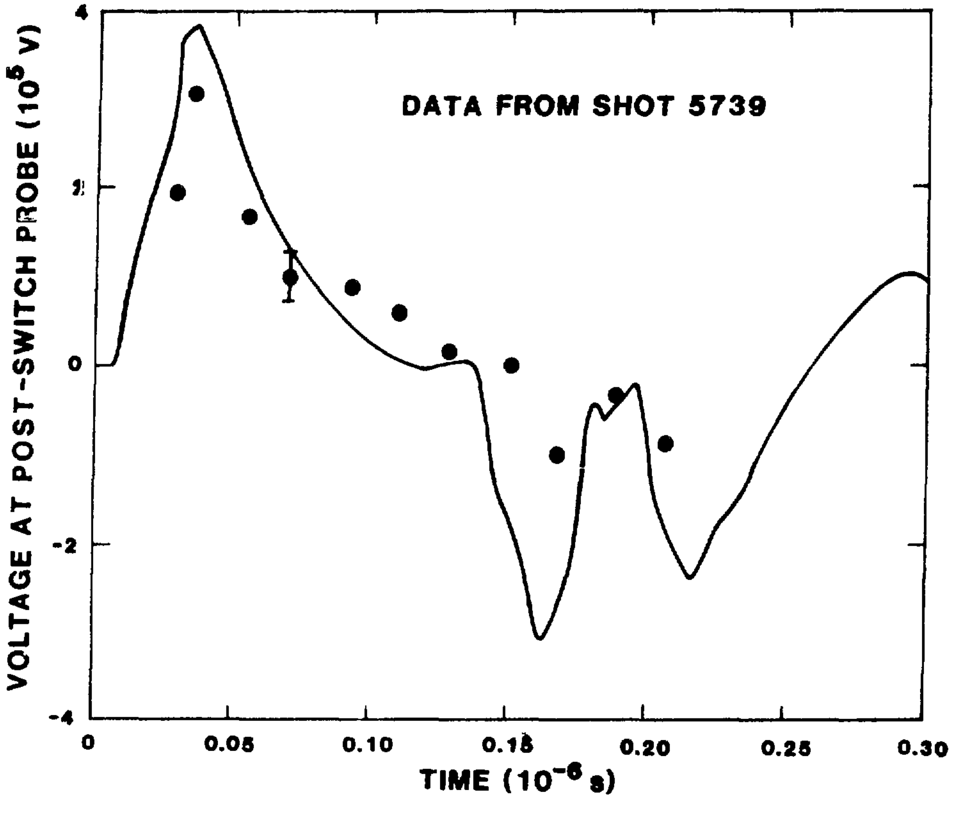

Fig. 4.12 Voltage waveforms for switch operative mode, global MHD predictions and experimental observations

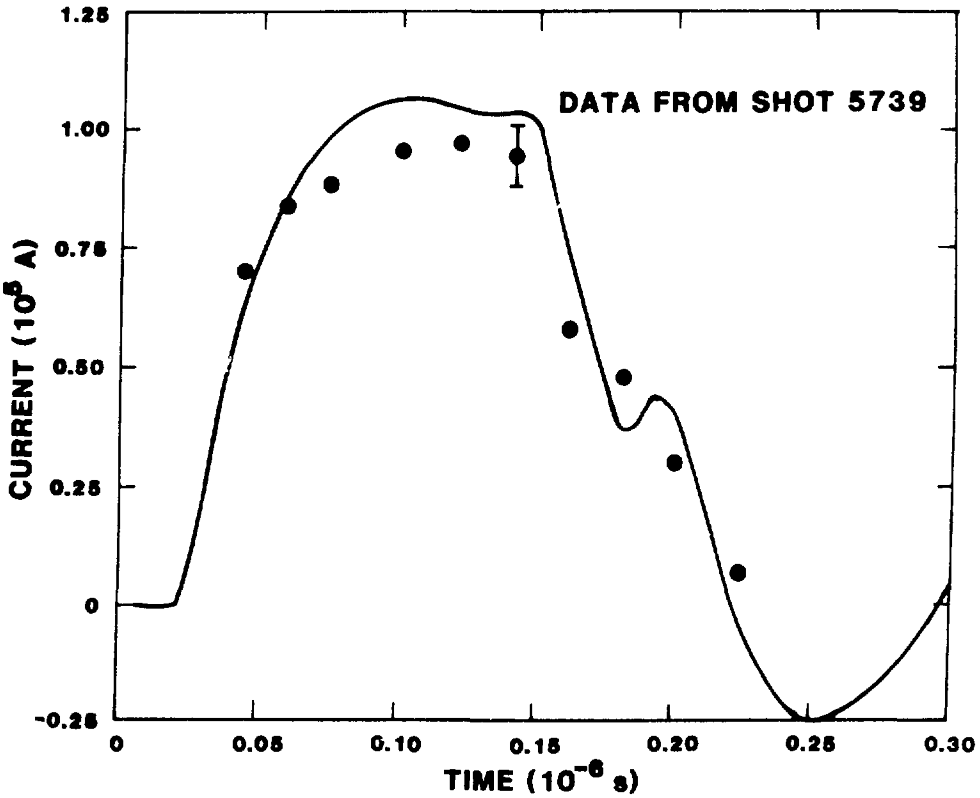

Fig. 4.13 Current waveforms for switch operative mode, global MHD predictions and experimental observations

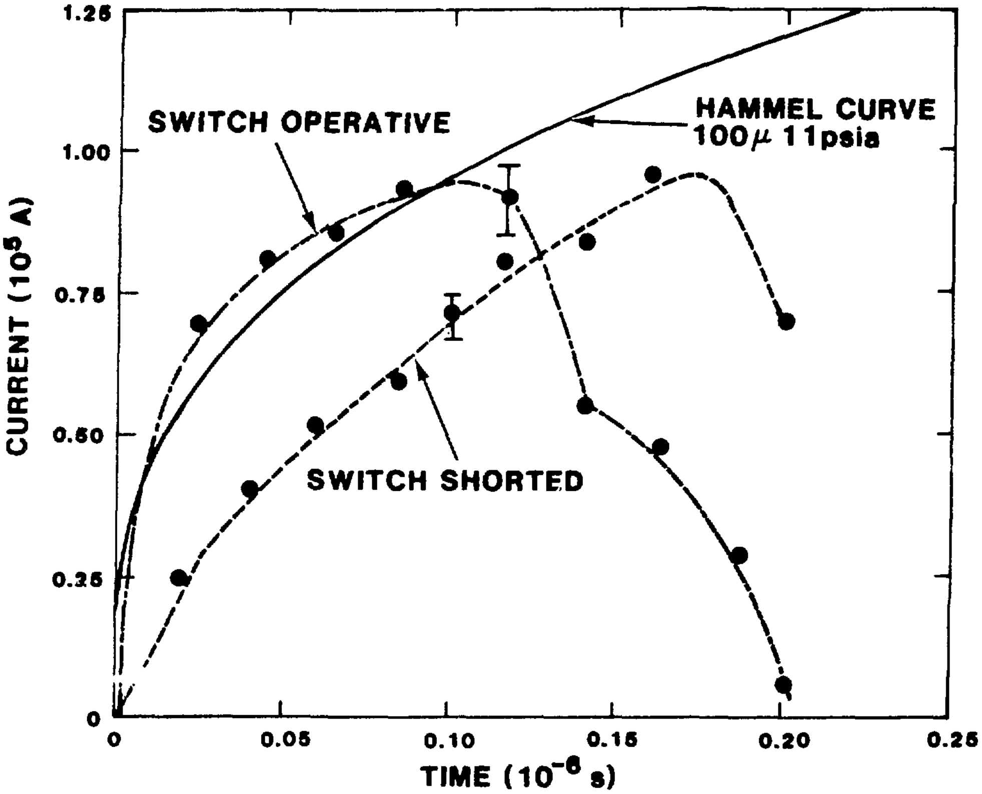

Fig. 4.14 Hammel equilibrium curve and current waveforms for shorted switch and switch operative modes

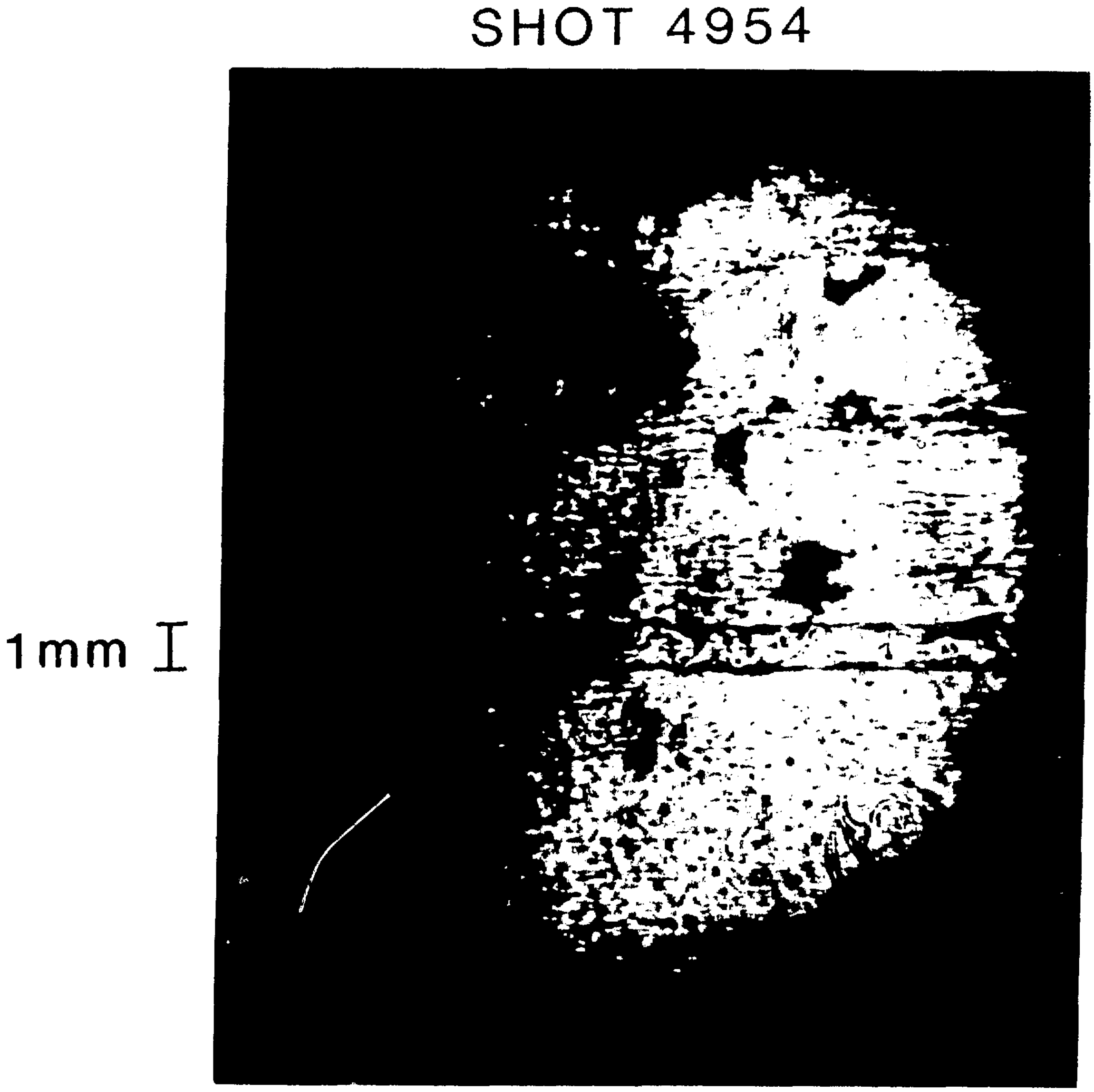

Fig. 4.15 Pinhole Schlieren photograph of laser-initiated channel accompanied by filamentary structures

photographs displayed a boundary to the region containing filaments which was almost certainly a projection of the taper angle. These data support the conjecture that some filaments are caused by the ruby laser itself, either directly by reflected light interactions or through gas illumination by ultra-violet emission from a laser-generated metal plasma at the electrode surface. An improved dump (Fig. 3.19) was constructed to eliminate stray ruby light, and tapered boundaries to the filament region were not subsequently observed.

Further observations of the breakdown phase reveal the complexity of the initiation process. In a simple experiment, the focusing lens was removed entirely, allowing the raw laser output beam to be apertured by the 1/4 inch diameter entrance hole in the ground electrode. As expected from the resultant low laser electric field, pinhole Schlieren photographs indicated a region filled with filamentary structures. These filaments did not fill the entire field of view, however, but were restricted to the cylindrical volume illuminated by the laser (Fig. 4.16). In a set of experiments designed to investigate the competition between the laser and Marx bank generated electric fields, the ruby initiation beam was aligned to enter the chamber at 15^{0} with respect to the nominal axis, and the resultant channel was clearly formed along the laser path. In a further study of the initiation process, an aluminum plug was inserted in the dump hole, with a sharp point protruding beyond the electrode surface. Schlieren photographs of the breakdown without the ruby laser pulse typically displayed two or three channels eminating from the plug tip. When the laser was fired before the Marx bank generated voltage was applied across the gap, however, a single channel was formed along the beam path, for standard conditions; the presence of the sharp point did not disturb the initiation.

Without firing the Marx bank, we are unable to detect any direct interaction between the ruby laser and the neutral gas below the optical breakdown threshold using the refractive diagnostics. This sensitivity limitation prevents us from distinguishing between two possible explanations of the laser initiation process. In the first of these hypotheses, the laser creates a weakly ionized channel, and the seed electrons avalanche in the subsequent applied electric field. The second[4] concentrates on the heating of the neutral gas by the small fraction of laser energy which is absorbed. The heated region expands, reducing its neutral pressure and increasing the

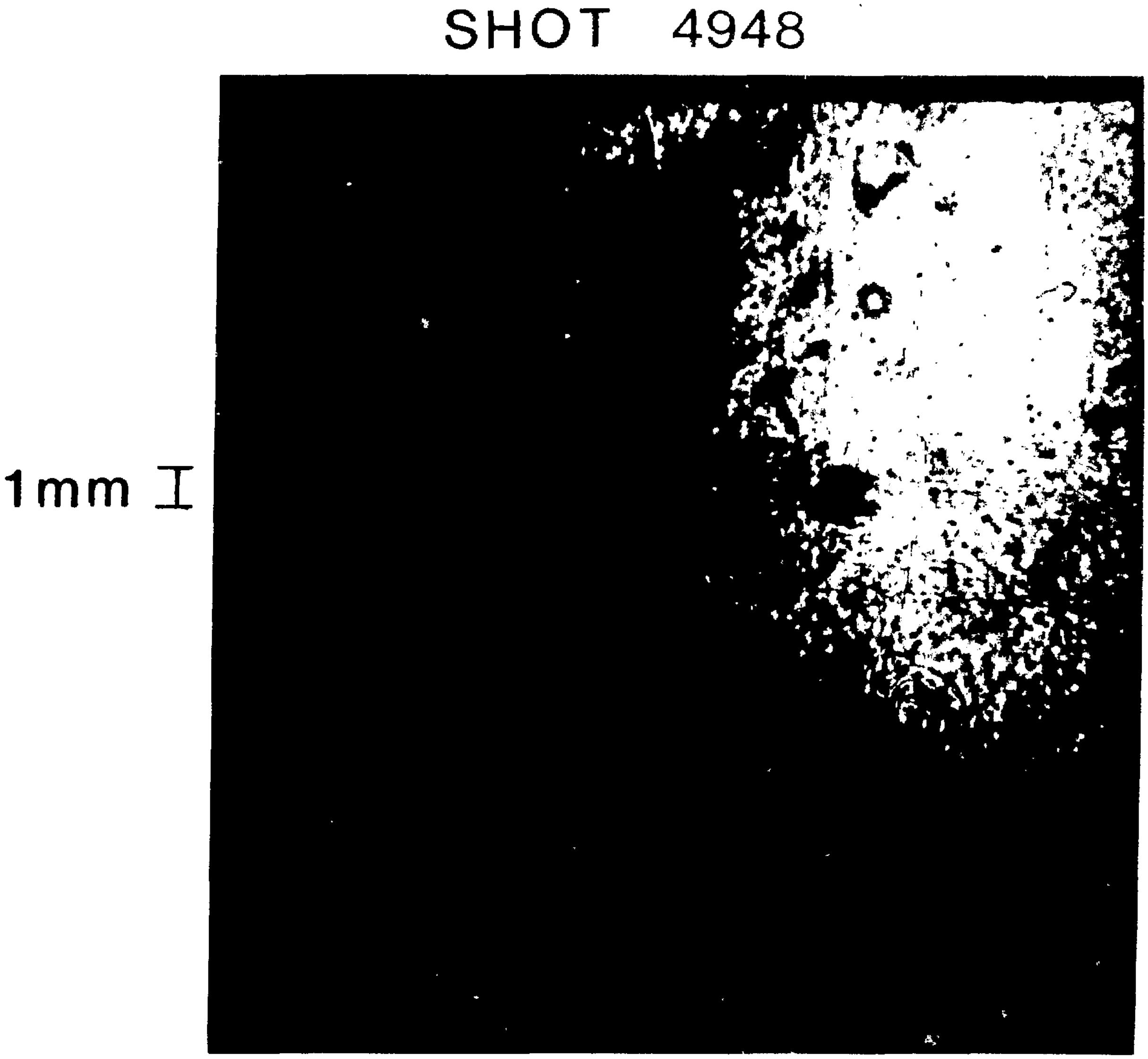

Fig. 4.16 Filamentary structures bounded by 1/4" aperture of raw ruby laser beam

effective field stress (E/P) when the voltage is applied across the gap. This region then preferentially breaks down and conducts the load current. Future experiments with more sensitive refractive diagnostics must be used to determine which mechanism is operating in the prototype HDZP.

Pinhole Schlieren photographs taken under switch operative conditions which display a central column without filamentary background are obtained routinely with nominal lens position and ruby laser pulse energies above 2 J. The qualitative features of these laser-initiated channels are identical to those described previously for shorted switch mode operation. During the first 40 ns, the columns are straight, axisymmetric, and have characteristic radii of 100-400 μ (Fig. 4.17) while later photographs again display three-dimensional structures.

4.3 X-ray and Optical Diagnostic Results

Both the two-foil differential absorber x-ray diagnostic (Fig. 3.18) and quantitative optical diagnostics have been used extensively to investigate the behavior of laser-initiated channels in the shorted switch and switch operative modes. The data in this section are restricted to shots which do <u>not</u> display filamentary structures. In addition, the data plotted in Figs. 4.21-4.36 are all representative of the early, axisymmetric plasma phase, determined by the Moiré and interferometer photographs.

For the majority of shots in the shorted switch configuration, the photomultiplier signals consist of narrow (30 ns FWHM) spikes occurring at or near peak voltage on the capacitive probe trace for the monitor located 8 ns behind the chamber. No signals are observed at peak current, 150 ns later. Shot-to-shot reproducibility of the x-ray signals is poor, and we have been unable to determine an effective two-foil temperature for the shorted switch mode signals. To eliminate the possibility that these signals were caused by stray light, a thick (1/4 in.) glass absorber was placed between the scintillator and the foil, with the subsequent attenuation of the photomultiplier output. The x-ray signals are also absent when a 1/4 in. thick brass absorber is inserted above the aluminum foil, establishing that the x-rays are not highly energetic (> 100 keV).

For switch operative conditions, the time and energy characteristics of the x-rays remain unchanged, while the amplitudes of the spikes are increased by one or two orders of magnitude. An example of the photomultiplier signals for a

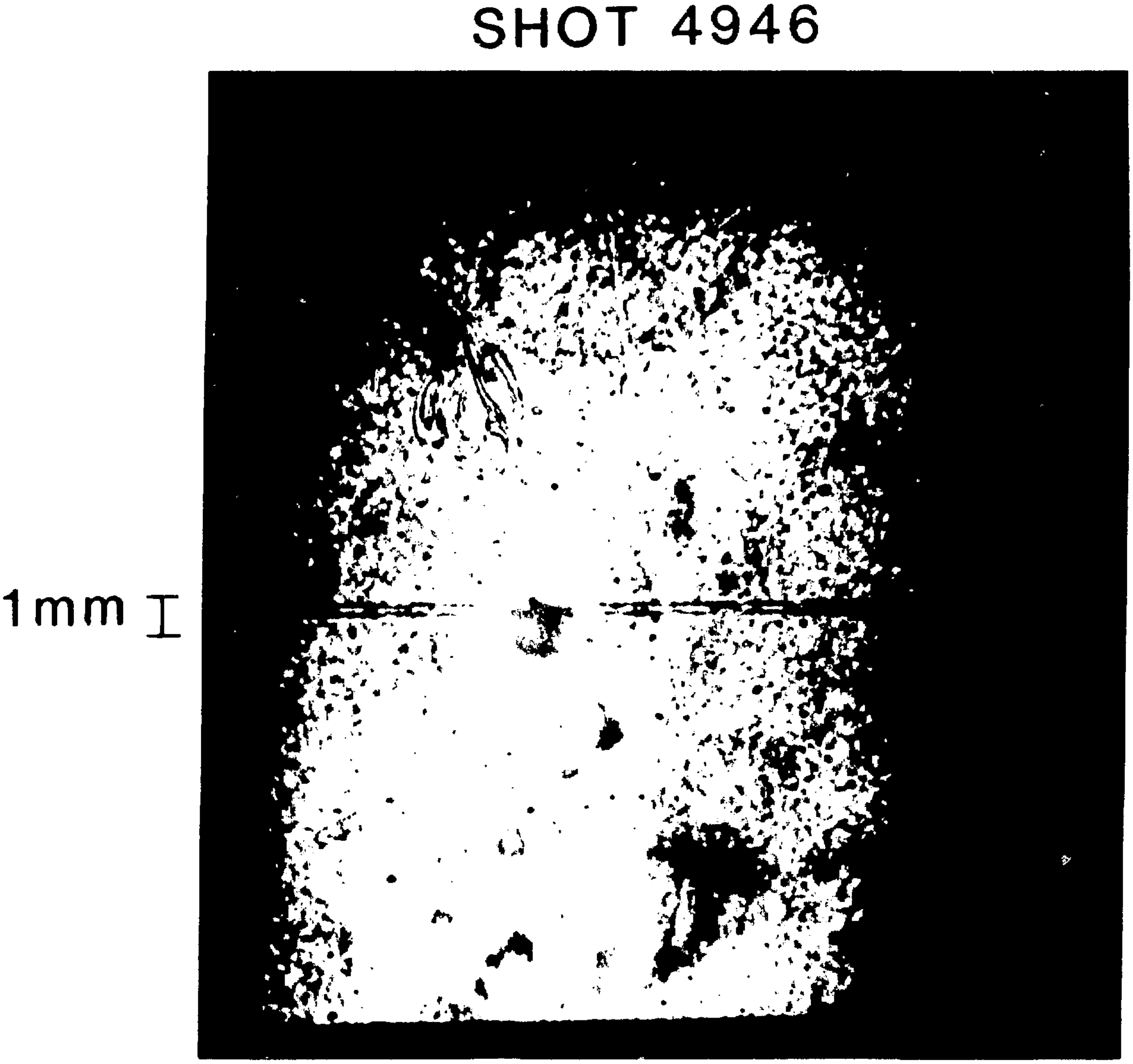

Fig. 4.17 Early pinhole Schlieren photograph for switch operative mode

switch operative shot along with the accompanying current and voltage traces is shown in Fig. 4.18. The shot-to-shot variation is again large, but two-foil temperatures for the spikes can be determined with

$$200\ \text{eV} \lesssim T_{2\text{-foil}} \lesssim 1000\ \text{eV} \quad . \tag{4.11}$$

The Moiré-Schlieren diagnostic has been used to determine the channel radius, the electron density distribution, n(r), and the line density, N. Fig. 4.19 shows a typical Moiré-Schlieren photograph along with the computed density profile. To support these measurements, a Mach-Zehnder interferometer was constructed using the N_2 laser, and with proper care given to the equalization of path lengths and optical surface quality, high contrast interference fringes were produced. The interferometric data are unfolded with a simple Abel inversion technique, and a sample photograph with the resultant density profile is shown in Fig. 4.20.

The global MHD code has been run for the conditions of the prototype HDZP experiment in both the shorted switch and switch operative modes. This model predicts an initial rapid expansion phase for the plasma channel, lasting approximately 5 ns, during which the column doubles in radius. This phase is followed by a 5 ns contraction period because the increased radius leads to an overshoot of the quasi-equilibrium curve in accordance with Eq. 2.51. The remainder of the current pulse, approximately 100 ns, is associated with a nearly constant radius phase. The predictions of the column dynamics by the global MHD code are qualitatively insensitive to the water switch mode and the fill pressure, in the 5.5-11 psia regime. It must be emphasized that a fundamental assumption in the computer model is the constant line density, N.

We have obtained measurements of the plasma line density as a function of time at two different filling pressures for both experimental configurations using data from several machine shots (Figs. 4.21-4.24). In each case, the line density monotonically increases with a value within the first 25 ns of

$$\frac{dN}{dt} \sim 1\text{-}2\times10^{26}\ \text{m}^{-1}\text{s}^{-1} \quad . \tag{4.12}$$

For an initial line density corresponding to 100 μ radius and full ionization at

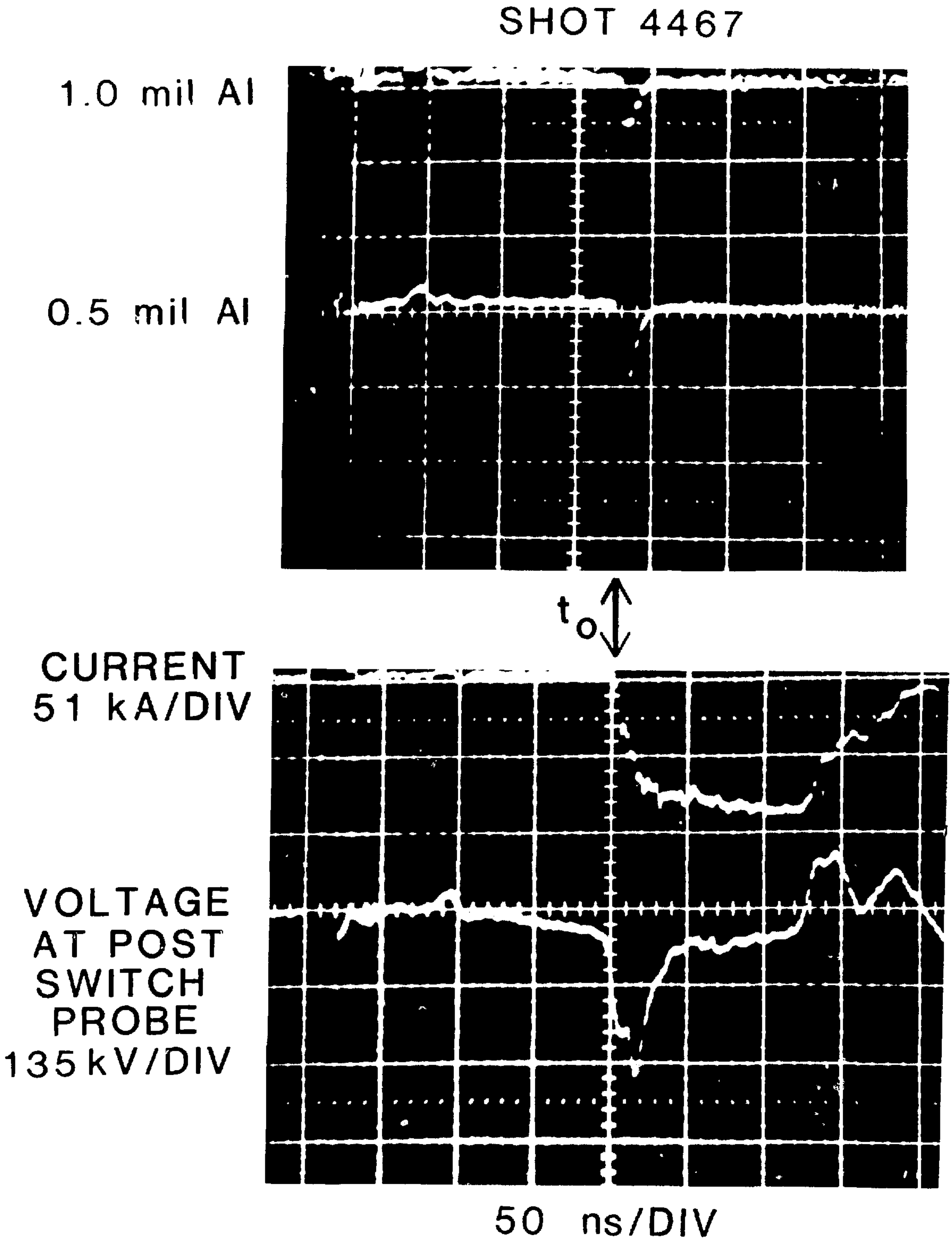

Fig. 4.18 X-ray diagnostic photomultiplier signals for a switch operative shot

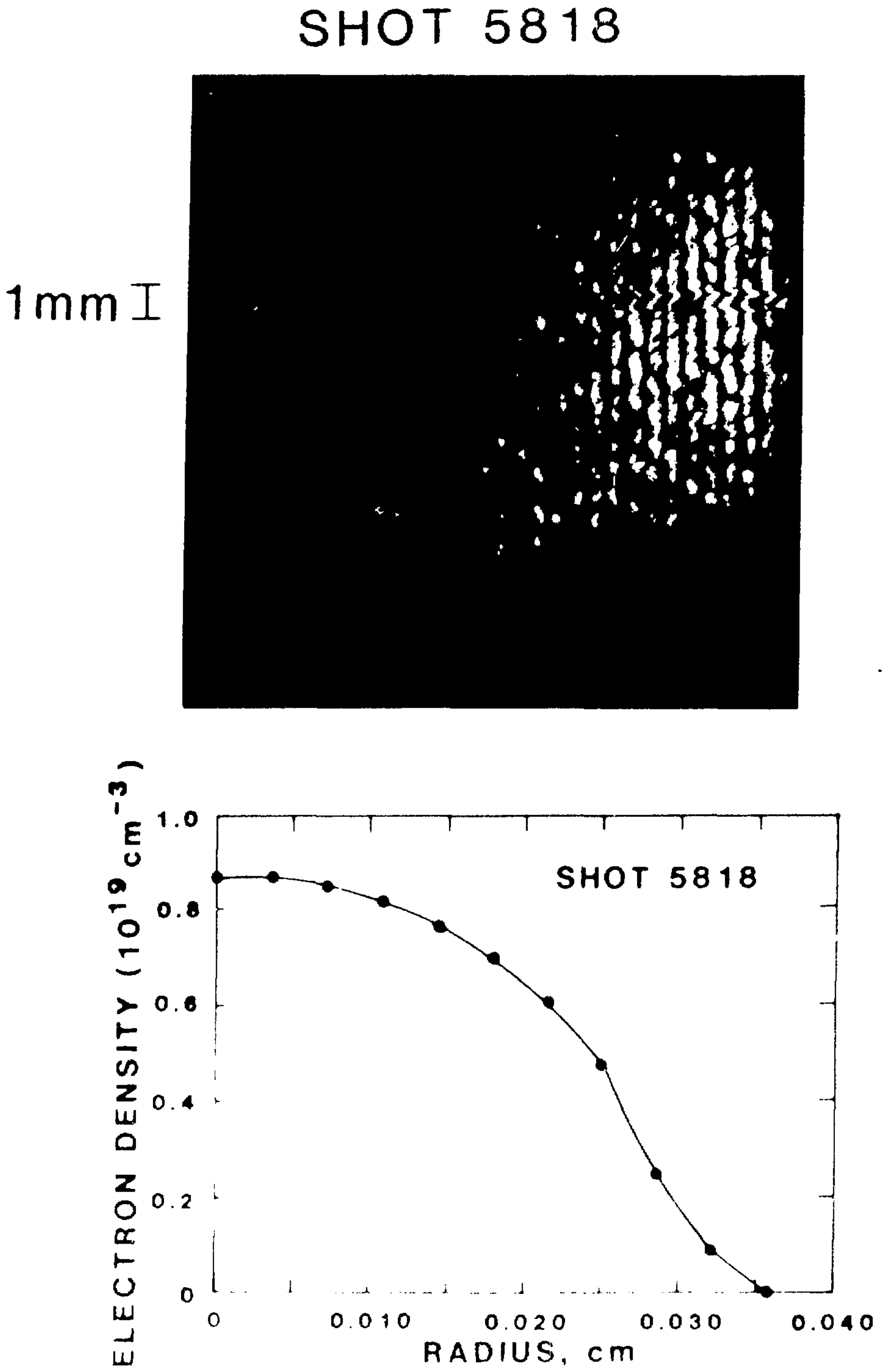

Fig. 4.19 Typical Moiré-Schlieren photograph with computed electron density profile

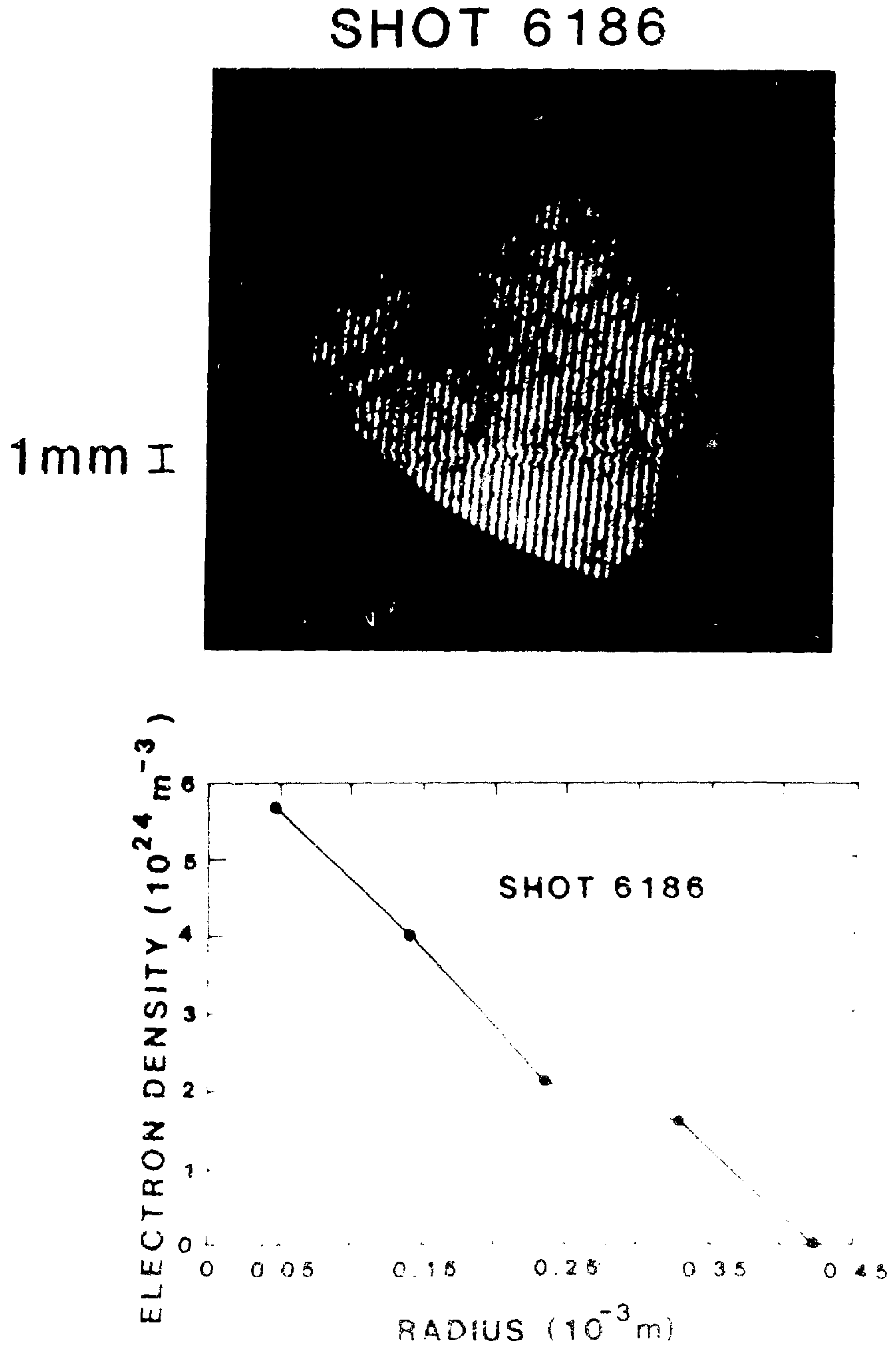

Fig. 4.20 Typical interferogram with computed electron density profile

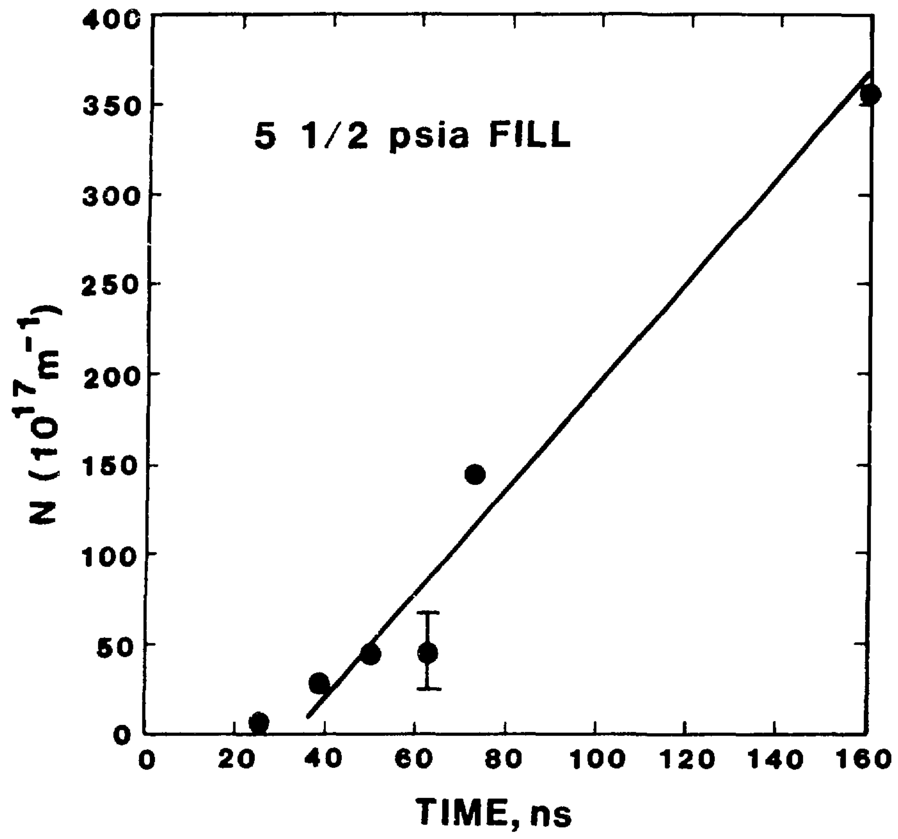

Fig. 4.21 Plasma line density--shorted switch mode--5.5 psia H_2

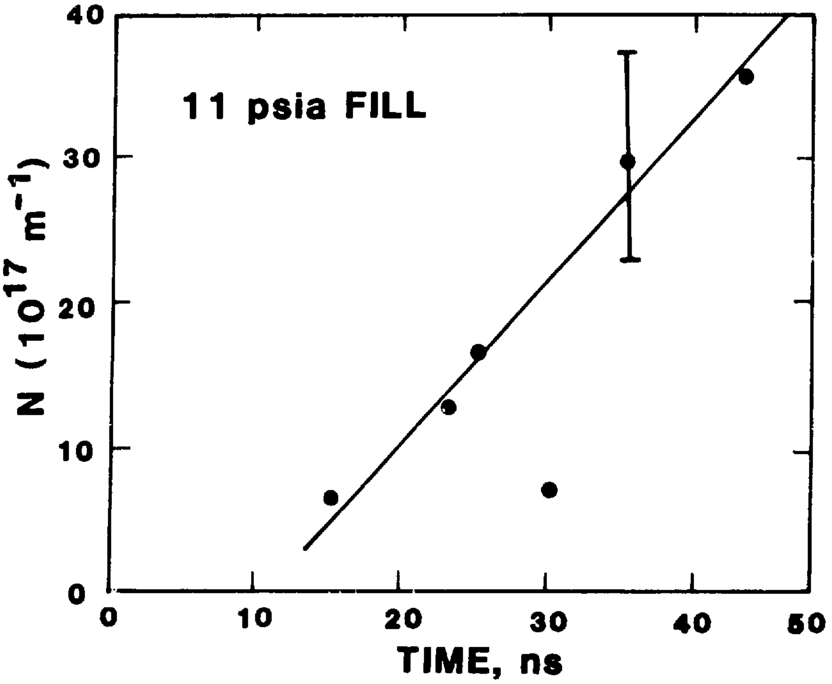

Fig. 4.22 Plasma line density--shorted switch mode--11 psia H_2

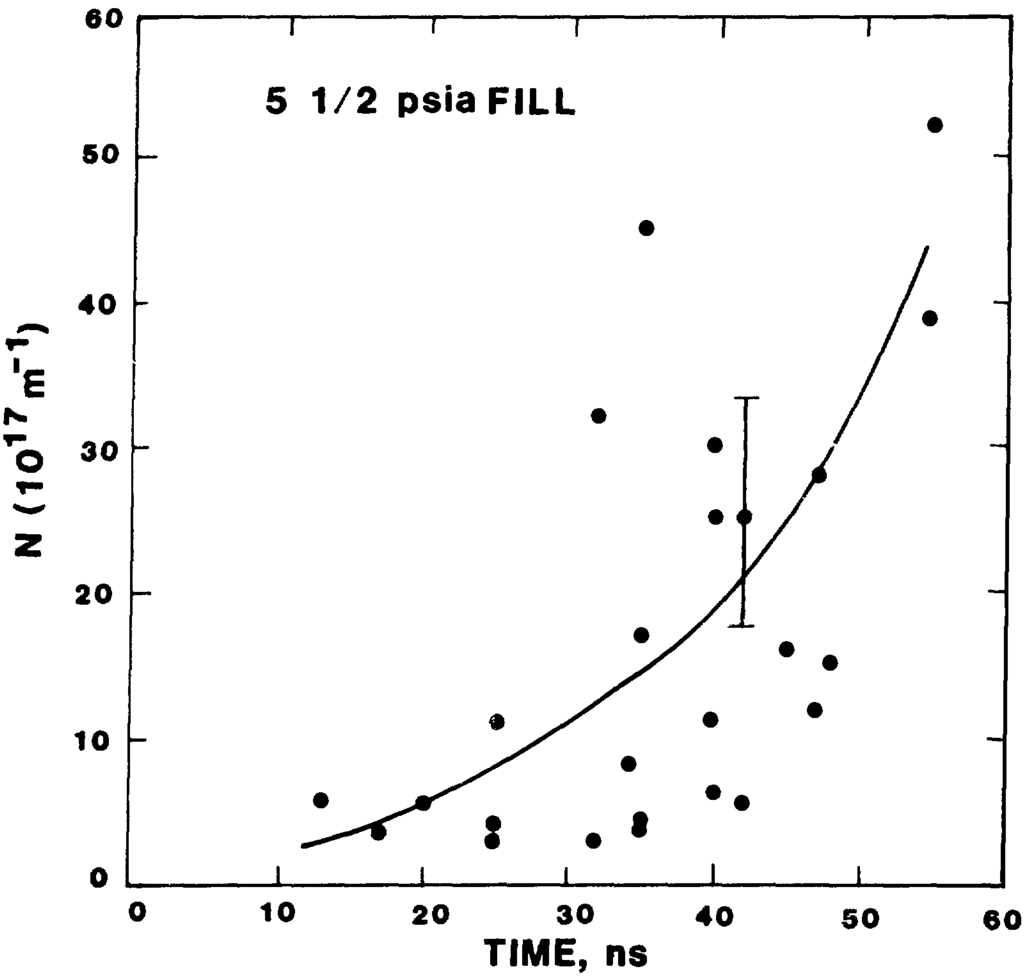

Fig. 4.23 Plasma line density--switch operative mode--5.5 psia H_2

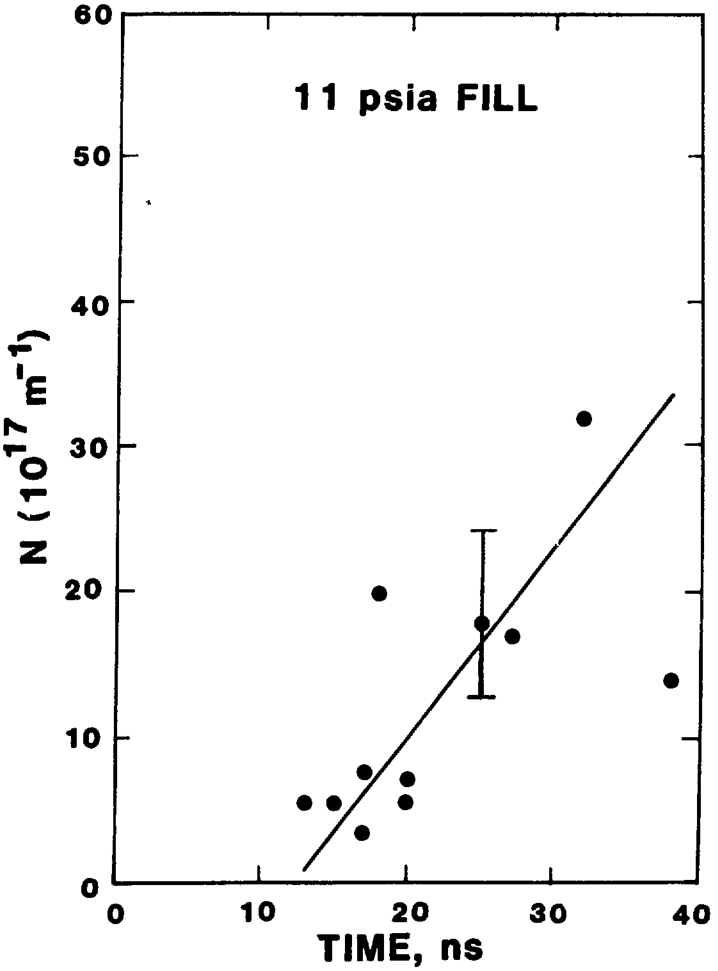

Fig. 4.24 Plasma line density--switch operative mode--11 psia H_2

the standard fill pressure of 11 psia, this implies a doubling time of 10 ns. The channel radius also increases with time at a rate relatively independent of fill pressure or switch mode; we find (Figs. 4.25-4.28)

$$\frac{dr}{dt} \sim 1\text{-}2\times10^4 \ \mathrm{ms}^{-1} \quad . \tag{4.13}$$

The optical diagnostics provide no evidence for an accompanying drop in the electron density on axis, and we rule out the hypothesis that the observed radius increases are associated with a simple column expansion. Instead, the data are reasonably consistent with an accretion model in which the change in column radius is a result of the creation of new plasma at the channel-neutral gas interface. For this model, we expect

$$\frac{dN}{dt} \simeq 2\pi rn \frac{dr}{dt} \quad . \tag{4.14}$$

As a comparison with Eq. (4.12), we calculate the predicted line density rise for the switch operative mode at 5.5 psia H_2. At a measured radius of 180 μ (Fig. 4.27) and an atomic fill density of 1.8×10^{25} m^{-3}, Eq. (4.14) yields

$$\frac{dN}{dt} \simeq 2.8\times10^{26} \ \mathrm{m}^{-1}\mathrm{s}^{-1} \tag{4.15}$$

for the experimentally determined expansion rate of

$$\frac{dr}{dt} \sim 1.4\times10^4 \ \mathrm{ms}^{-1} \quad . \tag{4.16}$$

The observed line density increases are intuitively undesirable because pressure balance for a given current is achieved at lower average temperatures for higher line densities. Optimistically, however, one might hope that all the load current flowed within the original plasma. The increased line density in this model would merely indicate the creation of a high resistivity coronal

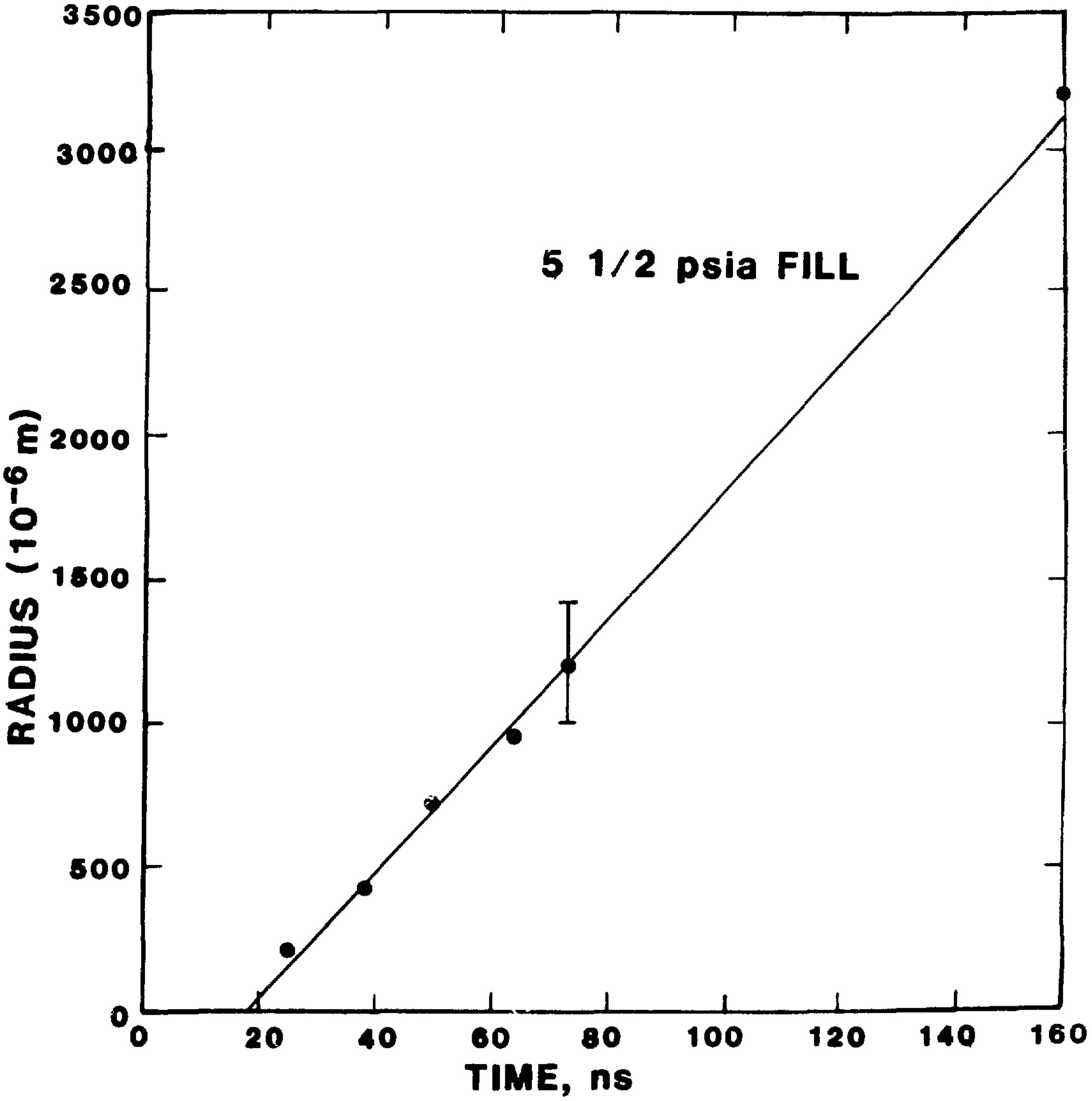

Fig. 4.25 Channel radius--shorted switch mode--5.5 psia H_2

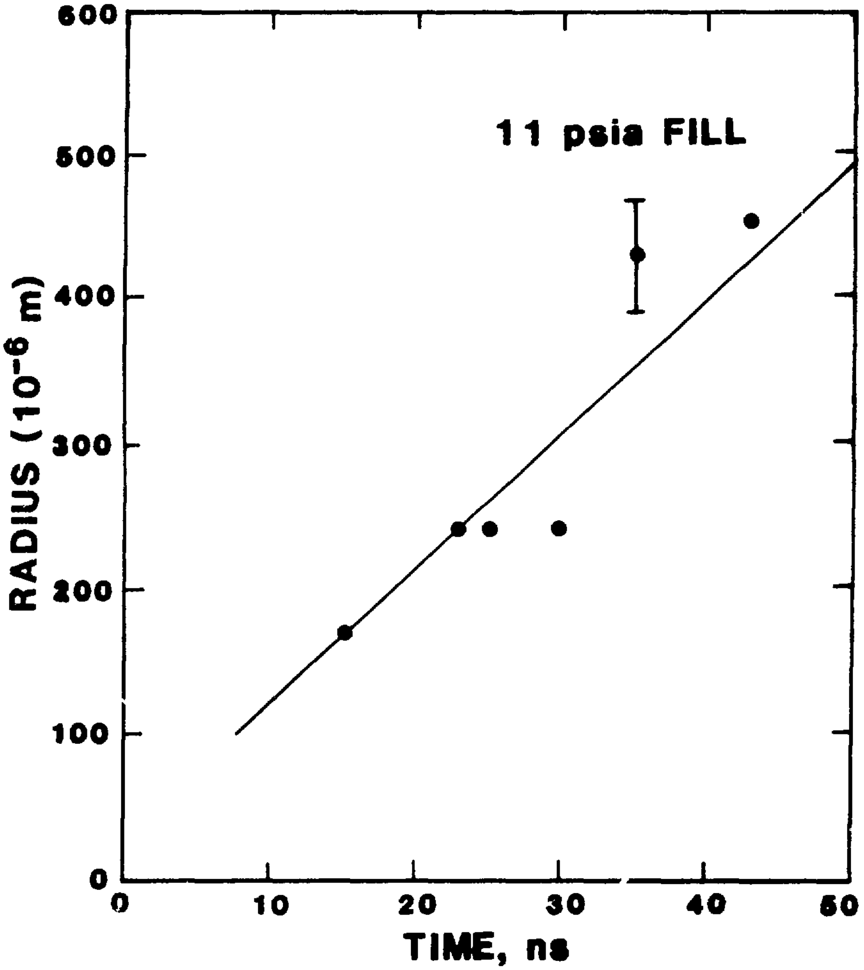

Fig. 4.26 Channel radius--shorted switch mode--11 psia H_2

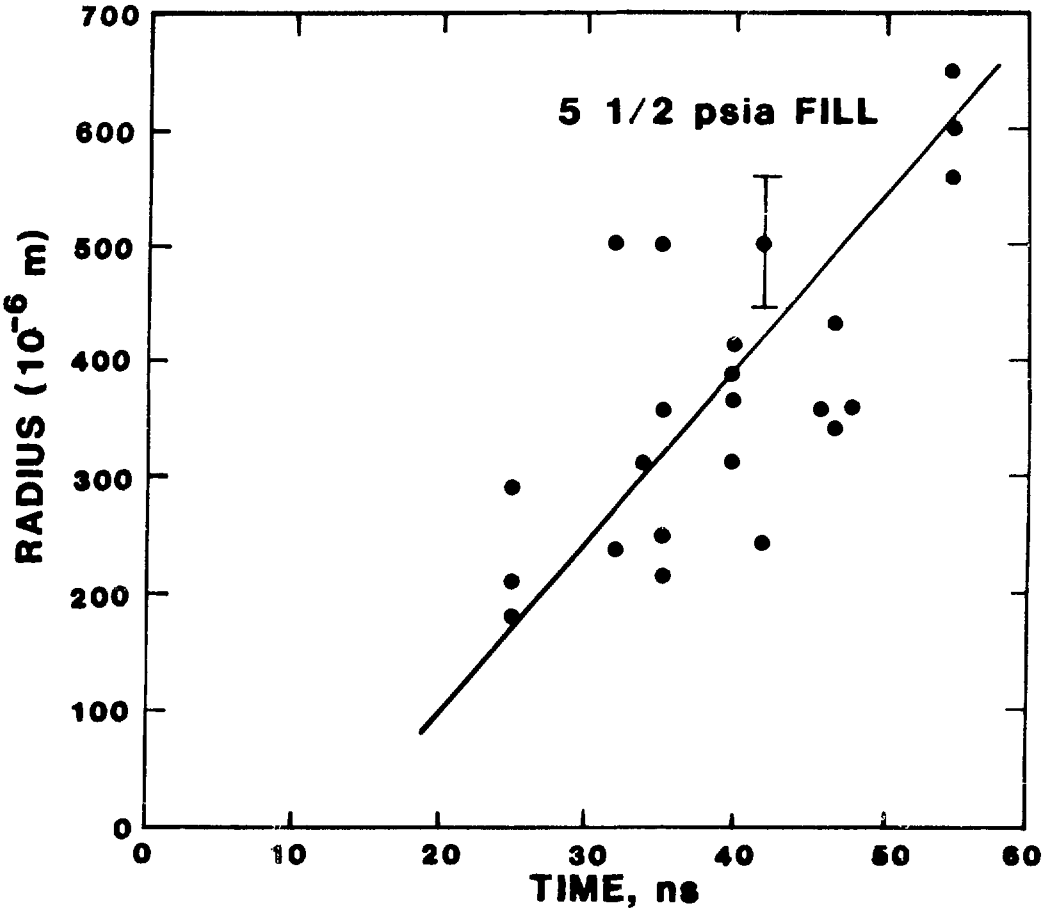

Fig. 4.27 Channel radius--switch operative mode--5.5 psia H_2

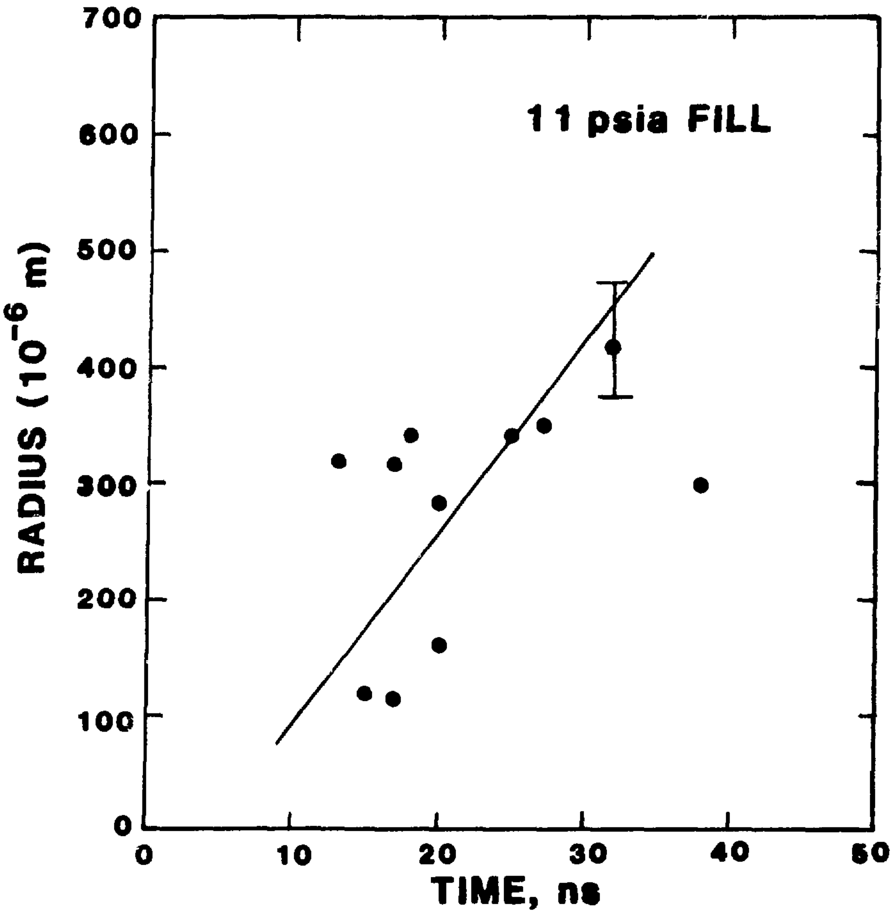

Fig. 4.28 Channel radius--switch operative mode--11 psia H_2

region surrounding the channel, through which additional magnetic field might rapidly diffuse. To test this hypothesis, we have examined the previous data from a slightly different viewpoint; namely, we have investigated the dynamics of the region which contains the original line density. For each set of conditions, we determine the minimum observed line density, N_o, and plot the time dependence of the channel radius containing this line density, $r_{N_o}(t)$ (Figs. 4.29-4.32). The radius values are obtained by truncating the integration of the electron density distributions for both the Moiré-Schlieren and interferometric results. As a comparison, we have applied the global MHD model to the conditions of a constant line density channel with an initial radius determined by the fill pressure and N_o. The code predicts the dynamics of a channel which carries the entire current and maintains the line density, N_o, at all times. The discrepancy between code and experiment clearly indicates that the load current is not being carried entirely within the original line density of the channel, but is at least distributed into the larger accreted region. The ionized coronal region is therefore incorporated into the central plasma channel and participates in its dynamics; this fact underscores the importance of the accretion measurements.

The disagreement between the global MHD model predictions and experimental observations of the channel dynamics reflects the inadequacies of a constant line density calculation. A more fundamental disagreement has been observed between the x-ray diagnostic data and the temperature estimates based on measured line density, number density, channel current, and dynamics. An effective Bennett temperature may be calculated from the measured line density, with the assumption that the total load current flows in the observed channel and determines the field pressure which balances the plasma internal pressure. The evidence for channel expansion (Figs. 4.25-4.28) suggests that this Bennett temperature will be a lower limit to the actual average plasma temperature, if $B_z = 0$ and current flows only in the visible channel, because the net force in the column is outward. The Bennett temperature may then be used to estimate a bremsstrahlung yield and, finally, to predict a photomultiplier current for the density and volume of plasma determined from the Moiré-Schlieren and interferometric data. The efficiencies and sensitivities of the components in the x-ray diagnostic are supplied by manufacturer's data and experiment.

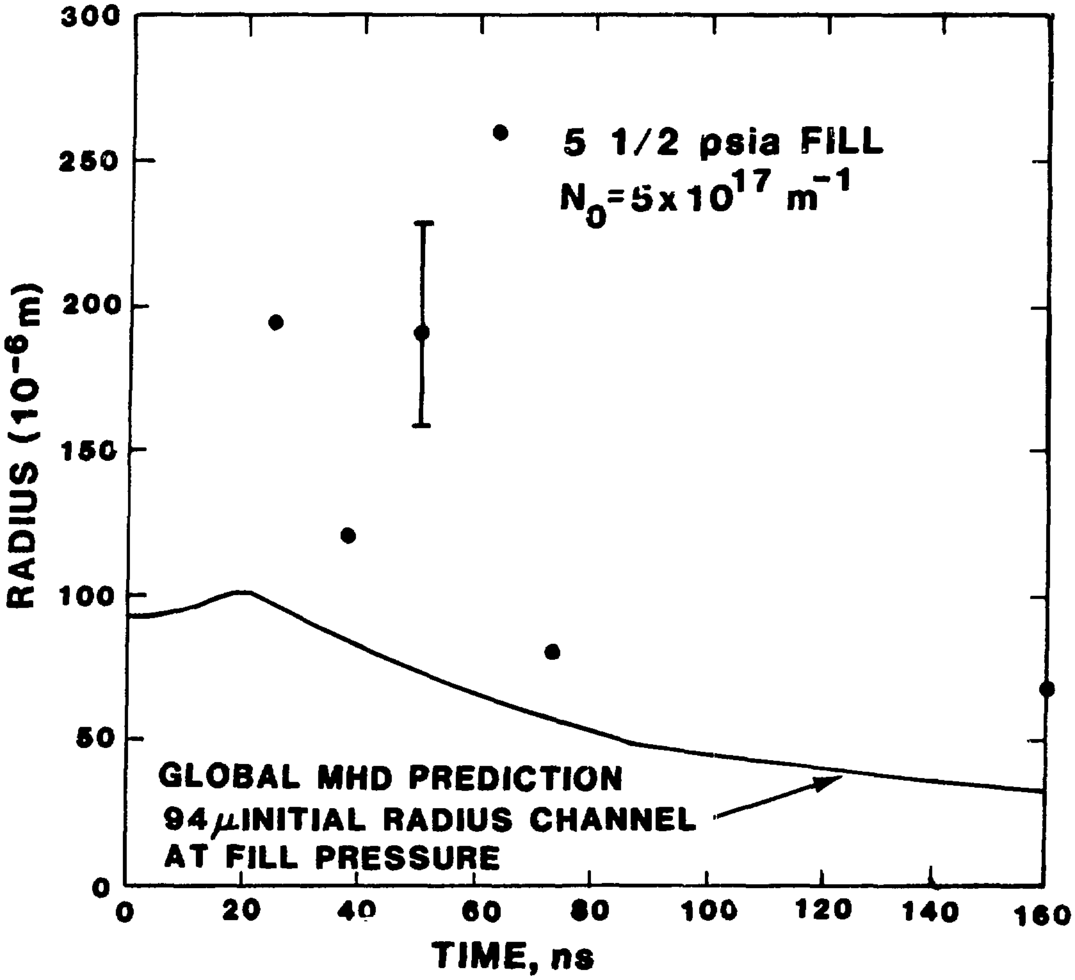

Fig. 4.29 $r_{N_0}(t)$--shorted switch mode--5.5 psia H_2

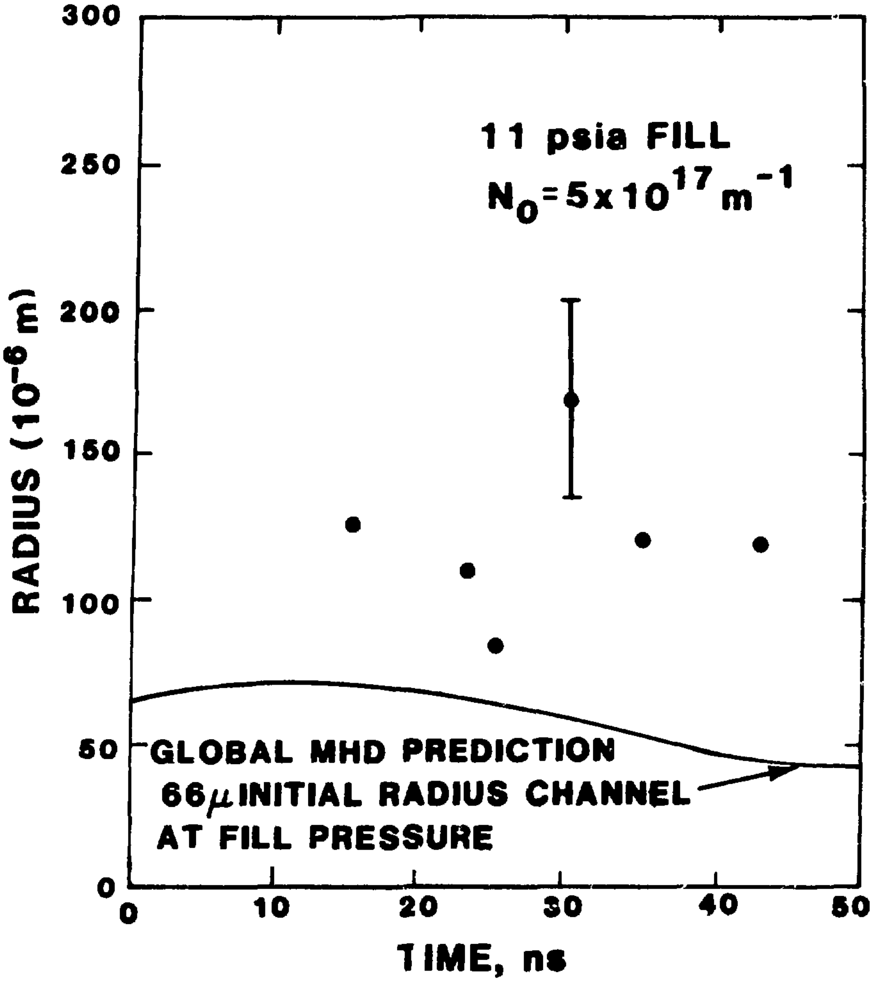

Fig. 4.30 $r_{N_0}(t)$--shorted switch mode--11 psia H_2

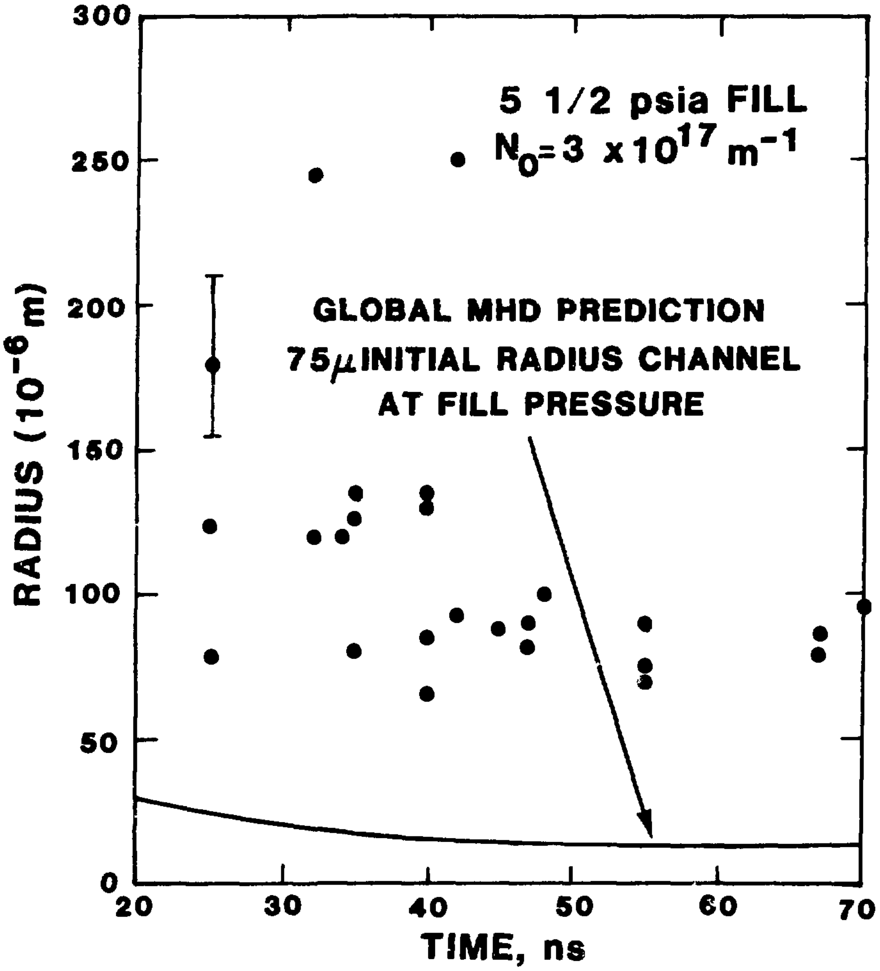

Fig. 4.31 $r_{N_0}(t)$--switch operative mode--5.5 psia H_2

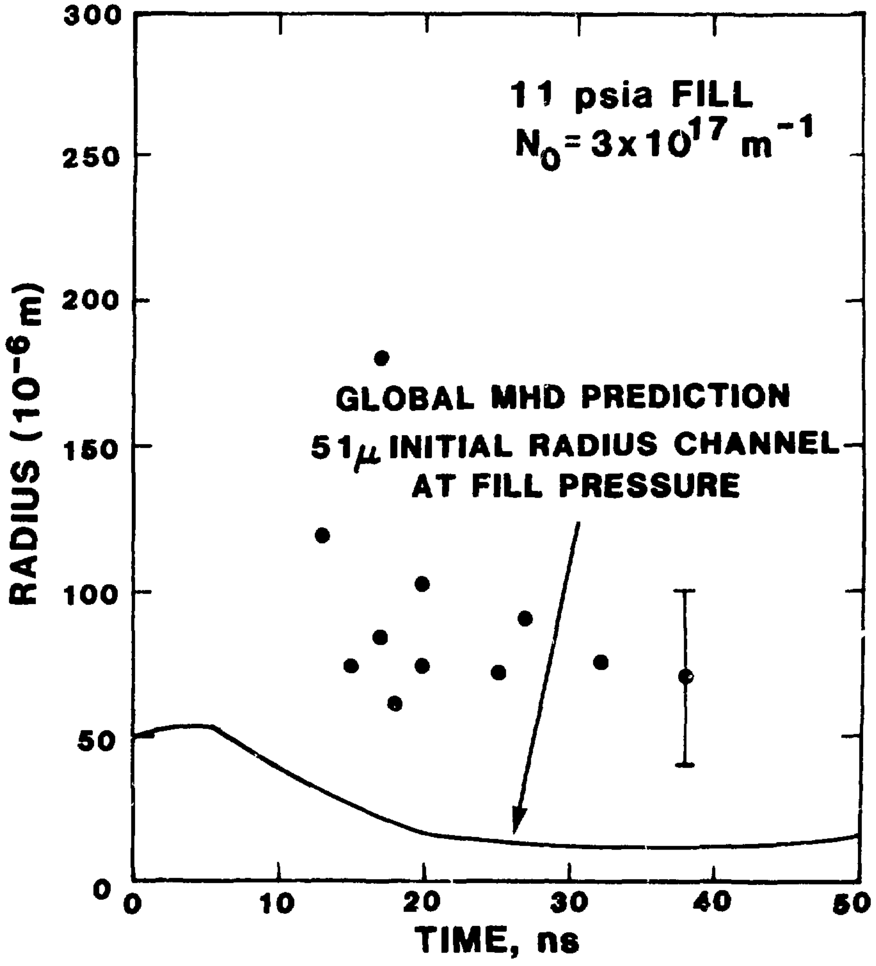

Fig. 4.32 $r_{N_o}(t)$--switch operative mode--11 psia H_2

Under shorted switch conditions (Figs. 4.33-4.34), the Bennett temperatures lie in the range

$$30 \text{ eV} < T_B < 150 \text{ eV} \tag{4.17}$$

and are not inconsistent with the absence of x-ray signals following an initial spike from the photomultipliers. For the switched mode (Figs. 4.35-4.36), however, we find

$$100 \text{ eV} < T_B < 3000 \text{ eV} \quad , \tag{4.18}$$

and photomultiplier signals should be visible as late as 60 ns after the onset of current. This is in sharp contrast with the observations of a narrow x-ray spike with little or no tail after 30 ns. Precise knowledge of the relative timing of the signals from the N_2 laser monitor, the current probe, and the photomultipliers is of extreme importance to these measurements. This timing data has been obtained using a light emitting diode as an optical source for the photodetectors while monitoring the current through the diode using the cable normally attached to the current probe. In addition, we have used pulse generator signals to determine cable delays, and in conjunction with manufacturer supplied data for the photodetectors, the results confirm the LED data.

The x-ray measurements from the two-foil absorber diagnostic suffer from dynamic range limitations associated with the high amplitude initial spike. This early signal often exceeds the photomultiplier saturation level and sets an upper limit on the oscilloscope gain, thereby reducing the diagnostic sensitivity. In an attempt to determine the origin of the early x-ray signal, with the hope of eventually eliminating this spike, a simple pinhole camera was constructed. A thin (0.3 mil Al) foil covering the pinhole acted as both a light and vacuum seal. Special emulsion-free soft x-ray sensitive films (Kodak 101-01 and RAR-2490) were used, but the x-ray flux was not sufficient to create an image. Plasma shots taken with a Marx bank voltage but no initiation ruby laser pulse, producing the filamentary background structures discussed previously, show the same spike in the x-ray detector signals, and we have

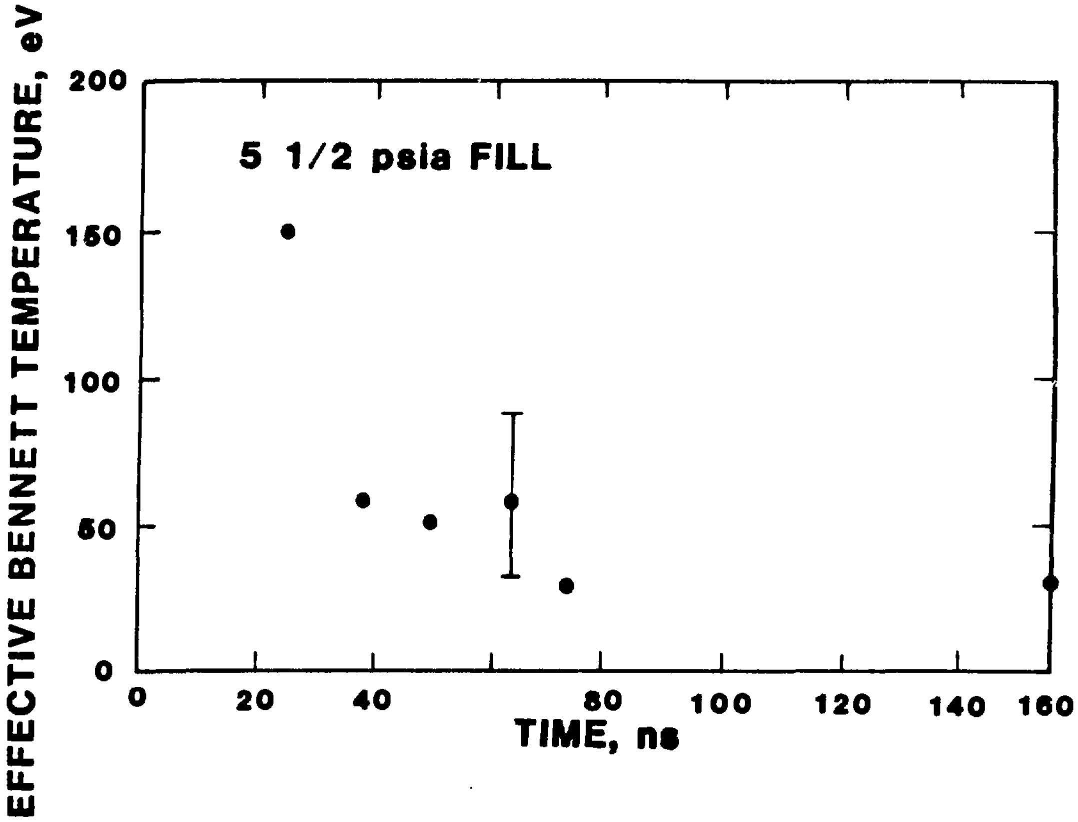

Fig. 4.33 Bennett temperature--shorted switch mode--5.5 psia H_2

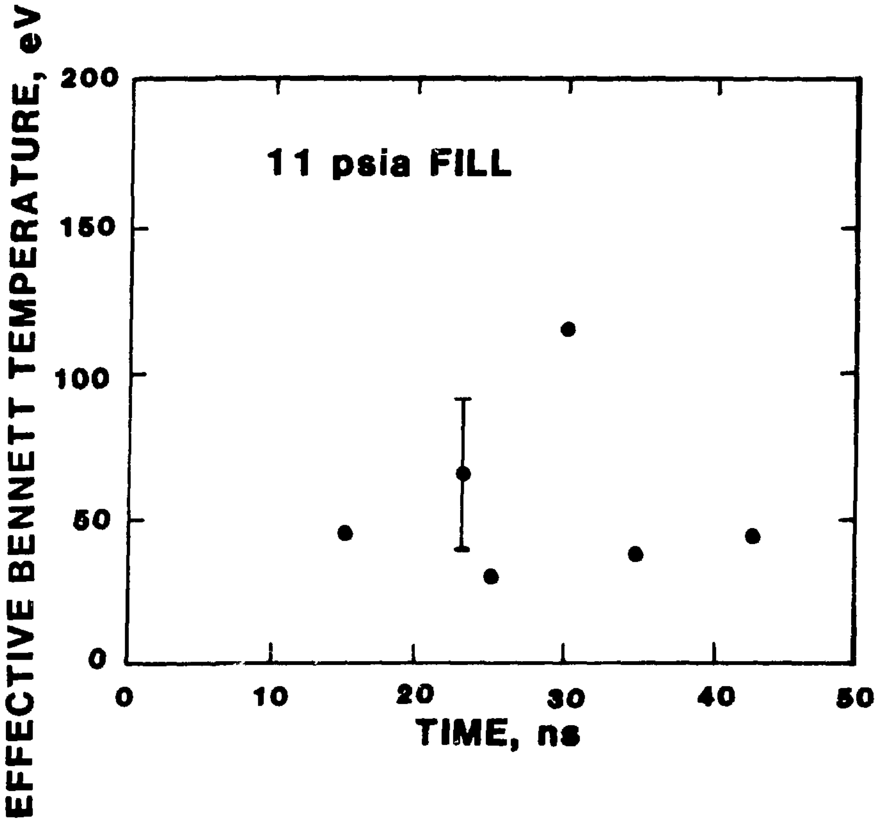

Fig. 4.34 Bennett temperature--shorted switch mode--11 psia H_2

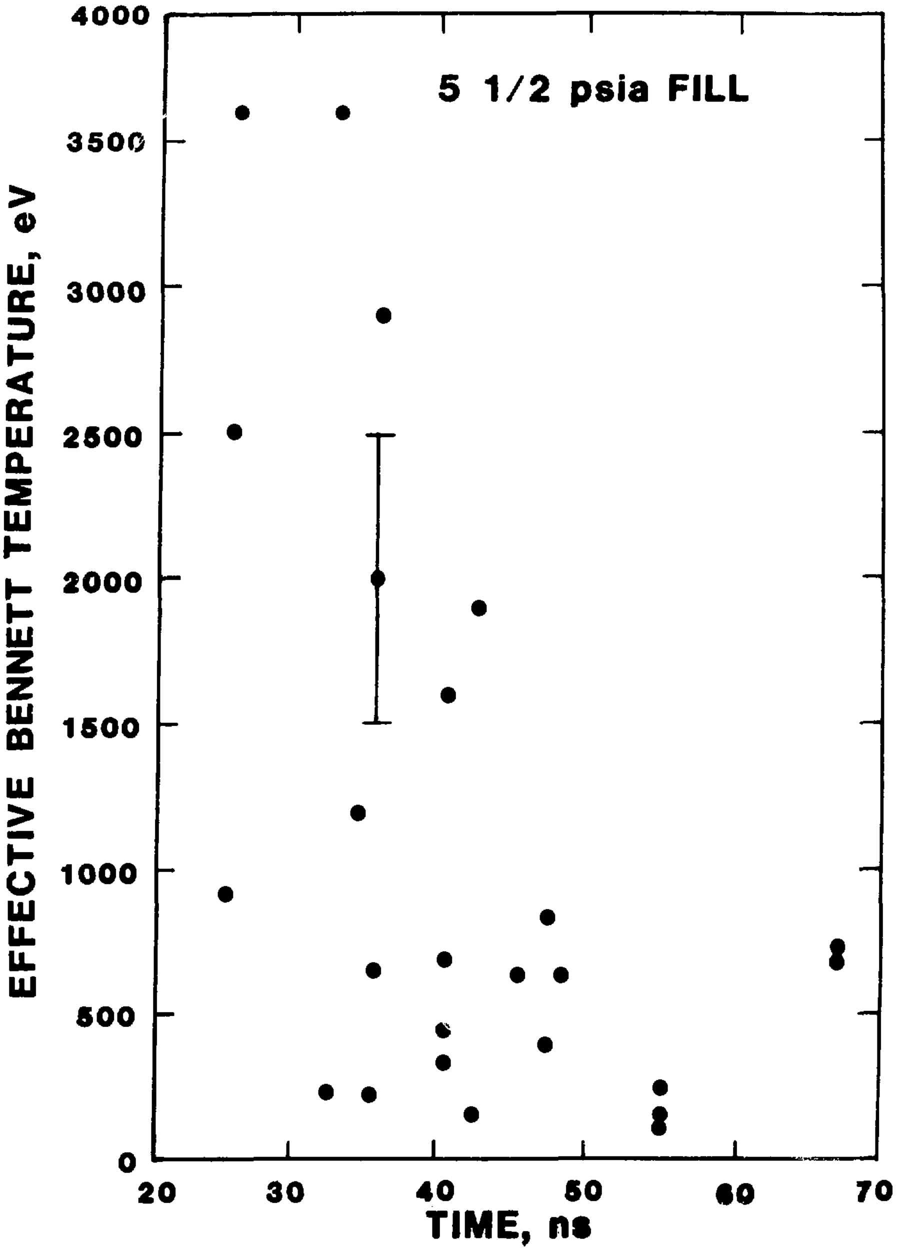

Fig. 4.35 Bennett temperature--switch operative mode--5.5 psia H_2

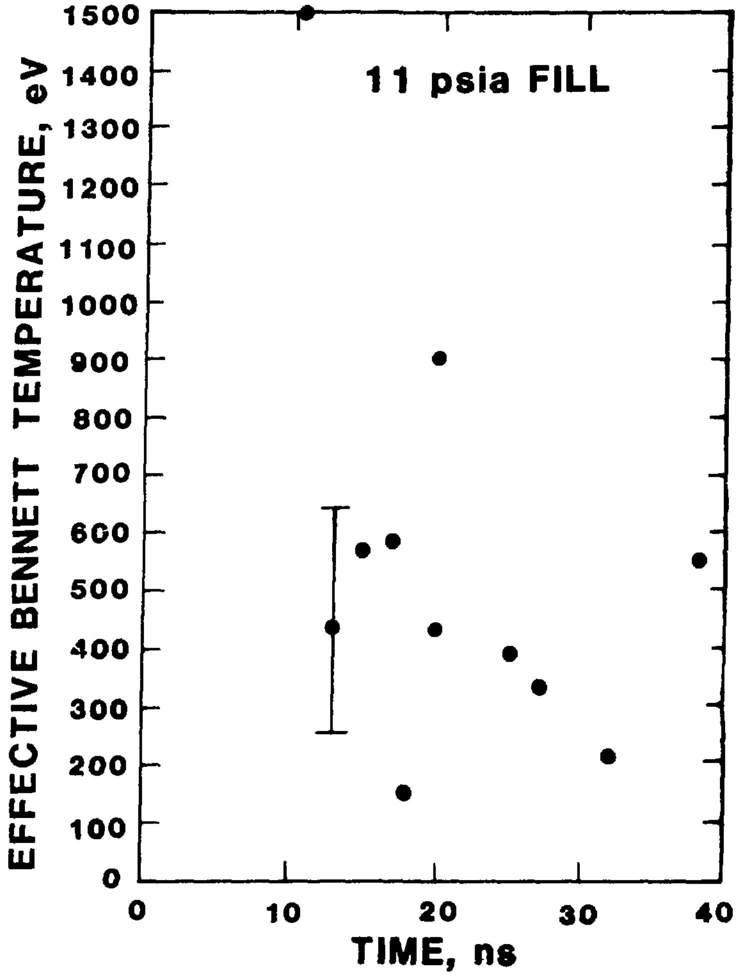

Fig. 4.36 Bennett temperature--switch operative mode--11 psia H_2

concluded from these shots that the spike is probably not associated with the central channel observed in laser-initiated discharges.

Careful examination of the photomultiplier signals using the ruby laser as a test source has indicated anomalous behavior (jagged afterpulsing) of the tubes when operated in proximity to the load chamber during the high voltage breakdown of the gas. This may have been caused by small leakage currents to the photocathode surface and led to the implementation of an alternate detection scheme. For this diagnostic, the photomultiplier is housed inside the screen room and is electrically shielded from the load chamber. The output of a scintillator is transmitted to the photocathode by four 1/8 in. diam fiber optics cables (Nanofast OC-50). The scintillator (2 in. diam Pilot B) is located at the chamber, directly above a 1 mil Al vacuum seal which is supported by an aluminum rib structure; there is no x-ray collimator in this sytem. The x-ray signals obtained by this single-absorber detector were essentially identical to those observed with the two-foil diagnostic, although shot-to-shot reproducibility was somewhat improved.

To eliminate the possibility of current paths well outside the field of view of the optical diagnostics, new insulators were designed to shield all but a small central region (1/2 in. diam) of each chamber electrode (Fig. 4.37). The polyethylene insulator covering the high voltage dump electrode replaced the plexiglass separation between the water line and the chamber, and was bolted to the existing flanges. For the ground side, a plexiglass disc insulator was glued to the aluminum electrode surface using a polyurethane adhesive (Adiprene). The Moiré-Schlieren and interferometric data obtained after installation of these insulators is virtually identical to the previous results. The x-ray signals, however, while retaining the same initial spike temporal history, are reduced in amplitude by two orders of magnitude, thereby overcoming the dynamic range problems and increasing the detector sensitivity. As in the earlier signals, no x-rays are observed after the narrow spike. Bennett temperatures for the switch operative mode, determined from Moiré line density measurements, are again in the range of Eq. (4.18), and the predicted photomultiplier signals are

$$250 \text{ mV} \lesssim V_{PM}^{\text{predicted}} \lesssim 5 \text{ V} \quad . \qquad (4.19)$$

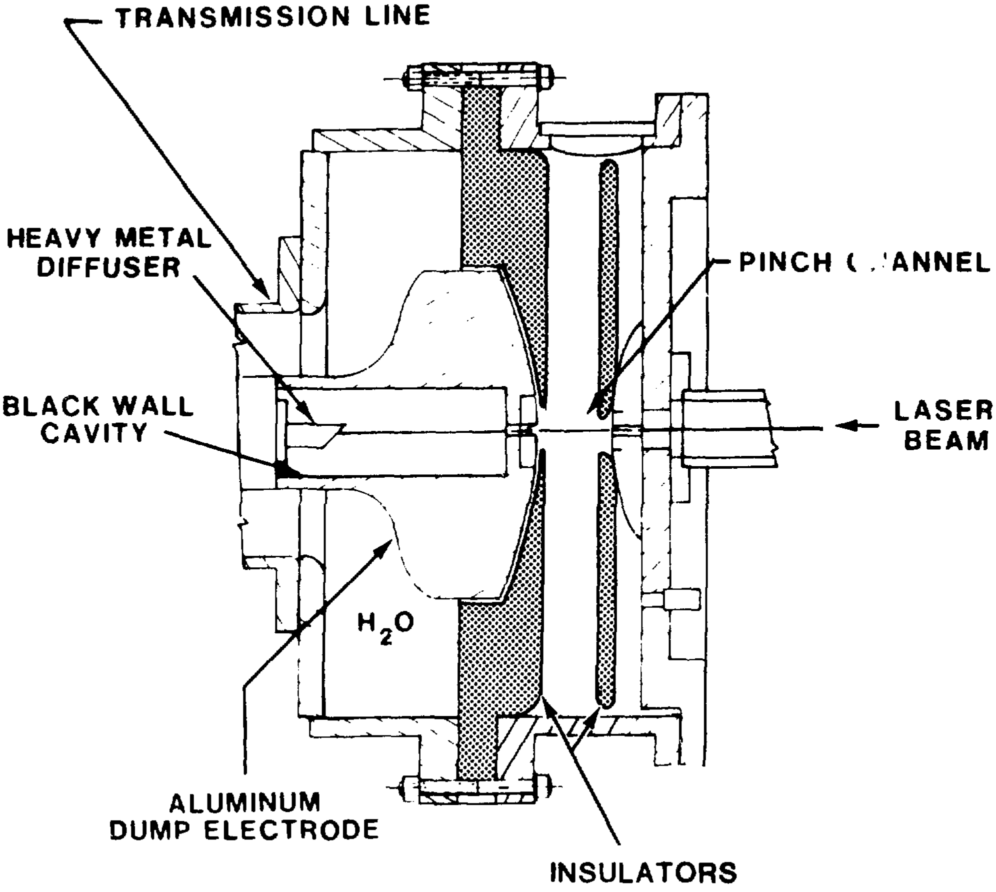

Fig. 4.37 Load chamber modification illustrating insulators covering electrodes

The x-ray detector data using the insulator modification, however, indicate

$$V_{PM}^{actual} \lesssim 5 \text{ mV} \qquad (4.20)$$

after the initial 10-20 mV spike. We believe that this discrepancy between the x-ray diagnostic signals and temperature estimates based on observed electron density profiles constitutes a fundamental problem which is most plausibly explained by the hypothesis that the bulk of the load current is not flowing in the laser-initiated channel. We support this hypothesis with additional MHD code results, simple calculations, and further experiments.

4.4 Non-localized Current Model

We begin by examining experimental observations which are strongly dependent on the relative timing between the N_2 laser monitor and the current probe signals. On several shots with the water switch operative, the N_2 laser has been triggered at low values of load current ($I \lesssim 30$ kA) corresponding to the first 10 ns of current. In a number of the Moiré photographs taken under these conditions there is no evidence for any refraction. These data suggest that a weakly ionized, uniform density region may be carrying the current, with a resultant refractivity below the detection threshold of the optical diagnostic.

In further experiments, the chamber was initially filled to 5.5 psia H_2, and the initiation laser was operated under conditions which produced Moiré photographs indicating a single, narrow channel, free of parallel filamentary structures. Additional H_2 was then added to the chamber to double the pressure. Moiré photographs displayed a multitude of filaments, each presumably carrying a fraction of the load current. The increased neutral gas density is expected to have two effects, however, each <u>increasing</u> the likelihood that current will flow in the laser-initiated channel. First, for identical Marx bank voltages, the higher pressure gas will have a lower breakdown stress (E/P), and the chance of bulk breakdown outside the laser interaction region should be decreased. Second, the ruby laser light is expected to couple more efficiently to a higher pressure gas, and thus create a more well defined channel precurser. The effective laser electric field, using the ac generalization of classical avalanche theory,[5] is

$$E_{\text{effective}} = \frac{\nu}{\omega} E_{\text{laser}} \quad , \tag{4.21}$$

where ν is the electron-neutral collision frequency and ω is the optical frequency. The collision frequency rises linearly with density, and the electron avalanche time falls dramatically with increased field strength; thus we predict a more highly ionized channel region at higher pressures. In actuality, we have nearly always observed filamentary structures at high filling pressures ($p \gtrsim 25$ psia) except at the highest laser pulse energies, for switch operative conditions. We conclude from these results that current might flow outside the laser-produced channel region, even under conditions where no filamentary structures are evident. It is possible that high pressure operation merely enhances the sensitivity of the optical diagnostics by increasing the refractive gradients. The discrepancy between Bennett temperature measurements and x-ray detector signals might then be interpreted as a result of an erroneous assumption about the current distribution in the load chamber; the Bennett temperatures are too large by the square of the ratio of total load current to the current in the visible channel.

A simple estimate of the electric field required to maintain the bulk of the current in a weakly ionized, "invisible" region outside the central channel is also consistent with our hypothesis. For this calculation, we assume a total load current of 100 kA. We also assume that a current

$$I_{\text{out}} = 80 \text{ kA} \tag{4.22}$$

is flowing in a large region outside the laser-initiated column; the central column carries only 20 kA. For $r_{\text{out}} = 5$ mm, the current density in the outer zone is

$$j_{\text{out}} \approx \frac{I_{\text{out}}}{\pi r_{\text{out}}^2} \simeq 10^9 \text{ Am}^{-2} \quad . \tag{4.23}$$

The outer zone electron density must be below the detection threshold for the Moiré or interferometric diagnostics; we assume

$$n_e^{out} < 10^{23}\ \mathrm{m^{-3}} \quad . \tag{4.24}$$

From Eqs. (4.23) and (4.24) we calculate

$$v_d = \frac{j_{out}}{n_e^{out}\ q_e} > 6\times10^4\ \mathrm{ms^{-1}} \tag{4.25}$$

where v_d is the electron drift velocity. From published data[6] on the electron mobility in H_2, we find

$$\frac{E}{N} = 50\ \mathrm{Td}\ \text{for}\ v_d = 6\times10^4\ \mathrm{ms^{-1}} \tag{4.26}$$

where 1 Td = 10^{-21} Vm^2 and N is the neutral molecular density. For a filling pressure of 11 psia H_2, $N = 1.8\times10^{25}\ \mathrm{m^{-3}}$ and we find

$$E \gtrsim 9\times10^5\ \mathrm{Vm^{-1}} \quad , \tag{4.27}$$

or for our 5 cm gap,

$$V_{sustain} \gtrsim 45\ \mathrm{kV} \quad . \tag{4.28}$$

Alternatively, we can estimate the mobility from the collision time for an electron in the neutral background,

$$\tau = \frac{1}{N\sigma v_t} \quad , \tag{4.29}$$

where v_t is the electron thermal speed. Using an electron energy of 0.5 eV, we obtain[7]

$$\sigma \sim 10^{-19}\ \mathrm{m}^2 \tag{4.30}$$

and

$$\tau \simeq \frac{1}{1.8\times 10^{25}\ \mathrm{m}^{-3} \times 10^{-19}\ \mathrm{m}^2 \times 3\times 10^5\ \mathrm{ms}^{-1}} \simeq 2\times 10^{-12}\ \mathrm{s} \quad . \tag{4.31}$$

The calculated mobility, μ, is given by

$$\mu = \frac{q_e}{m_e}\tau \simeq 3.3\times 10^{-1}\ \mathrm{s}^{-1}\mathrm{V}^{-1}\mathrm{m}^2 \quad . \tag{4.32}$$

Thus

$$E = \frac{v_d}{\mu} \gtrsim 2\times 10^5\ \mathrm{Vm}^{-1} \tag{4.33}$$

or

$$V_{\mathrm{sustain}} \gtrsim 10\ \mathrm{kV} \quad . \tag{4.34}$$

Both calculations suggest that the electric field required to drive the bulk of the load current in a low ionization, large volume region is consistent with the data obtained from a capacitive voltage probe in the insulator at the chamber-transmission line interface.

In addition to the global MHD model calculations, computer simulation of the plasma behavior in the prototype HDZP experiment has been performed with a two-dimensional MHD (MANIAC) code. The results[8] indicate that for the most optimistic estimates of the ruby laser parameters, i.e., maximum power and minimum divergence, only 20 kA of the total load current is contained within a laser-initiated channel of radius 300 μ. We do not expect complete agreement between code and experiment; in particular, an accurate description of the breakdown process is extremely complicated, three-dimensional, and requires detailed knowledge of the initiation laser spatial and temporal profiles. The predictions nevertheless provide a self-consistent picture in which the bulk of the current flows outside of a small channel. The code results indicate peak plasma temperatures of 90 eV for water-switched operation, consistent with the x-ray diagnostic data. Furthermore, the calculations yield an electron density profile (Fig. 4.38) which can be reduced computationally to theoretical Moiré and interferometric fringe patterns (Figs. 4.39 and 4.40). While the details of the MANIAC-predicted central channel profile are not in good agreement with experimental results, we note that neither optical diagnostic would suspect that only 20% of the current is contained within a small radius; optical diagnostics are simply not current profile diagnostics.

Experimental measurements of accretion have revealed the inadequacies of simple analytic and computational models which assume a constant line density. Results from quantitative density diagnostics and current probes along with the data from x-ray detectors have further suggested that laser-initiated channels in the pressure range 5.5 psia-11 psia H_2 do <u>not</u> contain all of the load current. This hypothesis is consistent with additional experimental evidence, sophisticated MHD code predictions, and simple calculations.

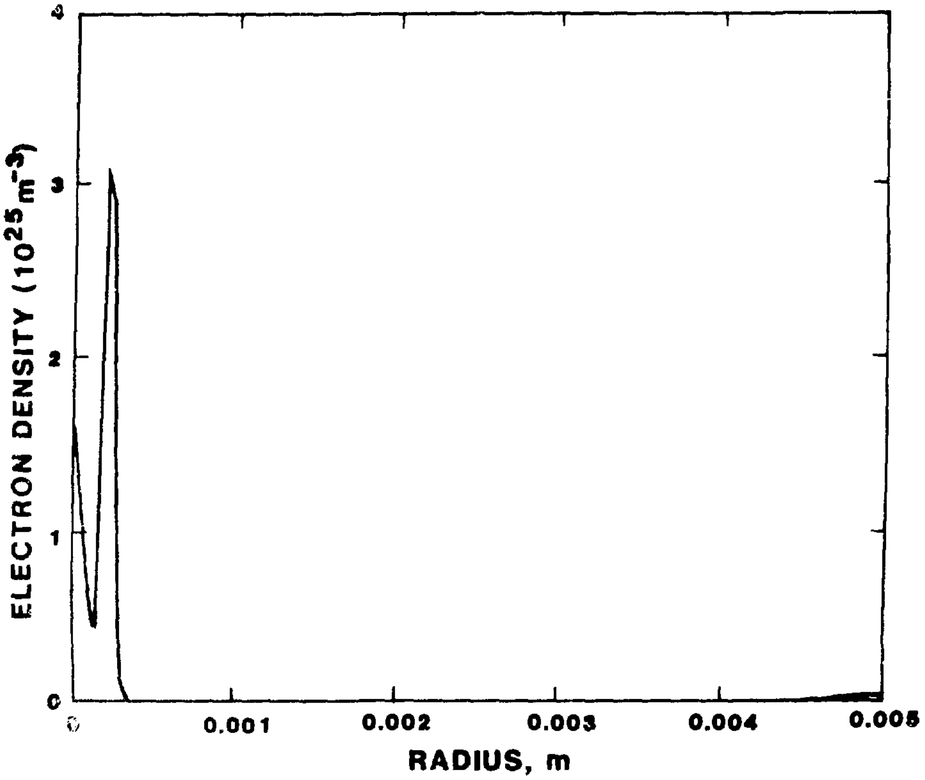

Fig. 4.38 MANIAC computed electron density profile

(reproduced from I. R. Lindemuth, private communication)

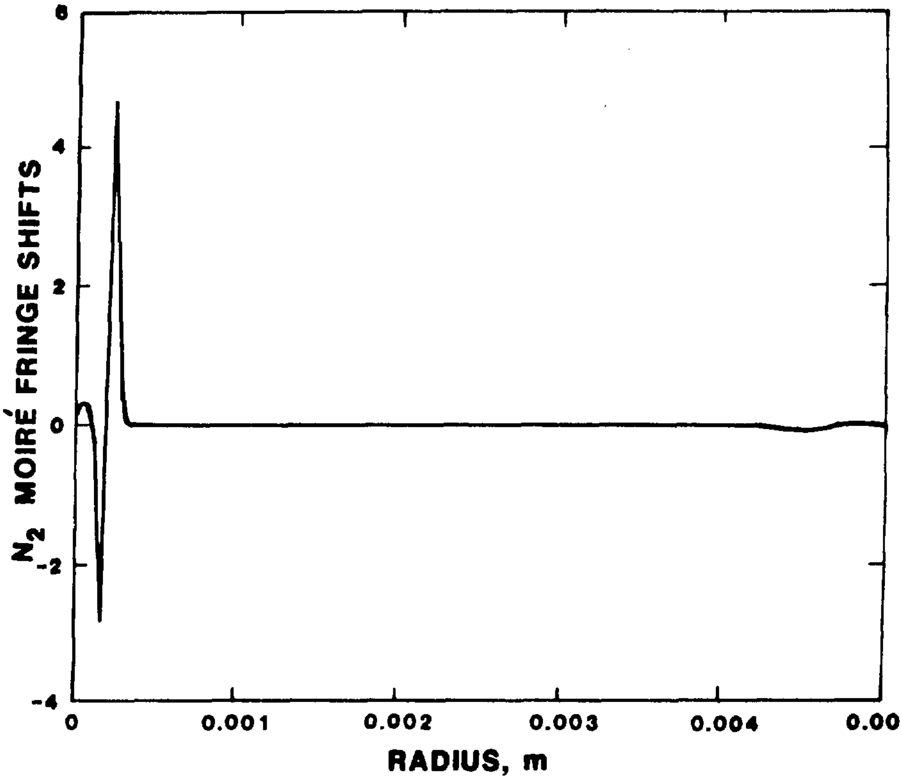

Fig. 4.39 Computed Moiré fringe profile for MANIAC results

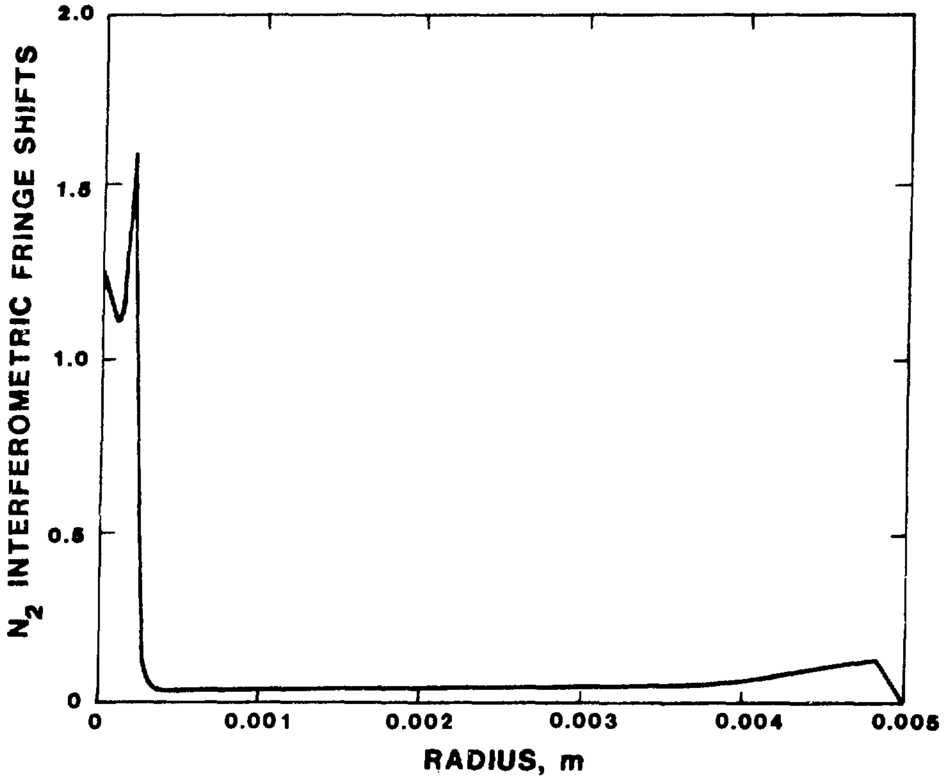

Fig. 4.40 Computed interferometric fringe profile for MANIAC results

References for Chapter 4

1. J. B. Taylor, Phys. Rev. Lett. 33, 1139 (1974).

2. D. H. McDaniel, Sandia National Laboratory, personal communication, 1979.

3. J. E. Hammel, Los Alamos Scientific Laboratory report LA-6203-MS, (1976).

4. I. R. Lindemuth, Los Alamos National Laboratory, personal communication, 1980.

5. I. Lindemuth, J. Brownell, T. Oliphant, and D. Weiss, Los Alamos Scientific Laboratory report LA-UR-81-346, (1981); see also E. Yablonovitch, Appl. Phys. Lett. 23, 121 (1973).

6. Atomic Data for Controlled Fusion Research, Oak Ridge National Laboratory report ORNL-5207, edited by C. F. Barnett et al., Vol. II, pp. E.1.8-E.1.9 (1977).

7. Barnett et al., Ibid., pp. E.1.6-E.1.7.

8. I. R. Lindemuth, Los Alamos National Laboratory, personal communication, 1981.

Chapter 5. Conclusion

In the preceding chapter, we examined evidence which supports the hypothesis that current flow outside a laser-initiated channel is an important process in HDZP experiments at fill pressures less than one atmosphere. We now briefly discuss alternative explanations for the discrepancy between x-ray detector data and Bennett temperature predictions and present suggestions for future diagnostic work which can investigate this problem in depth.

5.1 Verification of Non-localized Current Model

Estimates of the photomultiplier anode signal currents, for plasma conditions inferred from Moiré-Schlieren and interferometric results, require knowledge of the scintillator response, photocathode sensitivity, and tube gain. The values for these quantities gleaned from device specification data are possibly in error and can lead to a false interpretation of small or sub-threshold detector signals. We have therefore recently performed a system calibration using the HSXR-2 soft x-ray "Henke" tube source at Los Alamos.[1] These tests were conducted with a detector configuration employing four 1/8" diameter, 20′ long optical fibers (Nanofast OC-50) transporting the scintillator output to an RCA-8575 photomultiplier tube. The 2" diameter, 1/2" thick Pilot B scintillator is located directly behind a 1.0 mil Al foil, which in turn is supported by an aluminum rib structure. Using an aluminum anode in the "Henke" tube, and operating at 2.6 kV, radiation slightly below the Al-K line at 1.49 keV was produced. A 3.9 mg/cm^2 Al foil acted as an output filter for the source to enhance the spectral purity of the x-rays. Based on a previous measurement for these conditions,[2] 96% of the photons are expected to lie in the K-edge peak with a FWHM of 160 eV. Because of the high input impedance of the Keithly 610 electrometer used to record the dc detector current, the photomultiplier anode was coupled directly to the electrometer without the usual 50 Ω grounding resistor. The source fluence, determined by HSXR-2 personnel using an ionization chamber, is

$$F = 8.6\times10^{11}\ \frac{\text{x-rays}}{\text{sr-s}}\ , \tag{5.1}$$

and our detector subtends a solid angle of

$$S = 1.4\times10^{-2} \text{ sr} . \qquad (5.2)$$

With the photomultiplier operating at -2000 V, the output signal for a "Henke" tube emission current of 350 mA was

$$I_{SIG}^{Observed} = (5 \pm 1)\times10^{-7} \text{ A} . \qquad (5.3)$$

We compare this with our prediction of signal amplitude using estimates of the system sensitivity. The 1.0 mil Al vacuum seal foil is computed to have a transmission coefficient of

$$T = 0.067 . \qquad (5.4)$$

We estimate the scintillator-photocathode response to be

$$SC = 3\times10^{-4} \text{ C/J} \qquad (5.5)$$

for 1.5 keV x-rays, while the tube gain, at -2000 V, is given by

$$G \simeq 1.4\times10^{7} . \qquad (5.6)$$

All of the x-rays are presumed to be fully absorbed by the thick scintillator. The fiber optic cable assembly transmission efficiency, determined under test conditions at 6943 Å using a ruby laser pulse, is

$$E_f = 4.7\times10^{-3} . \qquad (5.7)$$

We therefore predict a signal current of

$$I_{SIG}^{Predict} = F\times S\times(1.5\times10^3)\times(1.6\times10^{-19})\times T\times SC\times G\times E_f \qquad (5.8)$$

or

$$I_{SIG}^{Predict} = 3.8\times10^{-6}\ A \simeq 8\times I_{SIG}^{Observed} . \qquad (5.9)$$

In general, however, we have used conservative tube gain estimates of

$$G = 10^6 \qquad (5.10)$$

to illustrate the inconsistency between Moiré/interferometric predictions and photomultiplier-scintillator observations. We thus conclude that this inconsistency is not the result of an over-estimate of the x-ray diagnostic sensitivity.

The Bennett temperature calculations in Chapter 4 begin with the assumption that the magnetic field pressure from a self-generated B_θ is balanced entirely by internal plasma pressure. A helical current configuration, however, can produce an axial magnetic field which will contribute to the internal pressure and lower the effective Bennett temperature, and the resultant bremsstrahlung output may be below the x-ray diagnostic detection threshold. Data obtained in an axial magnetic field diagnostic, described in Chapter 4, were inconclusive and do not preclude the existence of B_z pressure. The line density data which were used to demonstrate the apparent diagnostic discrepancies, however, were restricted to early times during the discharge for which the N_2 laser-produced photographs indicate a reasonably one-dimensional axisymmetric channel. We find it unlikely that large solenoidal fields are generated before the appearance of the three-dimensional structure and do not presently consider internal axial field pressure to be a significant factor in the momentum equation for the plasma regime of interest.

While the hypothesis of current flowing outside the central column is plausible, more direct measurements of the radial current profile are needed to substantiate this view. We have considered two specific nonperturbing diagnostic schemes sensitive to B_θ, namely, Faraday rotation and Zeeman splitting.

The polarization of an electromagnetic wave propagating a distance ℓ along a magnetic field B is rotated by an angle

$$\theta = 2.63\times10^{-13}\ \lambda_L^2\ n_e\ B\ \ell \tag{5.11}$$

with all quantities in MKS units.[3] If we consider a He:Ne laser beam transverse to a current carrying column with average field

$$B_\theta^{ave} \approx \frac{1}{2}\,\frac{\mu_o I}{2\pi r_p}\ , \tag{5.12}$$

then for $I = 10^5$ A, $r_p = 10^{-4}$ m, $\lambda_L = 6.3\times10^{-7}$ m, $n_e = 3\times10^{25}$ m^{-3}, and $\ell = 2\times10^{-4}$ m, we find

$$\theta \approx 6.3\times10^{-2} \text{ radians} = 3.6^o, \tag{5.13}$$

a rotation which can be detected with cross polarizers.

Experimental results obtained on a plasma focus device[4] indicate the feasibility of a Zeeman splitting measurement to determine the peak magnetic field under high density ($n_e \sim 10^{25}$ m^{-3}), high β ($\sim$ 1) conditions. Detection of the CV (2s - 2p) multiplet by Norton and Peacock was enhanced by the addition of 2.5% ethylene by volume to the deuterium fill, and the emission was analyzed with a photomultiplier and normal-incidence monochromator arrangement. With proper consideration given to thermal-Stark effect broadening and mass motion splitting, the observed 6 Å shift of the σ-radiation indicated a magnetic field in the range

$$80 < B_\theta < 200 \text{ T} . \tag{5.14}$$

The data were recorded on a shot-to-shot basis with a time resolution of 8 ns. The conditions of n_e and B_θ for the plasma focus are sufficiently similar to those of the HDZP to warrant more detailed study of this technique as a relatively direct means of determining the current profile.

5.2 Summary

In this thesis we have investigated an unusual plasma parameter regime characterized by densities approaching 10^{26} m^{-3}, sub-microsecond time scales, 100 μ radial dimensions, and rapid rising currents ($\dot{I} > 10^{12}$ As^{-1}). One motivation for examining narrow, gas embedded channels is the recognition of the virtues of a dense, ohmically heated column as a fusion reactor plasma, namely, relatively low cost, size, and energy input compared to conventional magnetic confinement configurations. The HDZP concept must overcome several obstacles including possible MHD instabilities and anomalous thermal loss mechanisms to become a useful fusion approach; nevertheless, simple scaling arguments suggest it is an option which must be explored.

This work has extended simple analytical plasma models by including realistic dynamic processes, allowing us to predict the column behavior in existing and future experiments, with the assumption of a constant number of plasma particles (constant line density). Measurements have been made on a 6 kJ device (prototype HDZP) which employs a laser to initiate a narrow channel in the discharge chamber. A parametric study involving the initiating laser identified the channel formation phase as an area for further experiments. Modification of a simple Schlieren optical technique using coarse gratings (Moiré-Schlieren) resulted in a unique and valuable quantitative density diagnostic, and the data indicate a monotonic increase in plasma line density, clearly undesirable from an energy inventory viewpoint. While the mechanism driving this accretion process is not understood, the increase in line density has been shown to dominate the dynamic behavior of the column and must be incorporated into computational and analytical models of HDZP plasma systems. The data from an x-ray diagnostic reveal an important discrepancy between Bennett temperature predictions and temperature estimates based on bremsstrahlung emission, suggesting that a significant fraction of the load current may be flowing outside the visible, laser-initiated channel for chamber fill pressures below one atmosphere. This hypothesis has been indirectly supported by simple calculations, experimental tests, and 2-D MHD computations.

Additional work in the Los Alamos HDZP experimental program will concentrate on increased densities (1-5×10^{26} m^{-3}) and longer initiation laser wavelengths (e.g., Nd-glass at 1.06 μ) in an effort to insure current flow in a small central channel. A new, higher current device (4-10×10^{5} A) will allow investigation of potentially high temperature plasmas under HDZP reactor-type conditions. We are optimistic that the problems observed to date and described in this thesis can be solved and are excited at the prospect of continued research on this novel fusion approach.

References for Chapter 5

1. We are indebted to the P-14 group at Los Alamos National Laboratory, in particular R. H. Day, W. C. Priedhorsky, and P. J. Walsh, for their assistance in this calibration.

2. R. H. Day, Los Alamos National Laboratory, personal communication, 1981.

3. F. C. Jahoda and G. A. Sawyer in Methods of Experimental Physics, edited by H. R. Griem and R. H. Lovberg (Academic Press, New York, 1970), Vol. 9, Part B, Chapter 11.

4. B. A. Norton and N. J. Peacock, Culham Laboratory Report CLM-P 363 (1973).

ACKNOWLEDGMENTS

The experiments reported in this thesis were conducted in the CTR-Division of Los Alamos National Laboratory as part of the Institutional Supporting Research Program. This work could not have been completed without the assistance of several friends and associates. I am particularly grateful to Professor Ralph Lovberg for his guidance and encouragement throughout my graduate years. The supervision of Jay Hammel, who conceived and designed the prototype HDZP experiment is also acknowledged. Discussions with numerous members of CTR-Division have been of great value, with a special thanks to Dave Scudder. The numerical modeling was a result of fruitful conversations with Tom Oliphant and Irv Lindemuth, who have been most generous with their time. The development of the optical diagnostics depended in large measure on the efforts of Dave Platts, Franz Jahoda, and Pete Forman; Carl Ekdahl's contributions to the probe and x-ray diagnostics were also valuable. The fabrication of several essential components of the experiment was completed by Bob Barnes and his able crew. Dalio Rodriguez provided an outstanding service as machinist during the past few years.

The preparation of this manuscript was accomplished with the aid of Yvonne Johnson, who patiently typed the hand-written text into the computer. Additional thanks go to the illustrators, Barbara Edwards, Arlene Branson, and Ed Vigil, for their fine work, and to Sharon Crane, whose efforts resulted in the final figures.

☆U.S. GOVERNMENT PRINTING OFFICE: 1982-0-576-020/97